UNIVERSITÀ DEGLI STUDI DI PADOVA

DIPARTIMENTO DI INGEGNERIA DELL'INFORMAZIONE

DIPARTIMENTO DI INGEGNERIA DELL'INFORMAZIONE

CORSO DI LAUREA IN BIOINGEGNERIA

A comparison of transverse relaxation time estimation models for cardiac magnetic resonance imaging in assessing left ventricular iron overload

Relatore

Dott. Ing. Castellaro Marco

Laureando

Checchetto Ambra

Correlatori

Prof.ssa Pepe Alessia

Dott.ssa Lupi Amalia

ANNO ACCADEMICO 2023-2024

Data di Laurea 12/12/2024

INDEX

ABSTRACT

Cardiac magnetic resonance imaging is one of the most advanced tools used in clinical routine to assess the physiology, anatomy or function of the heart. Its versatility and non-invasiveness have made it an important method of diagnosis. This technique can also be exploited to measure myocardial iron overload, since iron is a paramagnetic substance. Iron accumulation leads to a decrease in T2* relaxation time, which can be used as a marker to detect important diseases such as Haemochromatosis and Thalassaemia. A significant reduction in T2* means that there is a substantial accumulation of iron, resulting in myocardial dysfunction. To assess left ventricular iron overload, four T2* estimation models were implemented: three non-linear models and one linear model, comparing pixel-wise approach and ROI-based approach. Since the dependence of the MR signal on echo times can be described by an exponential decay, the implemented non-linear models are distinguished between a single-exponential model, a biexponential model and an offset model. The fourth model was obtained by linearising the exponential model. From each model, it is thus possible to obtain T2* maps of the ventricular myocardium, which is divided into three parts: basal, medial and apical region, for a total of sixteen segments. All these models were compared using different evaluation metrics, and mono-exponential model proved to be the most suitable for T2* estimation. Besides, all models were applied to healthy subjects and patients with Haemochromatosis, to evaluate T2* trend in all segments. Using T2* estimates obtained in healthy subjects, a map of correction factors was also created to correct for the presence of artifacts such as the heart-lung interface and blood vessel pulsation that corrupt the image signal. Even if the calculation of the correction factors is based on manual segmentations, thus involving a selection of the mid-ventricular septum by the radiologist, the map obtained turns out to be robust also to simulated error of the individuation of the septum. In addition, a second correction map was implemented based on more precise segmentations, which do not divide the myocardium into equidistant segments, but adjust the segment lengths based on the inter-ventricular septum. In conclusion, T2* parametric mapping proves to be a good assessment method to reveal the presence of myocardial iron overload, allowing accurate diagnoses.

INTRODUCTION

1.1 Cardiac magnetic resonance imaging

Magnetic resonance imaging is one of the most advanced imaging techniques in the study of human physiology and internal anatomy. It is exploited in many different applications because of its versatility and non-invasiveness, and it is widely used in clinical routine. For these reasons, MRI has also become an effective diagnostic examination modality in the cardiac field. Its introduction into clinical practice in the 1980s sparked significant advancements in research, enabling the derivation of key medical parameters with greater flexibility and high accuracy. Cardiac magnetic resonance imaging can be used to assess both the function and structure of the heart: the main accessible features are the anatomy of the atria and ventricles under resting and/or stress conditions, the tissue composition of the myocardium, the biochemical environment, the deposition of substances such as iron or pericardial fat, the pattern of blood flow within the vessels and chambers, cardiac metabolism, possible presence of oedema or fibrosis, perfusion and diffusion (summarized in Figure 1.1) [1]. The significant growth in the use of cardiac MRI, particularly in Europe over the last decade, has turned it into an important diagnostic tool. Advances in cardiac MRI techniques, such as faster image acquisition, quantitative characterization of myocardial tissue, and image analysis, have been essential in its development. Moreover, considering that cardiovascular diseases are the leading cause of death in the world and have an important impact in the health economy, the presence of an effective and accurate imaging modality can contribute greatly to detecting these diseases early, making more precise diagnoses, and personalizing treatments. In addition to the advantages related to the wealth of physiological information that MRI provides access to, a further positive aspect remains the simple way an MRI examination is performed, which requires only that the subject is motionless during the scan and executes cycles of inhalation and exhalation, depending on the instructions given by the operator who is performing the scan. However, to improve or make the images more informative, in some specific cases it is preferable to coordinate the triggering of image acquisition with the signal obtained from the electrocardiogram, to identify the specific waves that characterize the tracing and derive more precise information about the patient's cardiac cycle. For example, it is possible to recognize the QRS complex, which makes it possible to identify when depolarization of the ventricles is occurring [2].

Another tool that is exploited to enhance image visualization and enhances details is the injection of contrast agents. Gadolinium is the tracer that is most widely used for magnetic

resonance imaging examinations. Gadolinium-based contrast agents involve the formation of complex molecules given by the chemical bonds formed between the gadolinium ion and substances that act as chelating agents. Such agents can prevent the potential toxicity of gadolinium while maintaining the contrast properties. Gadolinium is injected intravenously over a period of 10 to 30 seconds and then eliminated from the body by the kidneys. This type of contrast agent especially enhances visualization of inflammation, tumours, blood vessels, and, for some organs, blood flow [3] . In some cases, contrast medium can cause allergic reactions or, in more serious situations, nephropathy. However, these are the only risks encountered during an MRI examination, as MRI has been widely demonstrated to be a safe imaging modality free of adverse effects, including long-term ones. In fact, the magnetic field and radiofrequency waves used to generate images work outside the range of ionizing radiation, so there is minimum biological hazard to present complications [4] . Claustrophobia is the most common adverse reaction to the MRI examination and can occur in 1% to 2% of the population, but generally can be managed with nonpharmacological strategies [5] Although the advantages associated with the use of MRI are several, there remain some limitations such as the cost of scanners, moderate availability of the devices due to the complexity of the equipment, and the need to introduce experienced and well-qualified personnel [1]. The role of MRI as an emerging method for determining iron accumulation at the ventricular level, a pathological condition that leads to major cardiac dysfunctionality, will be explored in the current thesis.

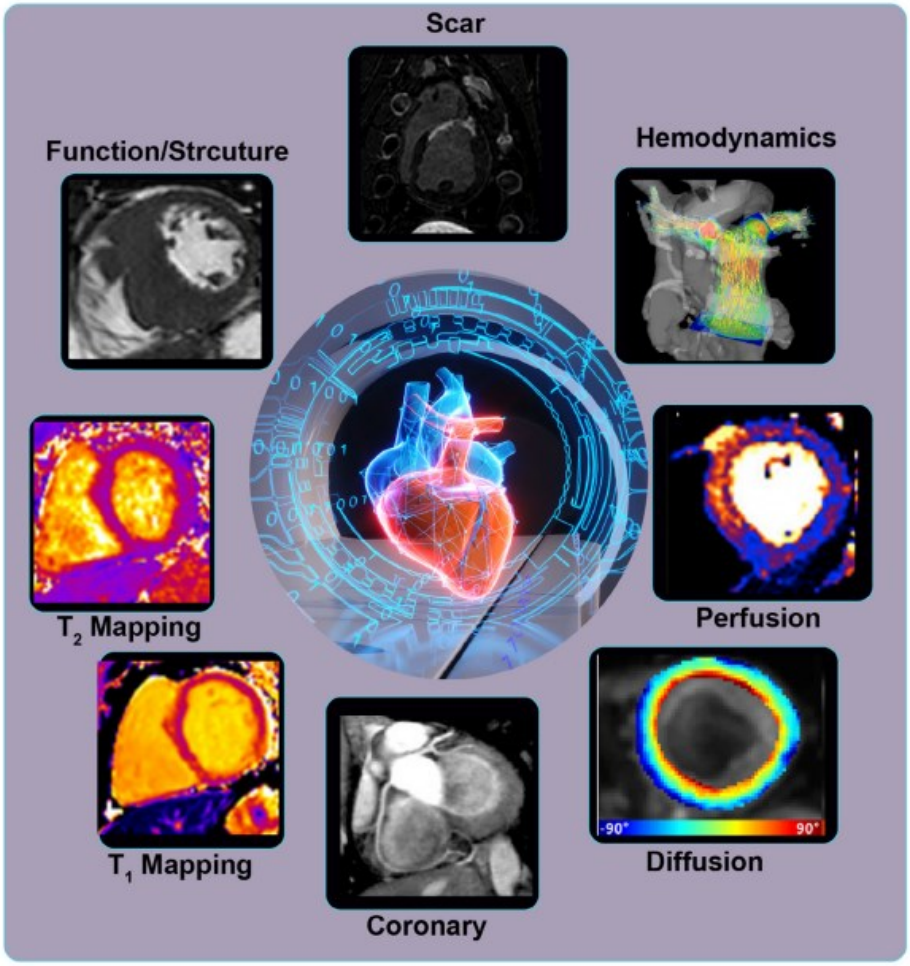

Figure 1.1. Summary of the functions of CMR: Cardiac MR imaging provides a comprehensive assessment of the structure, function, perfusion, viability, hemodynamic, microstructure, and myocardial mapping via T1, T2, and T2* [6]

1.2 Heart anatomy

The heart is a muscular organ that, along with blood vessels and blood, forms the cardiovascular system. The role of the heart is to push blood to all organs and tissues of the body, ensuring efficient distribution of gases, nutrients, signal molecules and metabolic waste substances. It occupies the central part of the mediastinum, and is therefore located within the thoracic cavity, particularly on the ventral side, enveloped by a protective sac called pericardium. It has a conical shape where the apical part faces downward with a left orientation and makes contact with the diaphragm, while the base is located behind the sternum. Thus, the major axis of the heart is located at an oblique angle to the long axis of the human body [7].

It weighs 250-300 *g*, and it is about 12-13 *cm* long and 8-9 *cm* wide. It is divided into four cavities: two atria (upper cavities) and two ventricles (lower cavities). The right side is divided from the left side by a septum, which is called the interatrial septum in the upper area and the interventricular septum in the lower area. This structure has a specific meaning: preventing the blood on the right side from mixing with the left side, keeping the flow of oxygenated blood and the flow of deoxygenated blood constantly separated. Despite this division, myocardial contraction occurs in a coordinated manner: the two atria contract simultaneously, followed then by the ventricles. Blood flows in only one direction, from the atrium to the ventricle, and unidirectionality is ensured by the presence of the heart valves, which open and close in response to pressure differences during the cardiac cycle. This one is organized as follows: blood enters the right atrium through the superior vena cava and inferior vena cava, via the tricuspid valve it enters the right ventricle from which the pulmonary artery departs, allowing the blood to reach the lungs, where it will be oxygenated. From the lungs, blood returns to the heart, specifically to the left atrium, via the pulmonary veins. Like the right side, blood passes through the mitral valve and enters the left ventricle. The left ventricle is the main pump of the systemic circulation, as it is responsible for pushing oxygenated blood to all tissues in the body. The blood enters the aorta, the main artery in the body, through the aortic valve, and from there it is distributed in an extensive network of arteries and capillaries until it reaches all biological districts. Because the left ventricle must cope with the high resistance of the arterial system, its walls are thicker in size than those of the other cavities [8] . The structure of the heart is shown in Figure 1.2.

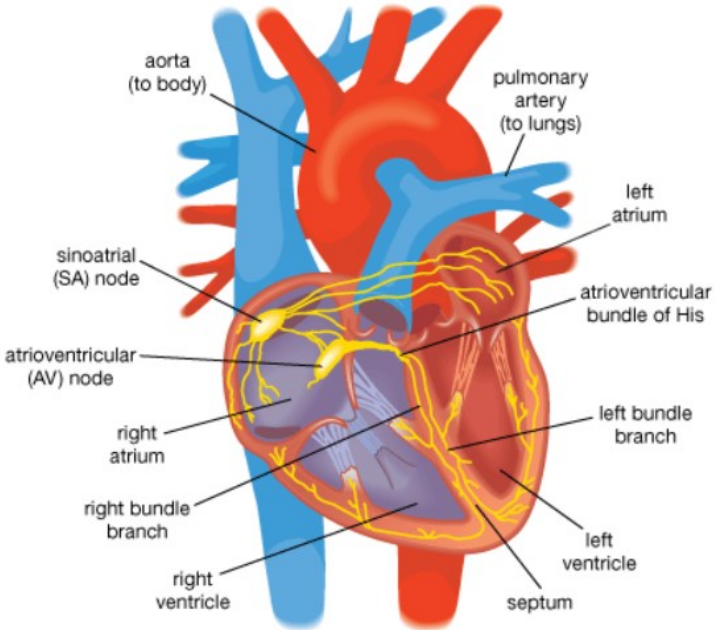

Figure 1.2. Heart Anatomy [9]

The heart wall (Figure 1.3) consists of a structure organized in layers, in which it is possible to identify:

- The endocardium: innermost layer bounding the lumen of the heart; being a continuation of the tunica intima of the blood vessels, it is composed of a simple squamous epithelium overlying a fibroelastic connective tissue. A deeper layer of dense connective tissue is richly supplied with elastic fibers and interspersed with smooth muscle cells. The deeper, sub-endocardial layer, which separates the endocardium from the myocardium, is composed of loose connective tissue with blood vessels, nerve fibers, and Purkinje fibers [10] .
- The myocardium: is the middle and most robust layer of the cardiac wall; it is composed of cardiac muscle cells. These can be contractile or autorhythmic (1% of cardiac cells). These ones regulate the contraction of the heart autonomously, generating action potentials without the need to receive signals from the nervous system. While contractile cells have fibers organized into sarcomeres, autorhythmic cells (or pacemaker cells) are smaller in size and therefore have fewer contractile fibers [8].
- The epicardium: outermost layer of the heart; it can be seen the visceral pericardium (serous membrane with protective and lubricating function) and the parietal pericardium (composed of an inner serous layer and an outer fibrous layer). The pericardial cavity located between the visceral and parietal pericardium contains serous fluid to reduce friction between the two surfaces of the pericardium during movement of the heart [10].

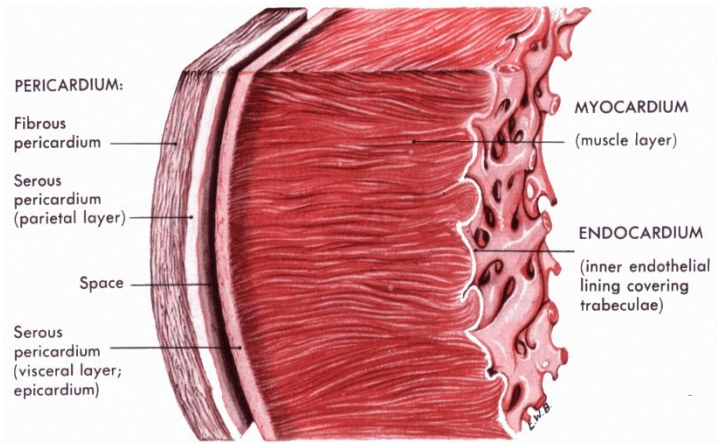

Figure 1.3. Layers of heart wall [11]

1.3 Basics of Magnetic Resonance

1.3.1 Physical Principles

Magnetic resonance imaging takes this name because it is based on a physical phenomenon known as 'nuclear magnetic resonance,' according to which atomic nuclei exposed to a strong magnetic field absorb and re-emit electromagnetic waves at a characteristic (or 'resonant') frequency, which falls in the radio frequency (RF) range. Specifically, reference is made to the nuclei of hydrogen atoms, a chemical element abundant in biological tissues since there is a high amount of water and fat. The nuclei of hydrogen atoms exhibit magnetic moments that undergo a rotational motion, known as precession, in the presence of a permanent magnetic field (denoted by the notation 'B0'). The concept of magnetic moment is associated with that of spin, which allows interactions with the magnetic field to be given. In the absence of a static magnetic field, magnetic moments orient themselves randomly, as a result the macroscopic magnetization (Mo), that is the vector sum of all moments, is equal to zero due to the mutual cancellation of vectors having opposite directions. In the presence of a magnetic field, the magnetic moments tend to align with the direction of B0 and this leads to a macroscopic magnetization that is non-zero (Figure 1.4). Considering the conventionally assumed three-dimensional reference system, in which the magnetic field B0 is arranged along the z-axis, it can be seen that the magnetization vector will then be decomposable into a transverse component (Mxy) and a longitudinal component (Mz). In an equilibrium condition, Mz will be coincident with Mo, while Mxy will be zero. Specifically, there are two different configurations (Figure 1.5): the low-energy (or 'spin-up') one in which the orientation of the dipoles exhibits the same direction as B0 (parallel direction), and the high-energy (or 'spin-down') one in which the dipoles oscillate by orienting in the opposite direction as B0 (antiparallel direction). The preferred configuration is the lower-energy one [12].

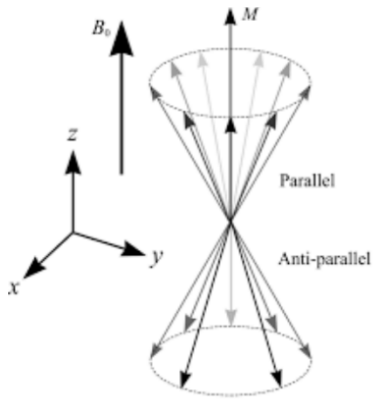

Figure 1.4. Magnetization result

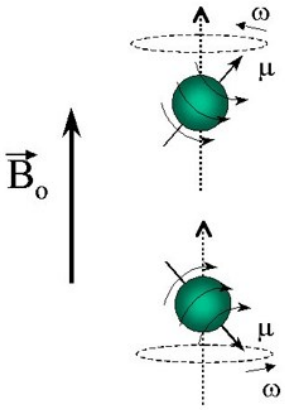

Figure 1.5. Spin-up configuration (upper side) and spin-down configuration (lower side)

Considering that the magnetic moment of the nucleus (μ) has the same direction as its spin (I), we have the following relationship:

$$\mu = \gamma I$$

Where γ indicates the gyromagnetic ratio, an intrinsic characteristic of the nucleus that varies from isotope to isotope. The frequency that characterizes precession motion (Figure 1.6) is called the Larmor Frequency (w_L), and is expressed through Larmor's law, according to which the Larmor frequency is proportional to the gyromagnetic ratio and the magnetic field B0:

$$w_L = \gamma B_0$$

It follows that B0 imposes a momentum that goes to influence the magnetic moment itself. Gyromagnetic ratio values for the cores of interest are in the range of megahertz (MHz) per Tesla (T), where Tesla is the unit measurement of magnetic field strength. Since the field strengths typically used in MR scanners are on the order of a few Teslas, Larmor frequencies fall in the megahertz range [12] .

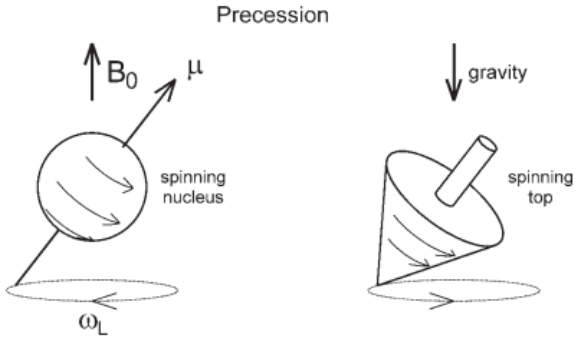

Figure 1.6. Spin Precession

1.3.2 Relaxation times

The condition described in the previous section (where in the presence of a static magnetic field B0, the magnetization vector M0 is perfectly aligned with the z-axis) can be modified by introducing a stimulation magnetic field, called B1. It is possible to obtain a magnetization component in the transverse plane (*xy* plane) if the magnetic field is applied with a rotational frequency equal to the Larmor frequency (which can be mathematically derived from Larmor's law), so that the so-called resonance phenomenon is obtained. Some nuclei that were previously in a spin-up configuration switch to a spin-down configuration, and thus the longitudinal magnetization component is reduced. At the same time, a transverse component will appear due to the synchronization of the precession motions, which are brought 'in phase'. As long as B1 transfers energy to the cores, the magnitude of the Mxy component will continue to increase. However, when B1 stimulation is removed, the system restores the original condition: the Mz component is recovered and the Mxy component tends to disappear. This phenomenon is called relaxation and is distinguished into longitudinal relaxation and transverse relaxation, respectively. Longitudinal relaxation is also known as spin-lattice relaxation because the energy that has been absorbed by the protons is given up to the surroundings. The time constant that describes the restoration of the longitudinal component is usually denoted as T1. The mathematical function describing this phenomenon in dependence on time '*t*' (from when the B1 magnetic field is removed) is the following:

$$M_z = M_0\left(1 - e^{-\frac{t}{T_1}}\right)$$

More precisely, the constant T1 represents the time to reach 63% of the magnitude of the original Mz component. The graphical curve represented in figure 1.7 shows the trend of Mz component.

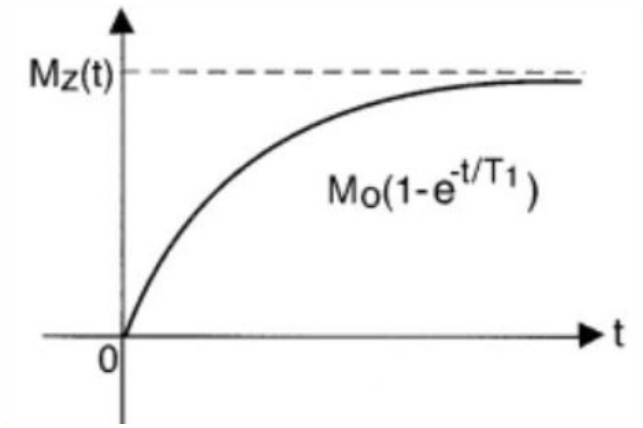

Figure 1.7. Longitudinal relaxation: trend of magnetization along the z axis over time [13]

The other phenomenon is the transverse relaxation. In this case, the Mxy component reduces, and this occurs faster than longitudinal relaxation because of mechanisms related to spin phase loss. The time at which there is a return of equilibrium of the Mxy component is described by the time constant T2 (spin-spin relaxation time). As before, the phenomenon can be mathematically described through the equation:

$$M_{xy} = M_0 \, e^{-\frac{t}{T_2}}$$

More precisely, T2 indicates the time by which the cross component decreases by 37% of the original value. The graphical representation is reported in figure 1.8. In addition, the constant T2 is always smaller than the constant T1[12] .

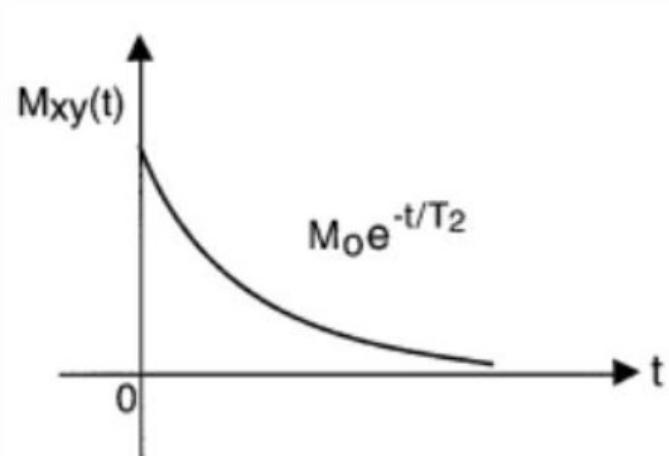

Figure 1.8. Transverse relaxation: trend of the magnetization component along the *xy* plane over time [13]

However, the presence of inhomogeneities (ΔB_i) in the magnetic field, to which the protons are subjected, introduces an additional relaxation constant, known as T2* ('*T2 star*'), indicating a greater loss of magnetization along the transverse plane. This time constant has a smaller value

than the T2 time constant because the dephasing of the magnetization is faster than pure T2 relaxation. The mathematical equation describing their relationship can be expressed as:

$$\frac{1}{T2*} = \frac{1}{T2} + \gamma \Delta B_i$$

[14]

As introduced in the first section (1.1), in the current thesis, T2* relaxation time will be used as the main marker for assessing the health of the heart in relation to the amount of iron in the left ventricle [12] .

1.3.3 General Acquisition Sequences

The detection of the nuclear magnetic resonance signal is performed by means of a special radio frequency coil that is placed along the transverse plane (XY plane). During the relaxation process, signals emitted by protons are picked up by such a receiving coil, and it is from this information that the image will be created. Specifically, the recorded signal is a sine wave since its amplitude decreases over time due to the loss of phase coherence between the protons. This signal is called Free Induction Decay (FID). MRI sequences are a specific succession of radio-frequency pulses, which are emitted in a precise order according to the tissues or properties to be highlighted. The parameters that allow different types of sequences to be defined are:

- Repetition time (TR): time interval between two consecutive RF pulses
- Echo time (TE): time interval between the RF pulse and the maximum echo amplitude
- Flip-angle (FA): amplitude of the tilt angle that is determined between the magnetization vector (as a result of the RF pulse) and the main magnetic field (B0).

The main acquisition sequences are distinguished into Gradient-Echo (GE), Spin-Echo (SE), which can be exploited within more complex sequences [12] .

1.3.3.1 Gradient-Echo Sequences

To obtain FID with a Gradient-Echo sequence, a single RF pulse is applied during each TR period at an angle that is less than 90°. It is characterized by very short repetition times (on the order of milliseconds) and therefore exploited when fast acquisitions are desired. A slice-selection gradient is applied during the RF pulse, which allows a single slice of the volume

under examination to be excited. Then, gradients of opposite sign are applied, inducing a spin phase shift and subsequent recovery of phase coherence to regenerate the signal. This sequence is unable to correct for phase shifts due to magnetic field inhomogeneities. Therefore, the signal decays faster, and a short TE value must be used to record a signal with sufficient intensity. A time diagram summarizing the application of the different gradients that characterize this sequence can be seen in Figure 1.9. An analog-to-digital converter, accessed during the signal acquisition phase, is also used [12] .

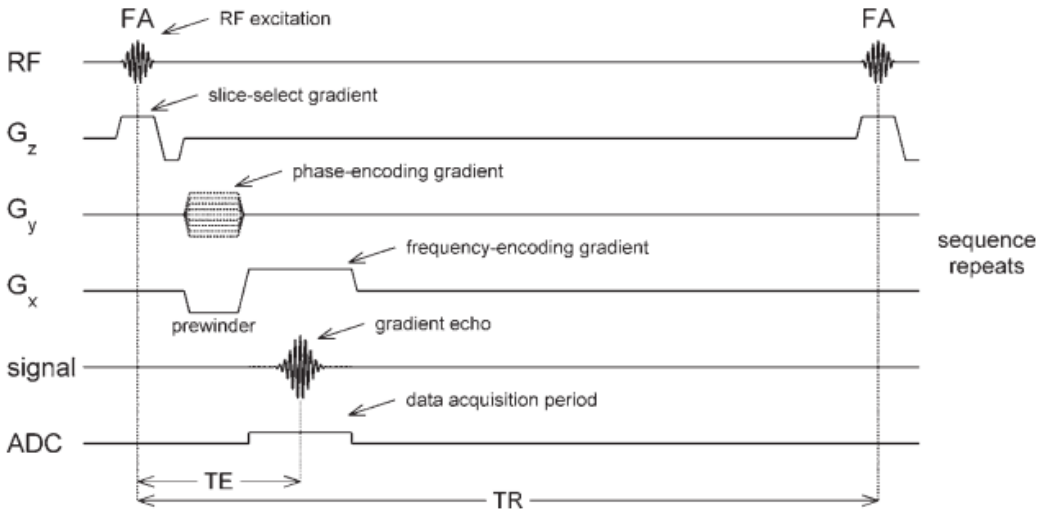

Figure 1.9. Time diagram of a GE sequence. Gz=slice coding gradient, Gy=phase coding gradient, Gx=frequency coding gradient, ADC=analog-to-digital converter [12]

1.3.3.2 Spin-Echo Sequences

The spin-echo sequence presents a succession of pulses similar to the gradient-echo sequence but uses two RF pulses in each TR repetition time. The first pulse that is launched presents a 90° flip-angle, while the second pulse presents a 180° flip angle. Thus, the first pulse induces a flip of the magnetization vector toward the transverse plane, while the second pulse results in a 180° rotation of the magnetization vector resulting in spin realignment and echo generation. Specifically, the 180° pulse is applied after a time equal to half echo time. The phase-encoding gradient is applied between the 90° pulse and the 180° pulse, while the frequency-encoding gradient is applied after the 180° pulse (thus during echo detection). In Figure 1.10, the summary temporal pattern can be observed. One of the limitations of this type of sequence is the high duration that it can present in cases where T1 is particularly long. This happens because it is necessary to wait for the magnetization vector to fully restore the equilibrium position along

the z-axis before proceeding with the next pulse. Thus, the main differences between the spin-echo sequence and the gradient-echo sequence concern the overall duration and the technique exploited to achieve the spin return to phase, which in the former case occurs through the 180° pulse while in the latter case it exploits a magnetic field gradient [12].

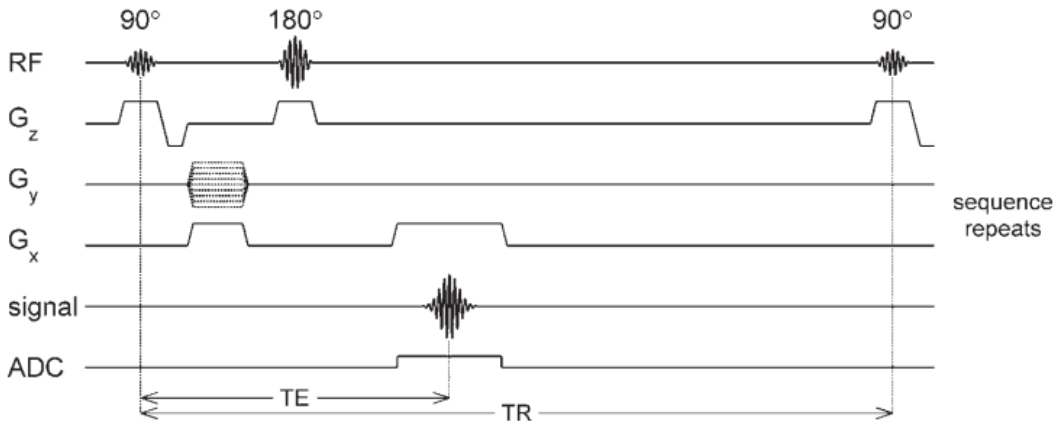

Figure 1.10. Time diagram of an SE sequence. Gz=slice coding gradient, Gy=phase coding gradient, Gx=frequency coding gradient, ADC=analog-to-digital converter [12]

Considering that the duration of the TR and TE times can be controlled by the operator during acquisition, it is possible to combine these values to obtain a specific stimulation leading to the desired result. Specifically, a high TR decreases the effect induced by time T1, while a high TE increases the effect induced by time T2. Consequently, a short TR accentuates the effect induced by time T1, and a short TE decreases the effect induced by time T2. Therefore, it is inferred that setting short values of TR and TE will result in T1-weighted images, and with longer values of TR and TE will result in T2-weighted images instead.

1.3.4 Cardiac Gating

1.3.4.1 Free Breathing

The requirement for a patient breath-hold in studies of cardiac function is a current limitation of cardiovascular MRI. Standard cine exams are segmented over several heartbeats, so a breath-hold is required to minimize breathing motion artifacts. The breath-hold constraint reduces patient comfort and can yield poor image quality due to inconsistent breath-holding. Since this technique shows several limitations, free breathing cardiac MRI could be a valid solution. Free breathing in cardiac MRI needs motion correction because respiratory motion introduces

artifacts that degrade image quality. During free breathing, the chest wall, diaphragm, and internal organs move continuously, causing changes in the spatial relationship between the MRI signal acquisition and the anatomy being imaged. These movements can blur images, create artifacts, and compromise the accuracy of diagnostic measurements. By implementing motion correction strategies, free-breathing imaging achieves high-quality results comparable to breath-holding approaches, making it especially valuable for patients unable to hold their breath, like pediatric or elderly patients [15] . These motion techniques are distinguished into Navigator echoes and advanced motion correction algorithms.

1.3.4.2 Prospective VS Retrospective Gating

Cardiac gating techniques in cardiac MRI minimise motion artefacts by synchronising image acquisition with physiological markers such as ECG R-wave or diaphragm position. These techniques can be divided into prospective gating, which acquires data at predefined cardiac phases, and retrospective gating, which acquires data throughout the cardiac cycle for later sorting. While ECG gating is more accurate than alternatives such as pulse oximeters, cardiac motion is inherently complex due to longitudinal, radial and rotational components, compounded by R-R interval variability due to normal beat-to-beat changes, premature contractions and respiratory effects. Patient-specific cardiac tracings are analysed prior to scanning to optimise data acquisition and address these challenges, ensuring higher image quality despite variability. Prospective gating (Figure 1.11) in cardiac MRI uses R-wave detection to trigger k-space filling for a set percentage (typically 80-90%) of the R-R interval, leaving the last 10-20% as an arrhythmia rejection window to minimise motion artefacts. This ensures a constant number of filled k-space lines per interval and can include broader arrhythmia rejection to handle premature contractions. It is commonly used in static and cine imaging. In contrast, retrospective gating (Figure 1.12) fills k-space continuously throughout the cardiac cycle, oversampling the R-R interval (up to 125%) and retrospectively assigning data to specific cardiac phases based on R-wave detection. This method handles beat-to-beat variability and premature contractions by interpolating data and is widely used in cine sequences such as GRE (gradient-recalled echo), True FISP, FIESTA and phase contrast imaging. The arrhythmia reject window can be applied in both prospective and retrospective gating to exclude k-space data from R waves that deviate significantly from expected parameters in patients with highly variable R-R intervals. This window can be symmetric or asymmetric around the expected R wave to enhance data accuracy [16].

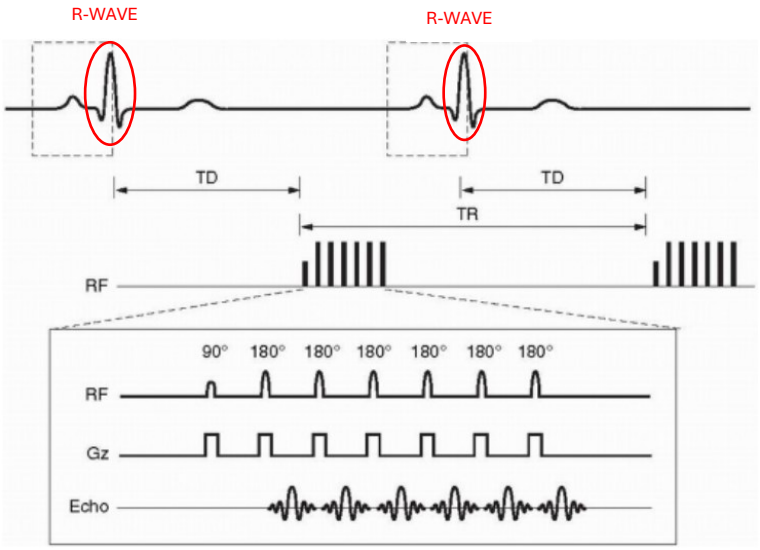

Figure 1.11. Prospective Gating for a single slice/single phase (mid-diastole) fast spin-echo sequence with an echo train length = 6. There is a long trigger delay (TD) between the R wave and the commencement of the pulse sequence with the initial 90° RF pulse. Dashed boxes around the QRS waves indicate the built-in arrhythmia reject window intrinsic to prospective gating (Figure adapted from [16])

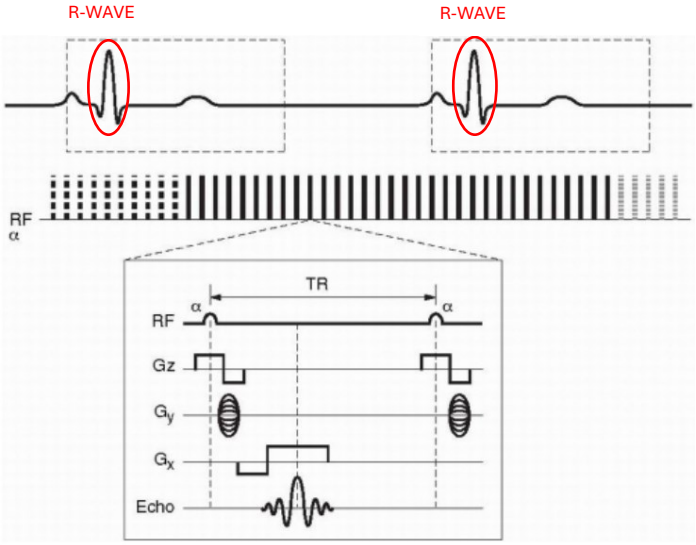

Figure 1.12. Retrospective gating for a single slice/multiphase cine sequence using a GRE pulse sequence. Notice the oversampling of the R-R interval of about 125% denoted by the different dashed or solid lines denoting a complete train of RF pulses contributing to a segment of k-space for the separate cardiac phases. There is no trigger delay as in prospective gating. Notice that the TR is much shorter in the GRE sequence than in the FSE sequence in (Figure 1.11). Lastly, the dashed box represents an optional asymmetric arrhythmia rejection

window (− 10% to + 50% expected R wave) whereupon an R wave detected outside of this box would result in rejection of the prior R-R interval's signals. (Figure adapted from [16])

1.3.5 Image formation

As explained in the previous section, the MRI signal of interest is the signal released as a result of a radiofrequency pulse. However, in order to transform the signal into an image that allows recognition of the anatomical and physiological characteristics of the tissue under examination, it is necessary to spatially encode the tissue itself, identifying the contribution of each individual point. This is accomplished by applying additional magnetic fields, which are called gradients and are distinguished as slice-encoding gradient, phase-encoding gradient, and frequency-encoding gradient (already illustrated in Figures 1.9 and 1.10) [12] .

1.3.5.1 Spatial encoding

To acquire an image of a particular slice of tissue, the scanner must excite nuclear magnetization only within that specific slice. This can be achieved by applying a radio frequency (RF) pulse in the presence of a magnetic field gradient such that it produces a linear change in the static field strength, B0, which gives rise to a spatial change in the value of the Larmor frequency. Only spins whose Larmor frequency exactly matches the frequency of the applied RF field will be excited. The slice thickness is determined by the bandwidth of the RF pulse and the amplitude of the magnetic field gradient. The position of each slice along the direction of the gradient is controlled by the frequency of the RF field: increasing the RF frequency excites the nuclei in a slice of tissue that corresponds to a higher Larmor frequency. Finally, the orientation of the slice is determined by the direction of the magnetic field gradient. After exciting nuclear magnetization in a desired slice of tissue, the position of the spins within the plane must be determined. This is achieved by exploiting frequency coding in one direction, and phase coding in the perpendicular direction. In frequency coding, a magnetic field gradient is applied during signal acquisition, and the position of the spins along the direction of the gradient can be identified by the frequency of their emitted signals (this is why the frequency coding gradient is also known as the readout gradient). In phase encoding, on the other hand, a magnetic field gradient is applied for a short period of time before data acquisition. This introduces a phase change between the spins, which is imprinted on their signals. To extract position information

from the phase, the process must be repeated many times with phase-coding gradients of ever-changing amplitude. The frequency and phase encoding directions are conventionally labelled x and y, respectively, while the slice crossing direction is labelled z. However, these labels are entirely arbitrary and are not related to the physical axes of the scanner or gradient coils [12] .

1.3.5.2 K-space

All collected data are recorded as a series of lines in a 2D matrix which is called 'K-space' (Figure 1.11). By applying a 2D Fourier transform to the K-space data, the spatial distribution of the signal is recovered. The resolution of the image in the phase-coding direction is determined by the number of k-space lines collected. It is useful to note that data in K-space can be interpreted as spatial frequency components of the image. This is because, data near the centre of K-space (k = 0) correspond to low spatial frequency components and represent the large-scale spatial structure of the image, whereas data near the outer edges of K-space correspond to high spatial frequency components and represent the fine structure of the image [12] .

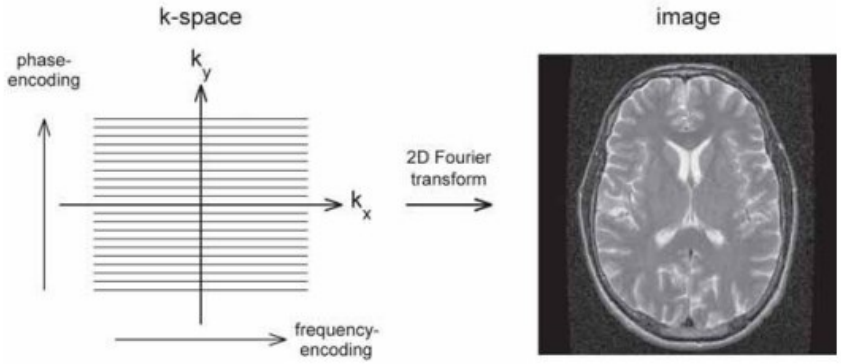

Figure 1.13. Example of image formation from K-space [12]

1.4 Iron overload-related pathologies and methods of diagnosis

Iron is an essential substance for human life and plays a major role in the transport of oxygen in the blood and in the respiratory activity of cells. Specifically, iron is bound to haemoglobin, a protein contained in red blood cells, which transports oxygen from the lungs to the body's tissues. There are several defects in globin, which result in pathological conditions that can be more or less severe, depending on the form in which they occur. Prominent among the various inherited diseases affecting iron accumulation is hemochromatosis, a condition in which the regulatory mechanism of iron metabolism is altered. Another rather common disease, not only in Italy but in the entire Mediterranean basin, is Thalassemia [17] . Thalassemia major (TM) is defined as that genetic disorder that involves the synthesis of haemoglobin and leads to a condition of anaemia. Without red blood cell transfusion, most patients die at an age of less than 10 years [18] . However, although transfusions have allowed a significant increase in life expectancy, the iron that is progressively accumulated with these clinical procedures leads to non-negligible biological disruptions, such as cell toxicity and tissue damage [19]. Iron accumulation mainly affects the liver, endocrine organs, and heart[20]. Iron deposition in the heart is greater in the ventricles than in the atria and is concentrated at the epicardium level. This phenomenon leads to cardiac problems, such as failure, arrhythmias and pericarditis [21], which are responsible for 71% of deaths in patients with Thalassemia [22].
It is useful to underline that iron is stored in the organs as ‘crystalline iron oxide’ within ferritin and haemosiderin [23]. Since the human body has no mechanism to physiologically excrete accumulated iron, it is necessary to resort to the administration of chelating agents, such as Deferoxamine and Deferiprone [21] to reduce the risk of morbidity and mortality. This type of therapy has been shown to be an effective treatment for iron reduction, but periodic measurements of accumulated iron in individual organs must be conducted to determine the correct dose of chelating agents to administer [19]. Monitoring of iron overload in the body should be performed continuously in all patients undergoing blood transfusion and chelation therapies. Currently, several methods are available for assessing the iron concentration of different organs, and many of these can be used in combination to make the diagnosis more accurate. The methods discussed below include those already used in clinical routine as well as those still under study and further investigation. Evaluation of iron accumulation can be done by laboratory analysis, determining, for example, ferritin concentration and degree of transferrin saturation, or by more invasive techniques such as biopsy of a tissue. Despite greater complexity and cost, computed tomography and quantum interference superconducting devices are also being tested.

1.4.1 Ferritin concentration

Ferritin is an intracellular protein that performs the function of iron storage and is able to bind it or give up it to the liver according to the body's needs. Ferritin is also present in the blood (serum ferritin), even if in modest amounts. This can be measured by analysis of a blood sample in the laboratory, revealing information about the amount of iron deposited. However, the relationship between serum ferritin and iron is not entirely known. Generally, a higher concentration of ferritin implies a greater accumulation of iron, but since this is an inflammatory protein, its concentration in the blood increases significantly in the presence of infection and/or inflammation, leading to an overestimation of the amount of iron present in the body [24]. In addition, another limitation is that this measure is not able to characterize the amount of iron relative to individual organs, providing a measurement that reflects a global level concentration [25]. It is important to distinguish between cardiac and hepatic iron concentrations, as iron metabolism has different mechanisms in the two organs. Normally, the liver is the organ that holds 70-80 % of the total iron stores in iron overload patients. Despite the limitations described, this method remains widely used due to the ease of performance and low cost associated with it [26].

1.4.2 Transferrin saturation

The role of Transferrin is to transport iron in the blood from the districts where it is absorbed (intestine) to all tissues that use it (especially the bone marrow, where red blood cells are produced) or to storage organs (like the liver). Currently, it represents the most specific serological screening marker for the recognition of primary hemochromatosis. The parameter of interest is not the concentration of Transferrin, but its degree of saturation, that is, the amount of iron bound to it. This is because a threshold above 85% [27] indicates that the amount of free iron is relevant. So, when the iron-binding capacity of transferrin is exhausted, free iron appears as non-transferrin bound iron (NTBI). The toxicity of NTBI is much higher than bound iron and promotes hydroxyl radical formation resulting in peroxidative damage to membrane lipids and proteins. In the heart, this leads to heart failure [23]. From a practical point of view, this measurement cannot be performed accurately if a circulating chelating agent is present, which is why frequent monitoring becomes more difficult to practice [24] .

1.4.3 Biopsy

Biopsy means taking a section of tissue, which can be evaluated in the laboratory to gain access to a histological assessment of the tissue itself and to a quantification of iron (the concentration of which is normally expressed in milligrams present in one gram of dry tissue). The organ that lends itself best to this type of operation is the liver, but the problems associated with this methodology remain several. As a first consideration, it can be easily observed that the invasiveness associated with this procedure limits the frequency of this operation. In addition, the distribution of iron in an organ appears to be quite heterogeneous, implying that the portion of the tissue examined may not be a good marker [24]. For example, in presence of significant fibrosis, the coefficient of variability can be as high as 40% [28]. Iron can also be assessed by endo-myocardial biopsy, but given the high degree of invasiveness, it is a procedure that is preferably avoided in medicine [21]. Besides, this technique has a limited sensibility, particularly in the initial stages, because the myocardial iron deposition is patchy and initially tends to be located in the sub-epicardial layer, with possibility of sampling errors [29] .

1.4.4 Computed tomography

Computed tomography is also one of the emerging techniques to track iron content accurately and reproducibly [30]. This is because iron increases X-ray attenuation in direct proportion to its concentration. Currently, there are two possible types of approaches, which are divided into single-energy and dual-energy techniques[24]. However, still few studies have been conducted with the dual-energy modality due to the limited availability of this type of scanner. Therefore, the use of computed tomography as an iron monitoring technique remains a challenge [25] .

1.4.5 Superconducting quantum interference devices (SQUIDs)

Quantum interference superconducting devices, known by the acronym SQUIDs, make it possible to measure the magnetic properties of a tissue, which will be affected by the amount of iron contained in the tissue, since iron is a paramagnetic substance. Despite the accuracy that these devices enable, their use is still limited to research studies due to complexity, cost, the need for frequent maintenance, and the need for experts who know how to accurately acquire measurements. Moreover, it is an approach currently reserved for the evaluation of iron in the liver and spleen [24].

1.5 Detection of iron through MRI

Given the limitations of other methods to diagnose and serially follow changes in iron concentration, MRI has emerged as a tool that overcomes most of the restrictions listed in the previous section (paragraph 1.4). During an MRI examination of iron overload assessment, the images generated are not measuring the iron molecule directly, but mostly through the indirect effect that iron produces in the local hydrogen protons. As explained in section 1.3.1, outside the magnet the hydrogen molecules present themselves with aleatory spin vector directions, producing no signal. In the presence of a magnetic field, these spins align with the direction of that field, generated by the scanner. To produce the image, a radiofrequency wave is produced, and the energy signal is captured in correspondence of an echo time (TE). The longer the TE time, the smaller amount of signal in produced owing to a dephasing effect. In a normal tissue without iron, more spins lose their coherence, and the image is progressively darker. In a tissue with a mild concentration of iron, the iron molecules affect the homogeneous field created by the MRI and disrupts the signal, therefore generating less signal within the same TE time as in normal tissue. So, it is possible to quantify a decay curve with many signal intensities at different TEs and estimate the concentration of iron within the myocardium, but also in the liver or endocrine organs (Figure 1.12) [25]. The procedure that allows to generate maps with the estimated parameters, as T1, T2, and T2*, is called parametric mapping. Currently, T2* imaging is the key technique to detect early iron deposition in the heart and to allow therapeutic changes that significantly impact the natural history of the disease.

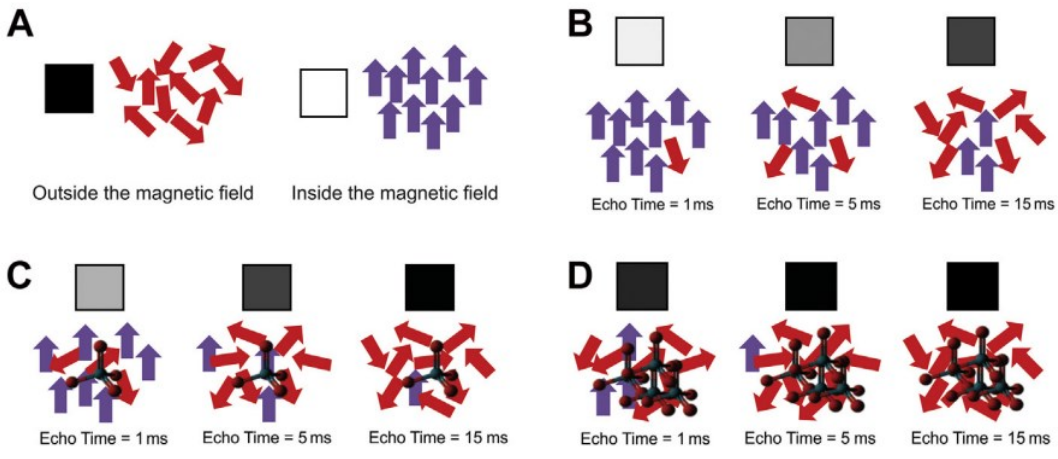

Figure 1.12. Illustration of how MRI measures iron in tissues. (A) Protons spin produce no signal outside the magnetic field (black box) but produce signal in presence of a magnetic field (white box). (B) Signal gets darker at longer TEs in a normal tissue. (C)(D) If there is iron in the tissue, the signal gets darker for the same TE time in a proportional way to iron concentration [25]

1.5.1 T2* parametric mapping

Parametric mapping is a pixel-wise map of magnetic relaxation parameters, which allows direct visualization and quantification of tissue properties. T1, T2, T2*, and extracellular volume (ECV) are the most frequently used parameters in MRI[31] . Multiparametric mapping of the myocardium has become an area of great interest in the recent year. Despite most of the focus initially on T1/T2 mapping, T2* mapping was the first clinically useful parametric mapping technique for the heart[23]. Before the introduction of T2* as a diagnostic tool, iron-induced cardiomyopathy was the most common cause of death in transfusion-dependent thalassaemic patients. It has been now more than 18 years since the initial applications of T2* images in iron overload assessment began to be performed and the accumulated knowledge gained from that has led to important practical changes in the diagnoses and treatment with the chelation. T2* is the current method of choice for the assessment of cardiac iron deposition, with proved evidence in reduction of overall mortality, improvement of life expectancy and fewer cardiovascular complications in transfusion-dependent patients[32] . T2* represents the decay of transverse magnetization caused by a loss of coherence between spins and magnetic field inhomogeneity. From the T2* equation showed in paragraph 1.3, it can be easily seen that T2* is more sensitive to magnetic inhomogeneity (and therefore, tissue iron deposition) than T2. T1 and T2 relaxation also decrease in the presence of iron compounds, but to a lesser degree [14]. It can be measured using gradient echo sequences, which offer two important advantages. Firstly, gradient echo images are more sensitive to tissue iron because they do not have a rephasing 180° pulse, which corrects for paramagnetic effects. Secondly, due to the rapid acquisition times, breath-hold images could be cardiac gated to minimize motion artifact from myocardial contraction, blood flow, and respiratory movement [33]. Usually, for cardiac imaging an additional electrocardiogram gating is exploited, and there are two validated and widely clinically used techniques divided into:

- Bright-blood technique: images are acquired immediately after the R wave to reduce artifacts caused by blood flow and myocardial wall motion; [34]
- Dark-blood technique: a double inversion recovery pulse is used to null the signal from blood; multiecho T2* acquisition is extended to late diastole with minimal cardiac motions technique. [35]

Dark-blood method has been shown to have superior interstudy, interscanner, and intercenter reproducibility and less artifact susceptibility, making it the preferred clinical technique.

Because the severe pathologic concentration of iron in the heart is more than 5 times lower than in the liver, myocardial T2* is usually easier to analyse [25] .

Often, instead of T2* relaxation time, the relaxation rate R2* is used, which is the reciprocal of the time constant:

$$R2^* = \frac{1000}{T2^*}$$

Where R2* is measured in Heartz (Hz) and T2* is measured in milliseconds (ms) [32].

As explained before, the presence of iron, which is a paramagnetic substance, influences the decay of a signal in a tissue: the greater the amount of iron accumulated, the lower the T2* value. This happens because paramagnetic particles create localized regions of magnetic field nonuniformity and cause nearby protons to lose phase coherence in a concentration dependent manner, thereby shortening transverse relaxation times. However, T2* and myocardial iron concentration are not linearly related, and this must be considered in assessing longitudinal changes in T2* values because significant changes in iron concentration occur when small variations are seen at low T2* values. The equation that allows to calculate myocardial iron concentration (MIC) knowing T2* value is the following:

$$MIC = \frac{45}{(T2^*)^{1.22}}$$

Where T2* is measured in milliseconds and myocardial iron concentration is measured in milligrams in 1 g of dry tissue [36].

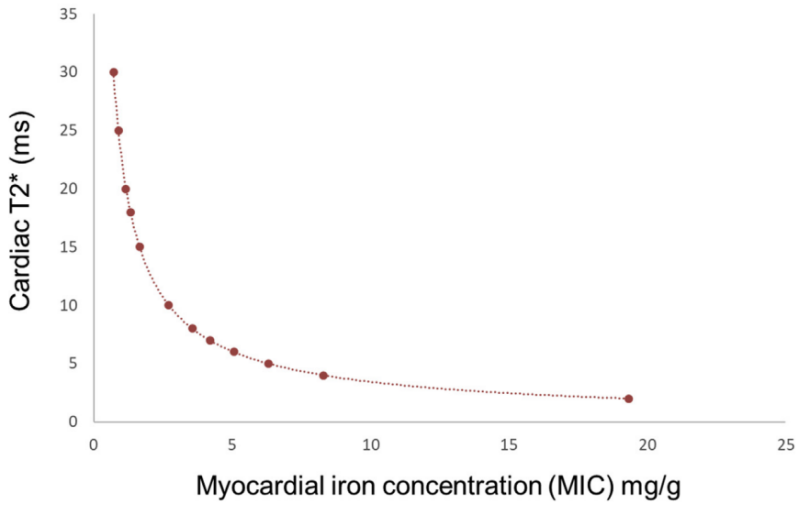

Figure 1.13 Graphical relationship between MIC and Cardiac T2* [24]

Considering MRI examinations performed at 1.5 T, a value of 20 ms in T2* has been traditionally associated with the normal cutoff for non-iron overload myocardial tissue, so all patients with T2* greater than this level do not develop reductions in left ventricular ejection fraction. If T2* values are between 10 ms and 20 ms there's a higher probability of developing myocardial dysfunction. T2* values below 10 ms indicate a severe condition and risk to develop heart failure increases dramatically when T2* shortens up to 4 ms [37]. These patients require intense chelation therapy and regular review. All these thresholds have also been approved by the American Heart Association [38]. It is important to underline that these ranges of values referred only to examinations conducted by a 1.5 T scanner. A more detailed classification of risks and complications, and correspondent cutoffs, are shown in Table 1.1, which also shows the difference with liver intervals [32].

T2*(ms) 1.5 T	**R2* (Hz) 1.5 T**	**T2* (ms) 3.0 T**	**R2* (Hz) 3.0 T**	**MIC/LIC (mg/g dw)**	**Classification**
Myocardium					
≥ 20	≤ 50	≥ 12.6	≤ 79	≤ 1.16	Normal
10-20	51-100	5.8 -12.6	80-172	1.16-2.71	Mild/Moderate
< 10	>100	< 5.8	>172	>2.71	Severe
Liver					
≥ 15.4	≤ 65	≥ 8.4	≤ 119	≤ 2.0	Normal
4.5-15.4	66 - 224	2.3 – 8.4	120-435	2.0-7.0	Mild
2.1 – 4.5	225- 475	1.05 – 2.3	436-952	7.0-15	Moderate
< 2.1	>475	< 1.05	>952	>15	Severe

Table 1.1. References values for myocardial and liver iron concentrations in MRI imaging [32]

1.6 Aim of the thesis

This work is the result of a collaboration between the information engineering department of the University of Padova and the radiology of Padova hospital. Under the supervision of Prof. Alessia Pepe and Dr. Amalia Lupi, a project to analyse magnetic resonance images of the heart and liver was outlined. In this thesis, we aim to explore and refine transverse T2* relaxation time estimation models with different approaches, as this is a crucial parameter for assessing iron overload in the myocardium tissue. The same methodologies were also applied in parallel to study T2* relaxation in the liver. Currently, HIPPO software is the tool used, in clinical research settings, at Padova Hospital for evaluating iron overload in patients with haemochromatosis, but it shows some limitations. These include reliance on manual myocardial segmentation, which slows down the analysis process, and exclusive use of the ROI-based approach, which makes it less effective in detecting heterogeneous iron distribution. In addition, the R2* correction factors used are derived from healthy subjects acquired at another centre[39]. So, the project was structured as follows:

- Implementation of T2* estimation models and best model selection
- Comparison of our results between all the different approaches and with those produced by HIPPO Software
- Development of new segmental correction factors, obtained from healthy subjects acquired in Padova
- Development of a new and updated type of myocardial segmentation

To sum up, the main objective of this work is to identify the most accurate model for myocardial T2* estimation and to compute a new R2* correction map that ensures accurate and reliable T2* measurements tailored to the specific parameters of Padova centre. So, this study aims to lay the foundation for developing a new tool for research purposes, with the potential for clinical application after the necessary validation, to replace or complement the current software.

CHAPTER 2 – STATE OF THE ART

2.1 Signal decay models

As introduced before, the multislice multiecho T2* approach has been validated as a good technique for the evaluation of segmental and global myocardial iron distribution. The dependence of the MR signal from echo times can be described through a multi-exponential decay, where each exponential represents the signal decay related to a particular tissue. So, plotting the MR signal of each myocardial voxel it is possible to recognize a decay curve, that could be described by a model. In describing this signal, there are different types of models present in literature [40]. The simplest model is the mono-exponential model:

$$S = S_0\, e^{-\frac{t}{T2^*}}$$

Where:

S= signal intensity

S_0 = initial amplitude

t= echo times

Nevertheless, the signal decay model may be affected by measurement errors. A small signal offset, almost constant over TEs, could be present due to Rician distributed MRI noise and signal from slow relaxing species oxygenated blood [41]. That means that Rician noise causes a drift of the signal amplitude. Although the signal correction with respect to this noise can be ignored in normal tissues because of the high signal-to-noise ratio (SNR), this issue becomes important in assessing T2* in heavily iron overloaded subjects [39]. In these kinds of subjects, the later TEs are usually subjectively excluded to take this aspect into account (Truncation Model). A valid alternative approach is to add a constant offset to the exponential curve, with the advantage of a reduced user-dependent variability. The offset is added to the equation to account for noise and artifacts [42]. However, this approach may not be optimal at high T2* values, such as those that characterize normal population, due to the incorrect estimation of the offset value [41]. The mono-exponential model summed with a constant C is the following:

$$S = S_0\, e^{-\frac{t}{T2^*}} + C$$

[40]. Another model, that is often proposed in literature to remove data with low SNR (last points), is the Truncation model. Usually, the last echo times are subjectively discarded by the

operator, and the remaining signal is fitted to a mono-exponential model. Nevertheless, an automatic truncation method is possible, exploiting R^2 value, which is a statistical measure of how well the fitted line approximates the real data points. The latter method consists in removing inaccurate points until R^2 value reaches a threshold equal to 0.995 [43]. A limitation is that this technique is only applicable in the ROI-based approach. Another possibility could regard the measurement of SNR value, removing all data points that represent images of SNR < 2 [44]. However, there are several techniques to estimate SNR in magnetic resonance images, but no precise method has yet been determined. Furthermore, the truncation model is suitable only when the signal exhibits a fast decay. Another alternative to the offset correction is the bi-exponential model. That is because, given the anatomical and chemical compartmentalization of the body's hydrogen protons [45] , multi-exponential transverse relaxation is expected of the various organs of the body. This is based on the idea that are two different tissue compartments: one described by a fast component (which is associated to a small T2* value) and one described by a slow component (which is associated to a higher T2* value) [46]. The model equation is:

$$S = S_{01}\, e^{-\frac{t}{T2_{1}^{*}}} + S_{02}\, e^{-\frac{t}{T2_{2}^{*}}}$$

Where S_{01} and T_{2_1} are the initial signal amplitude and T2* relaxation time of the first component, and S_{02} and T_{2_2} are the initial signal amplitude and T2* relaxation time of the second component. Another possible version involves incorporating a constant C (similarly to what is done with the mono-exponential), leading to:

$$S = S_{01}\, e^{-\frac{t}{T2_{1}^{*}}} + S_{02}\, e^{-\frac{t}{T2_{2}^{*}}} + C$$

For hereditary hemochromatosis patients, it has been demonstrated that transverse relaxation process within the iron-loaded liver is at least bi-exponential, but the results are different in the heart [46] . Myocardial tissue seems not to need the bi-exponential model as the differences obtained with the single-exponential model are minimal and negligible, and it is therefore preferable to use a simpler model with fewer parameters [40].

The last possible model that could be used in describing the MR myocardial signal is a linearized version of the single-exponential model. The decay curve can be logarithmically scaled:

$$S = S_0\, e^{-\frac{t}{T2^*}}$$

$$\ln(S) = \ln(S_0) - \frac{t}{T_2\,*}$$

$$\ln(S) = -\frac{1}{T_2\,*}TE\; +\; \ln(S_0)$$

It can be observed that the equation is now reduced to the form: $y = m\,x + q$ (linear equation). So, a linear best-fitting operation minimizing the X^2 error statistic can be performed to obtain the T2* value [39].

2.2 Myocardial Segmentation

For T2* analysis in the myocardium, the left ventricle is divided into 16 segments (Table 2.1) based on American Heart Association (AHA) segmented model [47]. Mean segmental T2* values are calculated by manually drawing endocardial and epicardial ventricular borders. To map T2*, the anteroseptal right ventricular connection of the left ventricular must be identified: the mid ventricular septum is the reference conventionally used as the starting point for division into segments. The myocardium is divided according to the cited model into six basal, six midventricular, and four apical regions of uniform arc lengths (Table 2.1 and Figure 2.1). In addition, global left ventricular T2* is usually calculated as the average over T2* over all 16 segments. A schematic representation of these standard segments is provided by the Bull's eye (figure 2.2): it has been developed as an important display for the visual and quantitative analysis of myocardial, to simplify the way of reporting the different values obtained from the T2* estimates (and similarly for T1 and T2) [48].

BASAL REGION	MID-VENTRICULAR REGION	APICAL REGION
1. anterior	7. anterior	13. anterior
2. anteroseptal	8. anteroseptal	14. septal
3. inferoseptal	9. inferoseptal	15. inferior
4. inferior	10. inferior	16. lateral
5. inferolateral	11. inferolateral	--
6. anterolateral	12. anterolateral	--

Table 2.1. 16-segment heart model: names of ventricular segments

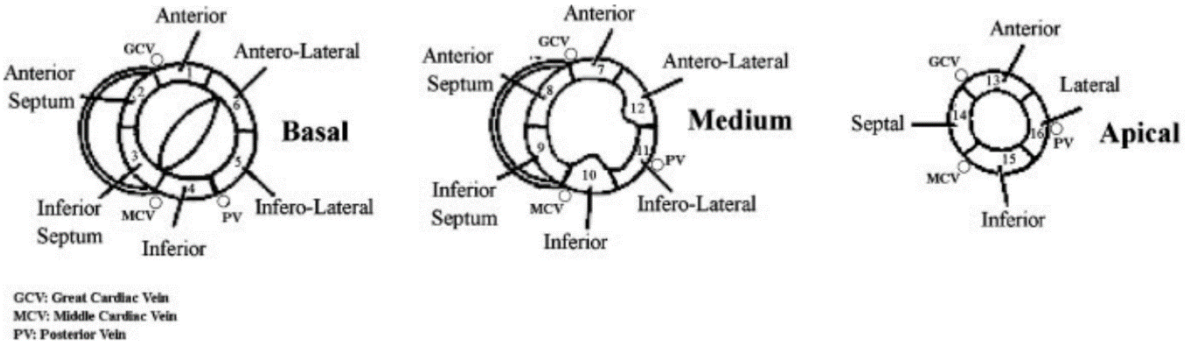

Figure 2.1. 16-segment heart model [39]

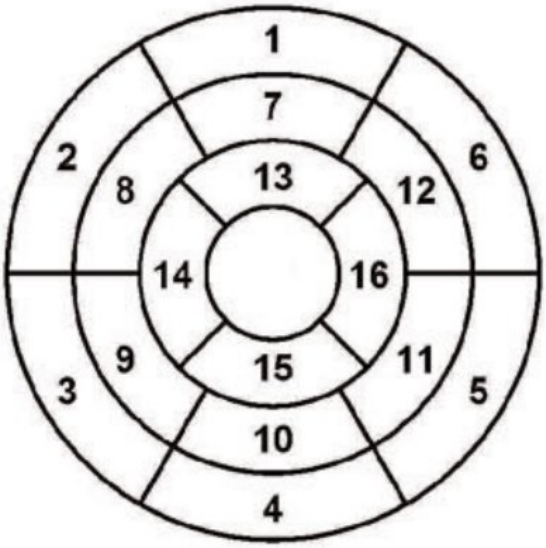

Figure 2.2. Bull's eye [48]

2.3 Artefact Modelling

Large cardiac veins and the heart-lung interface are the main sources of artefacts affecting T2* distribution in cardiac imaging. The large cardiac veins create perturbations in the z-component of the magnetic field due to the susceptibility difference between deoxygenated blood and surrounding tissue [49]which leads to artefactual alterations in T2* values. These artefacts reduce rapidly with distance from the veins, and their strength is influenced by the angle between the vein axis and the imaging slice. Figure 2.3 shows typical susceptibility artefacts at the basal (A), medium (B) and apical (C) regions. Consequently, artefact intensity varies

randomly among subjects and can be modelled as a Gaussian distribution, with the mean and standard deviation (SD) representing the systematic bias and variability in T2* segmental values. Heart–lung interface is another possible source of artefacts, as shown by means of qualitative analysis of pig hearts in vivo and ex vivo[50] . These artefacts were less important in human studies when measurements were performed in end-expiratory breath hold when phrenicomediastinal recess diminished [51]. Artefacts related to this source should involve a larger area with respect to 'spot-like' artefacts similar to the ones produced by cardiac veins. Figure 2.3(D) shows a typical artefact induced by the heart–lung interface. These artefacts could affect T2* measurements in the lateral wall and might be more severe in the apical region as compared with the base and the mid-ventricular level [41]. Besides, geometrical distortions originating from differences in the diamagnetic susceptibilities of different tissues can play an important role in T2* value distribution. These contributions are expected to operate at a macroscopic scale (up to centimetres) [46]. It should be noticed that the susceptibility artefact intensity depends on a large number of parameters, such as the angle between the axis of the vein and the acquired slice [49] . The presence of these artifacts has found to be minimal in the mid-ventricular septum (segment 8 and segment 9), hence the measurement of cardiac T2* has been limited to this location in clinical practice (see paragraph 2.3.1). It is still important to understand how imaging artefacts and distortions affect the measurement of iron deposition in the myocardium, and whether all the variations in T2* values should be interpreted as artifacts or whether a true inhomogeneity exists in patients with myocardial haemochromatosis [39].

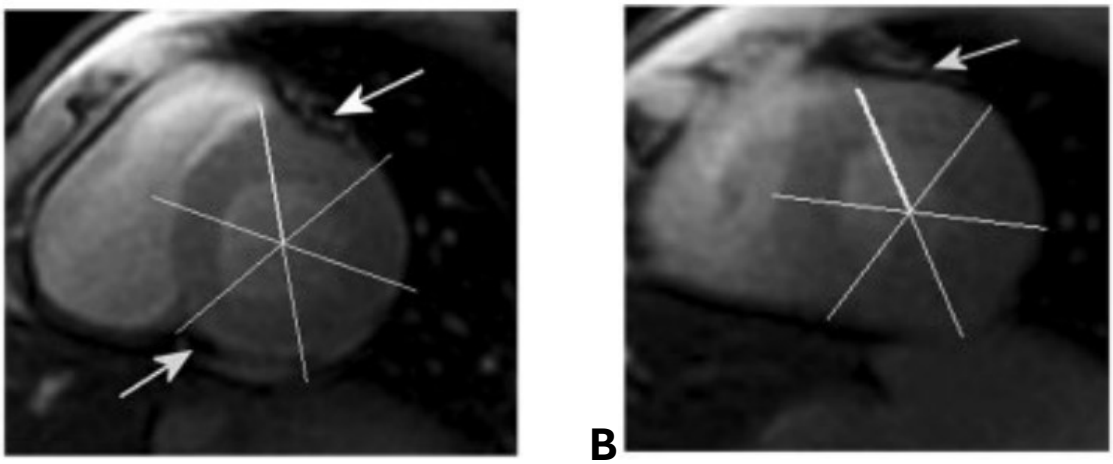

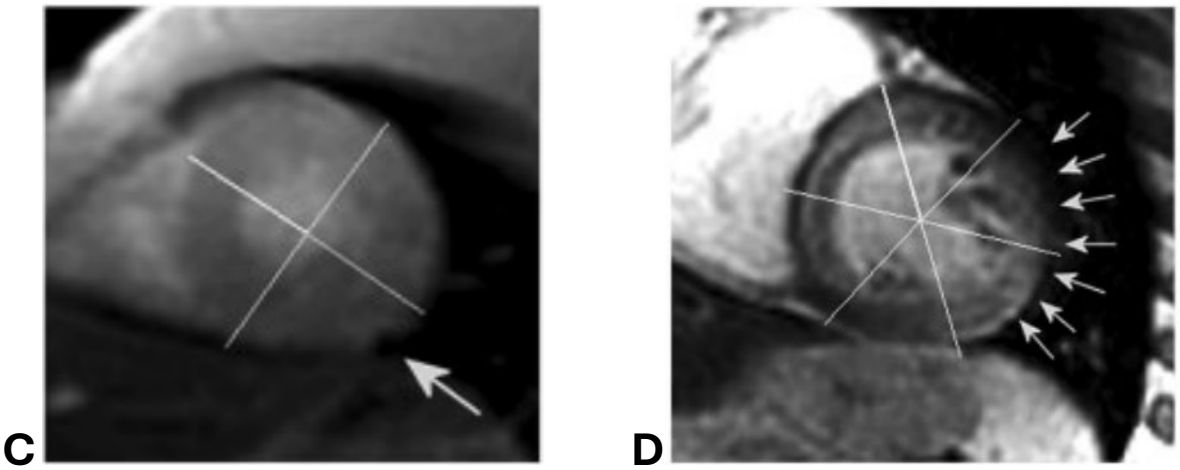

Figure 2.3. Mapping of segmental T2* distribution of the 16-segments model. Typical artefacts: cardiac vein (A-B-C) and heart-lung interface (D) [41]

2.3.1 Correction Factors

Due to the heterogeneous effect of susceptibility artefacts on different heart regions, the use of an R2* segmental correction map, evaluated on a normal subject, was proposed to partially overcome this drawback. Below, the procedure to obtain a T2* correction map, as implemented by Positano et al. in 2007, will be described [39] .

The measured relaxation rate $R2^*_{kj}$ of the myocardial tissue in a subject *j* and in a segment *k* can be expressed as the sum of three factors [46]:

$$\overline{R2^*_{kj}} = R2^*_{kj} \pm \Delta R2^*_{kj} + \Delta R2^{*\prime}_{kj}$$

Where $R2^*_{kj}$ is the true relaxation rate of the myocardial tissue, $\Delta R2^*_{kj}$ represents the deviation from R2* from point to point in the tissue, and $\Delta R2^{*\prime}_{kj}$ incorporates the averaged macroscopic variations in R2* due to contributions of the geometrical arrangement of tissues with different magnetic susceptibilities. Ignoring the term $\Delta R2^*_{kj}$ (since the segment is large enough with respect to the scale of the point-to-point variations), the true R2* value in a heart sector *k* for the j-th subject can be written as:

$$R2^*_{kj} = R2^*_j = \overline{R2^*_{kj}} - \Delta R2^{*\prime}_{kj}$$

$\Delta R2^{*\prime}_{kj}$ represents a correction factor that can be used to compensate for the systematic artefactual R2* variation in segment *k*. To evaluate $\Delta R2^{*\prime}_{kj}$, the above equation can be averaged among the sixteen segments (K=16) resulting in:

$$\frac{1}{K}\sum_{k=1}^{K} R2^{*}_{j} = \frac{1}{K}\sum_{k=1}^{K} \overline{R2^{*}_{kJ}} - \frac{1}{K}\sum_{k=1}^{K} \Delta R2^{*'}_{kj} \Rightarrow R2^{*}_{j}$$

$$= \overline{R2^{*}_{GJ}} - \Delta R2^{*\prime}_{j}$$

where $\overline{R2^{*}_{GJ}}$ is the global R2* value measured in subject *j*, and $\Delta R2^{*\prime}_{j}$ is the averaged effect of macroscopic artefacts of the entire heart of the j-th subject. After some substitutions, $\Delta R2^{*'}_{kj}$ can be written as:

$$\Delta R2^{*'}_{kj} = \overline{R2^{*}_{kJ}} - \overline{R2^{*}_{GJ}} + \Delta R2^{*\prime}_{j}$$

And this last equation can be averaged among N subjects, obtaining the mean value of $\Delta R2^{*'}_{k}$ to be used in the correction map:

$$\Delta\langle R2\rangle^{*\prime}_{k} = \frac{1}{N}\sum_{j=1}^{N}(\overline{R2^{*}_{kJ}} - \overline{R2^{*}_{GJ}}) + \Delta\langle R2\rangle^{*'}$$

The mean segmental correction factor $\Delta\langle R2\rangle^{*\prime}_{k}$ is defined as the sum of the averaged deviations of the measured R2* in a segment with respect to the global measured R2* value plus a constant factor $\Delta\langle R2\rangle^{*'}$, which is the global drift in R2* measurement. To evaluate $\Delta\langle R2\rangle^{*'}$, the macroscopic artefacts can be assumed to be minimal in the mid-ventricular septum: so, it is the common choice for R2* assessment. Besides, there is a good correlation between the global T2* value and the T2* value in the mid-ventricular septum, thus reinforcing the hypothesis that the septum is an excellent marker to represent the mean T2* of the whole myocardium [52]. Assuming $\Delta\langle R2\rangle^{*\prime}_{ms} = 0$ in the joined 8 and 9 segments, we have:

$$\Delta\langle R2\rangle^{*\prime} = \frac{1}{N}\sum_{J=1}^{N}(\overline{R2^{*}_{GJ}} - \overline{R2^{*}_{msJ}})$$

Hence, the correction factors are normalized with respect to the mid-ventricular septum value. It can be easily observed that substituting this last equation in the previous equation it is possible to obtain:

$$\Delta\langle R2\rangle^{*\prime}_{k} = \frac{1}{N}\sum_{j=1}^{N}(\overline{R2^{*}_{kJ}} - \overline{R2^{*}_{msJ}})$$

The correction factors $\Delta\langle R2\rangle_k^{*\prime}$ define the ‘‘segmental R2* correction map’’, which can be used to compensate for systematic artefactual variations in R2* measurements. The corrected T2 * values can be evaluated by transforming T2* values in the corresponding R2* ones, correcting the R2* values by subtracting the corresponding correction map values, and returning to T2 * notation. With the same approach, a “segmental radial R2* correction map” could be calculated to compensate for the R2* variations between endocardial and epicardial regions (under the hypothesis that the artefactual variation is minimal in the endocardium).

2.4 HIPPO Software Description

T2* mapping is widely regarded as the most effective technique for assessing iron levels in organs. At Padova Hospital, a specialized tool called HIPPO MIOT IFC-CNR is used to estimate T2* values. Developed in the IDL 6.0 environment, this software has undergone prior validation and is now commercially available [39]. This tool requires the manual selection of the endocardial and epicardial contours, thereby limiting the analysis to the myocardial region. After the septum is manually selected, the algorithm automatically divides it into equidistant segments (according to AHA segmentation). This procedure is repeated for the basal, mid-ventricular, and apical slices. At the end of each phase, the T2* values obtained for each segment are displayed. The model used is mono-exponential, allowing the operator to truncate the later echo times if deemed necessary. The number of echos to be excluded is also subjective and determined based on the provided data. The approach employed for T2* estimation is ROI-based. Finally, the software applies a correction to the T2* values obtained for each segment. The segmental correction map applied, shown in Table 2.2, was derived from a previous study conducted in Pisa in 2006 [39]. The dataset exploited to calculate these factors were composed of 22 healthy subjects. Images were acquired using a GE scanner at 1.5 T, using fast gradient-echo multi-echo sequences. However, it is important to highlight differences between Pisa and Padova Scanner (Table 2.3), since all these factors have an impact in images results. Besides, in HIPPO Software, a threshold of 60 ms is applied to the T2* values displayed in the final corrected segments. This threshold was chosen because T2* values exceeding 60 ms are not considered physiologically relevant. Moreover, since the primary objective is to detect iron presence, any segment with a T2* value greater than 60 ms can be classified as free of iron overload. All segmental values are presented in a Bull’s eye diagram and rounded to the nearest integer. Moreover, a pixel-wise map is provided, highlighting pixels with T2* values below 20 ms. These regions indicate moderate to severe iron overload

Segment	Correction Factor – R2*(Hz)
1	+4.7
2	-0.7
3	-1.0
4	+7.7
5	+3.3
6	-2.3
7	+6.9
8	+0.3
9	-0.3
10	+4.6
11	+0.6
12	+1.3
13	+6.1
14	-2.2
15	-0.2
16	-2.2

Table 2.2 Segmental Correction Map [39]

Parameters	**PISA**	**PADOVA**
Echo times	9 TE (2.2 – 20.3) ms	10 TE (2.02 – 22.36) ms
Echo spacing	2.26 ms	2.26 ms
Bandwidth	62.5 KHz	208 KHz (= 814 Hz/Px * 256)
Spatial Resolution	1.37 mm	1,27 mm
Parallel Imaging	---	GRAPPA
Number of excitations	0.75	1
Flip angle	25°	25°
Slice thickness	8 mm	8 mm

Table 2.3 Differences between Padova and Pisa acquisitions

2.5 Reproducibility of Parametric Mapping of the Heart

As explained in the introduction, in recent years, parametric mapping has seen a steady increase in use in the clinical setting. The relaxation times are quantifiable properties of a tissue in a magnetic field, and strongly depend on physiological properties of that tissue. This leads to large advantages of parametric maps over qualitative imaging, since these maps should no longer be dependent on scan-specific parameters such as radiofrequency (RF) coil proximity, receiver chain efficiency, or magnetic field inhomogeneities. Quantified relaxation times also reduce interobserver variability, allow for a patient's tissue parameters to be tracked through therapy, and allows for individual patient values to be compared. In theory, these parameter maps should thus be highly reproducible, since they only depend on the interaction of physics and biology. Unfortunately, while parametric mapping can indeed uniquely and quantitatively inform on tissue properties such as interstitial fibrosis and iron deposits, most mapping techniques are in practice not as independent of confounding influences as described above. Different vendors and even different scanners at the same magnetic field strength in the same hospital often led to different baseline relaxation times. Because of these differences, the latest international consensus statement on parametric mapping of the heart [53]recommends establishing reference values in healthy volunteers for each mapping technique, scanner, and hospital. Similarly, recent international guidelines on CMR reference ranges report broad vendor-specific reference ranges [54]. This indicates that parametric mapping is currently reproducible at the level of the individual MR scanner, but that relaxation parameters can often not be directly compared between different mapping techniques, or between different hospitals. Figure 2.4 shows the sources of bias and variability in the myocardial mapping workflow. Not all factors contribute significantly to mapping techniques, but any relaxation time is the result of combination of the subject, hardware, acquisition, reconstruction and map analyses used so each step contributes to increasing uncertainty [14].

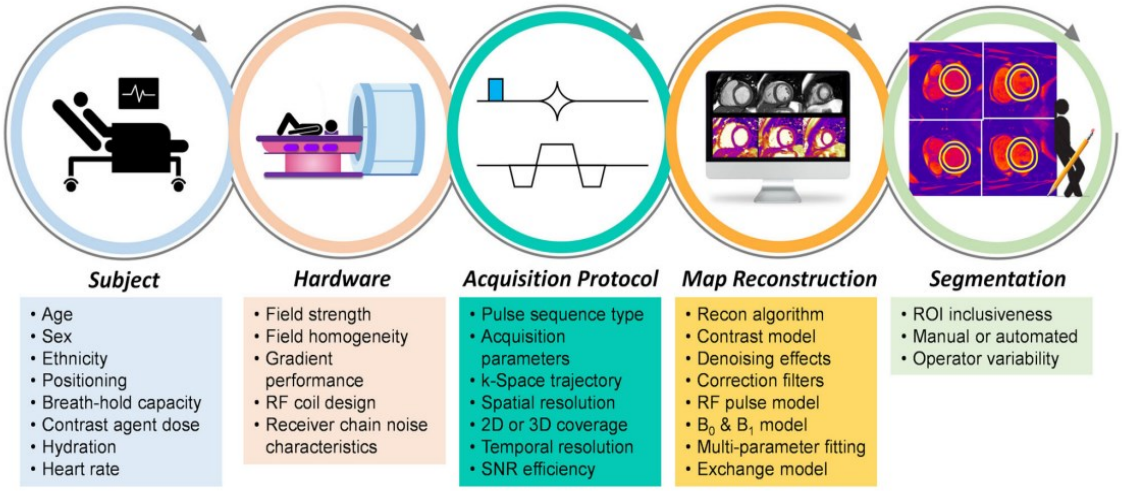

Figure 2.4. Sources of variability in myocardial mapping results. [14]

CHAPTER 3 – MATERIAL AND METHODS

3.1 Datasets

In the current work two Datasets were tested, in to analyse both healthy subjects (Dataset 1) and patients affected by Haemochromatosis (Dataset 2). All data were provided from Padua's Radiology. The study was conducted in accordance with the Declaration of Helsinki. All subjects signed an informed consent and received information about the protocol carried out. Image acquisition was performed with a Siemens MAGNETOM Avanto Fit scanner (software: syngo MR VE11C) at 1.5 T. For T2* mapping, three parallel short-axis sections (basal, middle and distal) of the left ventricle were acquired with black blood Multi-Echo Gradient Echo (MEGE) sequences with breath-hold at end-expiratory and by cardiac gating in telediastole. A detail description of the datasets is provided below:

- DATASET 1: Fifty healthy subjects were prospectively enrolled between November 2021 and May 2022. Patients underwent CMR in May 2022. Inclusion criteria were age between 20 and 69 years, absence of cardiovascular risk factors, negative history of symptoms, cardiovascular or systemic disease or Sars-CoV-2 infection within the last 3 months, Sars-CoV-2 vaccination course completed at least 3 months earlier, recent (within the last 3 months) negative electrocardiogram and absence of absolute contraindications to MRI. The above-mentioned criteria were verified by anamnestic collection, supplemented by a lifestyle questionnaire, an anthropometric analysis and the performance of an electrocardiogram, if not available. In the event of exclusion, due to failure to meet all the above criteria, or due to the finding of pathological findings on the MRI scan, the subject concerned was replaced by another of the same sex and age group. One subject was excluded due to an improper images acquisition of the apical slice.
- DATASET 2: Ten patients underwent cardiac MRI for suspected iron accumulation. The age ranged from 12 to 81 years, 3M/7F. Four subjects have the HFE gene mutation responsible for haemochromatosis and five subjects have thalassaemia major. All patients are regularly treated. One subject was excluded due to an improper images acquisition.

All technical data concerning the acquisition protocol are summarised in Table 3.1.

Scanning Parameters	Dataset 1-2
First echo time (ms)	2.02
Last echo time (ms)	22.36
Echo spacing (ms)	2.26
TR (ms)	Variable
Flip-angle	25°
Bandwidth (Hz/Px)	814
FoV read (mm)	400
FoV phase	81.3 %
Base Resolution	256
Phase Resolution	60%
Thickness (mm)	8
Spacing (mm)	Variable
Number of excitations	1
Echo numbers	10
View per segment	13
R-R	1
Parallel imaging	GRAPPA

Table 3.1. Description of scanning parameters of acquisition protocol for datasets 1,2.

3.2 Preprocessing

This MRI scanner acquires images by saving them in DICOM *(Digital Imaging and COmmunications in Medicine)* format (.dcm), the standard image format generated by modern medical imaging devices. Each magnitude image, given by the signal at each echo time, was converted to NIfTI (*Neuroimaging Informatics Technology Initiative*) format (.nii), using the available '*dcm2niix*' package (available here https://github.com/rordenlab/dcm2niix), which is designed to convert imaging data from the DICOM format to the NIfTI format. Besides, it allows to save *json files (JavaScript Object Notation Files)*, which contain useful information about the acquisition settings. With the resulting NIfTI files, a merge of the data from the different echo times was performed for each subject, using the '*fslmerge*' function

(command in FSL: FMRIB Software Library - https://fsl.fmrib.ox.ac.uk), to create a 4D-matrix structured as follows:

- first dimension: number of frequency encoding step of a single slice (Nx)
- second dimension: number phase frequency encoding step of a single slice (Ny)
- third dimension: number of slices (Nz)
- fourth dimension: number of echoes in the sequence (Nt)

The resulting 4D-matrix (Nx *x* Ny *x* Nz *x* Nt) contains the data that will be used to test the implemented models.

3.3 Models implementation

This part of the study describes the implementation of the models employed to estimate T2* descripted in paragraph 2.1:

- Single-exponential model (S-EXP)
- Single-exponential model summed with a constant (C-EXP)
- Bi-exponential model (B-EXP)
- Linearized single-exponential model (LIN)

All models were implemented using Python 3.14 (64 bit), exploiting modules of the Standard Library such as: Nibabel, Os, NumPy, SciPy, Json, Matplotlib. The structure of the models is the same for both Database 1 (healthy subjects) and Database 2 (patients). The models described were implemented through two different approaches: i) In the pixel-wise approach, T2* values are calculated individually for each voxel within the image, resulting in a detailed spatial map that captures localized variations across the tissue. In this way, it is possible to obtain a T2* map, which describes T2* value in each point. Then, in each segment, an average of all T2* values which belong to that specific segment is calculated. In some cases, also median T2* values of each segment were analysed. In contrast, ii) the ROI-based approach calculates a single average T2* value in each segment. So, the original MR signal is averaged over multiple voxels. A comparison of all these results were performed to evaluate differences in terms of reliability and interpretability.

3.3.1 Exponential models

The 4D-matrix was loaded, and the parameter estimation was performed using '*curve-fit'* function (from *'scipy. optimize'* module), which uses non-linear least squares to fit a function to data:

Parameters_opt, Parameters_covariance = curve_fit (exponential_decay_function, time_vector, original_signal_intensities, initial_guess, bounds, method)

The meaning of all the parameters indicated here is listed in table 3.2:

Parameters_opt	Optimized parameters resulting from the fit
Parameters_covariance	The estimated approximate covariance of *Parameters_opt*. The diagonals provide the variance of the parameter estimates
Exponential_decay_function	Function which models the exponential decay of signal intensity
Time_vector	Echo times
Original_signal_intensities	Data coming from each voxel of 4D-matrix
Initial_guess	Initial estimation values used to perform the fit
Bounds	Lower and upper bounds on parameters
Method	Method to use for optimization

Table 3.2. Description of parameters required in '*curve_fit*' function

The initial estimates, upper and lower bounds, and optimization algorithms vary depending on the type of exponential model being implemented. For the bi-exponential model, the initial values for amplitudes and T2* relaxation times are chosen to differentiate between the fast and slow components. It is assumed that the fast component has a higher initial amplitude than the slow component, and since its signal decays more rapidly over time, it is associated with a lower T2* relaxation time than the second component. The bi-exponential model is expressed as the sum of these two components. As explained in Section 2.1, the bi-exponential model has been rarely tested on the heart, and no specific initial values or implementation methods are available in the literature. Therefore, the choice of parameters is based on different combinations tested during the study. For the C-EXP model, the selected values are based on the study conducted by Positano et al. in 2007 [39]. For the S-EXP model, the initial value of the T2* relaxation time was chosen to be equal to the conventional cutoff (0.02 s) used to discriminate the presence

of cardiac iron overload. The initial amplitude used by the estimation algorithm is set to the signal value acquired at the first echo time. Additionally, for the S-EXP model, which does not require specific constraints, the Levenberg-Marquardt (*'lm'*) algorithm is used. This standard method for solving non-linear least squares problems is a hybrid between the Gauss-Newton method and gradient descent. However, it does not support parameter bounds. On the other hand, some constraints are necessary for the C-EXP and B-EXP models. In these cases, the optimization algorithm used is the Trust Region Reflective (*'trf'*) method. This method solves non-linear least squares problems by iteratively improving the solution within a trust region around the current estimate. During each iteration, the size of the trust region is adjusted based on the progress of the optimization. It is suitable when dealing with constraints on the parameters to be estimated.

All specific details regarding the implementation of parameter estimation through the three exponential models are summarized in Table 3.3.

	S-EXP	**C-EXP**	**B-EXP**
Optimized Parameters	S0; T2*	S0; T2*; C	S0_1; T2_1*; S0_2; T2_2*
Exponential decay function	$S = S0\ e^{-\frac{TE}{T2*}}$	$S = S0\ e^{-\frac{TE}{T2*}} + C$	$S = S0\_1\ e^{-\frac{TE}{T2\_1*}} + S0\_2\ e^{-\frac{TE}{T2\_2*}}$
Initial guess	S0= signal at first echo time T2*= 0.020 s	S0= signal at first echo time T2*=0.035 s C=0	S0_1= (2/3) signal at first echo time T2_1*= 0.020 s S0_2= (1/3) signal at first echo time T2_1*= 0.040 s
Bounds	--	S0 = [0; inf] T2*= [0; inf] C= [0; signal at last echo time]	S0_1=S0_2 = [0;400] T2_1* = T2_2* = [0; 0.15 s]
Method	Levenberg-Marquardt (*'lm'*)	Trust Region Reflective (*'trf'*)	Trust Region Reflective (*'trf'*)

Table 3.3. Summary of values and methods used for S-EXP, C-EXP, B-EXP models in performing the fit to the acquired data

3.3.2 Linear Model

To implement the linearized model a different structure was followed. To linearize the exponential model, a logarithmic scale was applied to all the signals. Using this transformed signal, the least squares estimation method was applied to obtain the parameters that define the equation: $y=mx+q$ (as described in Section 2.1). The implementation of the linear least squares method is carried out using the '*linalg.lstsq*' function from the *NumPy* Python library, which returns the least-squares solution to a linear matrix equation:

coeffs, rss, rank = np.linalg.lstsq (Coefficient_Matrix, Data, rcond)

Where all the parameters are described in Table 3.4.

Coeffs	Least square solution: values of slope coefficient (m) and intercept (q) of $y=mx+q$ equation
Rss	Sums of squared residuals
Rank	Rank of *Coefficient_Matrix*
Coefficient_Matrix	Echo times vector and all-ones vector
Data	Ordinate or "dependent variable" values: logarithmic signal
Rcond	Cut-off ratio for small singular values of *Coefficient_Matrix*: not necessary in this implementation

Table 3.4. Description of parameters required in '*np.linalg.lstsq'* function

So, the system is given from the following matrices product:

$$\underbrace{\begin{bmatrix} TE_1 & 1 \\ \vdots & \vdots \\ TE_{10} & 1 \end{bmatrix}}_{Coefficient\_Matrix} \cdot \underbrace{\begin{bmatrix} m & q \end{bmatrix}}_{Coeffs} = \underbrace{\begin{bmatrix} Log\_signal_1 \\ \vdots \\ Log\_signal_{10} \end{bmatrix}}_{Data}$$

After obtaining the values of *m* and *q* estimated by least squares, it is necessary to perform the inverse operations to derive the values of the parameters of interest (T2* and the amplitude of the initial signal):

$$\ln(S) = \underbrace{-\frac{1}{T_2*}}_{\text{m}} TE + \underbrace{\ln(S_0)}_{\text{q}}$$

$$T2^* = -\frac{1}{m} \qquad S_0 = e^q$$

So, T2* is equal to the anti-reciprocal of the slope m, and S0 is the exponential form of the intercept *q*.

3.3.3 Smoothing models

All models described were implemented also in a smoothed version. In this version, it was not taken the single signal intensity of the voxel in exam, but the signal was evaluated along all echo-times values in a 3x3 region surrounding the voxel, to obtain a mean signal (see Figure3.1). The mask is also designed to treat voxels in the image borders considering only signals from adjacent voxels. However, the myocardium is in a central position, so how to handle the outer voxels is not of interest in this work. After obtaining an averaged signal, this was used in the same way of the original signal described in the implementation of exponential models and linear model (Paragraph 3.3.1 and Paragraph 3.3.2). So, this mean vector is used as input in the *curve_fit* function (in substitution of '*Original_signal_intenstities*') to estimate T2* in non-linear models, while, its logarithmic version is the input in '*linalg.lstsq'* function ('*Data*' parameter).

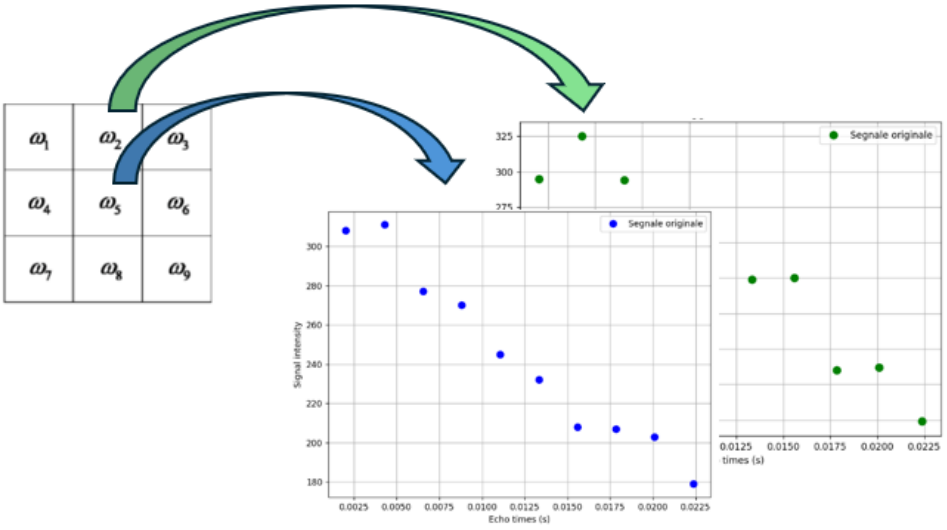

Figure 3.1. Example of how to obtain mean signal intensity in a 3x3 mask. The *w5*-voxel mean signal was obtained averaging with the 8 surrounding signals equally weighted, to obtain a unique signal in the correspondant voxel that will be used in the estimation algorithm. Images refer to a myocardial voxel in apical region of subject 1 (Dataset 1).

In image processing, estimating the value of a parameter in a single voxel by averaging the signals from the surrounding voxels can enhance the accuracy and reliability of the estimate. Data acquired from medical imaging often contains noise, especially at fine resolution levels. Calculating the average from neighbouring voxels helps in reducing the impact of random noise, as noise tends to be randomly distributed and partially cancels out when averaged. So, averaging among neighbouring voxels introduces a smoothing effect, which helps reduce high-frequency artifacts and provides visually smoother images. However, this also results in some loss of fine details.

3.4 Coefficient of variation associated with T2* estimates

Some operations common to all implemented were performed to generate T2* maps that are more readable. Firstly, all the estimation functions were executed inside a try/expect Python block, to handle errors in the fit and to eliminate voxels in which the MR signal is not recognised, and thus parameters cannot be estimated. In addition, for each voxel, a further check was placed by calculating the covariance matrix associated with the estimated T2* values. In the exponential models, the covariance is calculated by the *curve_fit* function, whereas in the linear model it was manually calculated:

$$Covariance\ Matrix = \frac{residuals^T \cdot residuals}{n-p} \left(Coefficient_{Matrix}{}^T \cdot\ Coefficient_{Matrix}\right)^{-1}$$

Where *residuals* are the difference between real signal and estimated signal, *n* is the number of observations (equal to the number of echo times) and p is the number of parameters. In all models, from the covariance, the standard error (SE) and the coefficient of variation (CV) can be obtained:

$$SE = \sqrt{diag(Covariance\_Matrix)}$$

$$CV = \frac{SE}{estimated\_value} \cdot 100$$

In this context, the estimated value refers to the T2* value in exponential models and to the slope *m* in linear models. Since high CV values indicate noisy and unreliable estimates, a threshold was set to discard poorly fitting T2* values. By excluding T2* estimates with high CV values, we improve data accuracy, reduce noise, enhance the quality of the model fit, and ensure more consistent results across voxels. This leads to more reliable and robust conclusions in the analysis. The threshold was tested more times to see how T2* analysis changes. Specifically, a CV percentage threshold of 1000 and a CV percentage threshold of 10 were analysed. A CV threshold on initial amplitude of the signal (S0) was not applied.

3.5 Myocardial Segmentation

Myocardial segmentation was performed using MATLAB R2023b, utilizing the first echo time image for each subject, as it provides the clearest anatomical structures. The segmentation was manually executed using the *roipoly* function, which allows for precise tracing of the region of interest (ROI), by defining the epicardial and endocardial contours. To identify the sixteen myocardial segments, the mid-ventricular septum was selected, with the help of a radiologist, since this is the reference point for subdivision. This was used as the starting point for dividing the myocardium into equidistant and equiangular segments, following the AHA convention (as described in Section 2.2). The segmentation was performed automatically by drawing line between the septum and the barycentre ('*centroid*' parameter of *roipoly* function) of the circular region. The resulting ROI mask is numbered 1-6 for basal segments, 7-12 for mid-ventricular segments, and 13-16 for apical segments.

3.6 Best model selection

The evaluation of models fit were performed through the application of *Bayesian Information Criterion (BIC)*, which is one of the most widely used tools in statistical model selection because of its computational simplicity and effective performance in many modelling framework. It makes a trade-off between the goodness of fit and model complexity. BIC is based on Bayesian principles and provides a stronger penalty for model complexity compared to *Akaike Information Criterion (AIC)*[55] . The formula to calculate BIC is as follows:

$$BIC = -2\ln(L) + k\ln(n)$$

Where L represents the maximized likelihood of the model, k is the number of parameters in the model and n is the number of observations. However, in the current analysis a simplified version of this criterion was used. The residuals sum of squares (RSS) were used instead of the Likelihood, leading to the following equation:

$$BIC = n\log\left(\frac{RSS}{n}\right) + k\ln(n)$$

In a model selection application, the chosen model is identified by the minimum value of BIC. In this work the comparison involves mono-exponential model, mono-exponential model with constant added, and linearized model. The number of observations (n) is equal to 10 in all models since it is the number of echo times, while the number of parameters (k) changes according to the structure of the model (Table 3.5).

Model	**Number of Parameters (k)**	**Types of parameters**
S-EXP	2	S_0, T2*
C-EXP	3	S_0, T2*, C
LIN	2	S_0, T2*

Table 3.5 Parameters of models

A Bayesian Information Criterion (BIC) value was calculated for each voxel within the myocardial region, slice by slice. This analysis was performed in both Datasets. After obtaining the BIC values, the relative performance of the models was assessed, by calculating the percentage of voxels in which one model is better than the others (which means having the lowest BIC value). To add spatial specificity, this percentage was divided across sixteen myocardial segments. This calculation was conducted in each subject to capture individual

prevalence patterns. The results were then aggregated across all subjects, keeping the segmental divisions, allowing a collective analysis of model prevalence across the myocardial segments. All these results were visualized in histograms.

3.7 Test-retest in Patients

In this study, Dataset 2 images were acquired twice (test-retest) for each of the 10 patients to evaluate the reliability and reproducibility of the imaging protocol. All scans were performed under standardized conditions, using the same scanner, acquisition sequence, and bandwidth. Additionally, the same radiologist carried out the segmentation to minimize inter-operator variability. This test-retest approach ensures that metrics such as T2* relaxation times are consistent, unaffected by technical variability or noise. Statistical comparisons between the two acquisitions, as detailed in one of the following paragraphs, validate the robustness of the protocol.

3.8 Segmentation of the myocardium adapted to the mid-ventricular septum

Myocardial segmentation conventionally divides cardiac segments into equidistant and uniform parts. However, the heart has a structure that varies from subject to subject, depending on genetics, gender or age. For this reason, such a geometrically guided segmentation may not be accurate in some cases. For example, segments number 8 and number 9 must cover the entire length of the mid-ventricular septum. For this reason, a procedure was implemented to select manually both the beginning of the septum (as in standard segmentation) and the end point. In this way, segments 2 and 3 of the basal slice, 8 and 9 of the mid-ventricular slice, are divided into two equal parts. As a result, the remaining arch is divided into four uniform and equally spaced segments. The apical region needs a different segmentation. In this case there is only one septal segment (number 14), and the remaining myocardium tissue is divided into three qual segments. Again, the segmentation in segments was performed automatically in MATLAB R2023b. This method performs the subdivision in sectors starting from the barycentre of the mask (previously segmented by drawing manually endocardium and epicardium). The resulting ROI mask is numbered 1-6 for basal segments, 7-12 for mid-ventricular segments, and 13-16 for apical segments.

3.9 Correction Factors

3.9.1 Correction Factors calculation and robustness of the methodology

The T2* correction map was created using the procedure described in the previous chapter. Segmental factors were calculated using data from Dataset 1 (healthy subjects). One subject was excluded due to improper image acquisition and the lack of visibility in the apical region. The average T2* values for each segment were determined using the mono-exponential model. Both the pixel-wise approach (ensuring coefficients of variation remained below 10%) and the ROI-based approach were employed to assess how these methods influenced the results. Besides, also T2* median values were considered in pixel-wise approach, to evaluate possible differences with T2* mean values. For the mid-ventricular septum, R2* values (in Hz) were calculated separately for segments 8 and 9, and their mean value was taken as the R2* reference. For each subject, the difference between the R2* value of each segment and the R2* of the septum, which is the reference, was calculated. These differences were then averaged across all subjects. Finally, we produced a series R2* correction for each method.

3.9.1.1 Error in septum identification: fixed and random rotation

Since the septum's identification is performed manually, a simulation was conducted to assess how varying the orientation of the segmentation mask impacts the correction factors. To simulate a systematic bias in septum identification, rotations of 2°, 5°, 10°, and 20°, in both clockwise and anticlockwise directions, were tested to evaluate the potential errors introduced by operator variability and the influence of intersubject variability. We also tested a non-systematic error, since the operator in the selection phase theoretically might introduce a random rotation. The rotation angle was randomly selected between -10° and 10° in 1° steps to simulate different error scales. This analysis provides insight into the robustness of the correction methodology under conditions of septum identification errors.

3.9.1.2 Sample size effect in the healthy subjects group

In addition, an analysis was carried out to examine the effect of subgroup selection on the calculation of segmental factors. The healthy subjects were divided into five groups, each containing ten individuals. For each group, the sixteen segmental factors were calculated and compared. As each factor was calculated in terms of R2*, this value must be subtracted to the original R2* value of each segment, and then the data must be converted back to T2* (from seconds to milliseconds) [39]:

$$T2^*_{COR} = \frac{1}{R2^*_{NO\_COR} - CF}$$

In this way, a standardized T2* correction map was obtained. The effect of all these forms of correction were evaluating setting each T2* mean estimated value to 20 ms, which is the cutoff conventionally used to determine if there is myocardial iron-overload. So, considering T2* of 20 ms, we applied the correction factors to study if this application induces an increasing T2* values or a reduction of T2*values. All the investigations described highlight the sensitivity of the correction methodology to errors and underscores the importance of considering these factors in the clinical interpretation of T2* outcomes.

3.9.2 Application of Correction Factors in Patients

We want to investigate the effect of the correction maps calculated with the two different types of segmentations (described in paragraph 3.5 and 3.8). To perform this evaluation, T2* mean values estimated in Patients (Dataset 2) were submitted to the correction factor map. The procedure was the following: T2* values were calculated in each segment in both pixel-wise (considering T2* means of all voxels of the specific segment) and ROI-based approach. Then, the correction factors were applied in the same modality explained above (3.9.1). The following diagram summarises the process (Figure 3.2).

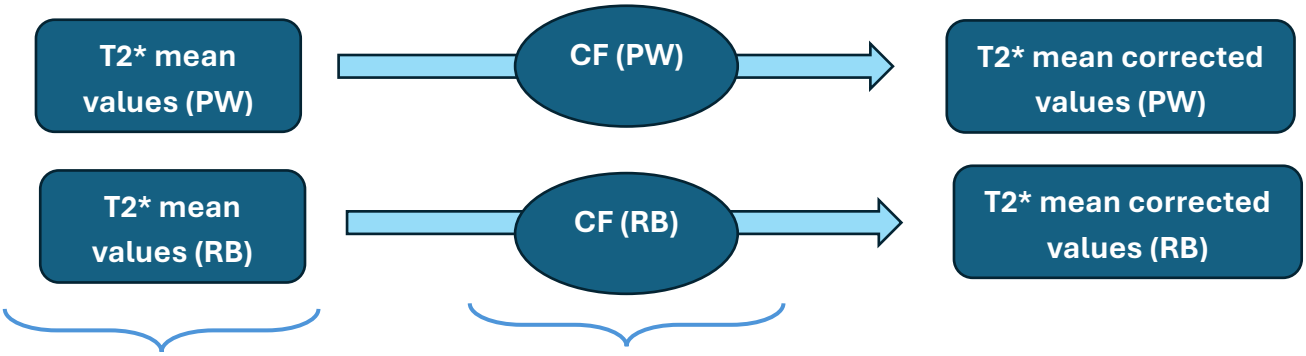

Figure 3.2. Summary scheme to illustrate the correction procedure. Correction Factors (CF) calculated from Dataset 1 with both pixel-wise approach (PW) and ROI-based approach (RB), were respectively applied to T2* values obtained from S-EXP model results in patients. All these steps were performed firstly with the standard segmentation and repeated in the same way with the new segmentation data.

3.10 Statistical Analysis

3.10.1 Student T-Test

To compare all the results obtained in T2* estimation from different models several tools were exploited. Firstly, to assess the statistical significance of differences between T2* global mean value across all subjects, a paired T-Test was applied. This test was applied in each segment to compare smoothing and non-smoothing in S-EXP, C-EXP, LIN models. To perform this analysis '*ttest_rel*' python function was used:

t_stat, p_value = ttest_rel (vector_1, vector_2)

where *t_stat* is the computed T-statistic and indicates the magnitude of the difference between the groups relative to the variability, while *p_value* is the probability of observing the data assuming the null hypothesis (no difference) is true. If the p-value is less than the chosen significance level ($\alpha = 0.05$), we reject the null hypothesis and conclude that there is a significant difference between the two groups.

3.10.2 Pearson Correlation

The Pearson correlation coefficient ('*Pearson_coeff*'), often denoted as r, is a statistical measure that quantifies the linear relationship between two continuous variables. It assesses how well the change in one variable can be predicted by the change in another variable. The result of the Pearson correlation coefficient ranges from -1 to 1, and it is interpreted as follows:

- r = 1: perfect positive linear relationship.
- r = -1: perfect negative linear relationship.
- r = 0: No linear relationship. There is no predictable pattern between the variables.
- 0 < r < 1: A positive linear relationship. As one variable increases, the other tends to increase, but not perfectly.
- -1 < r < 0: A negative linear relationship. As one variable increases, the other tends to decrease, but not perfectly.

In all figures, the bisector line was plotted together with the regression line and its equation (to see slope and intercept). Along with the correlation coefficient itself, a p-value is calculated to test the null hypothesis that there is no linear correlation between the two variables. If the p-value is less than significance level ($\alpha = 0.05$), it suggests that the observed correlation is statistically significant. The python function used is:

Pearson_coef, p_value = pearsonr (vector_1, vector_2)

This was performed in several analysis, for example to compare HIPPO results and our results, all the correction factors calculated, and test-retest results.

3.10.3 Bland-Altman Plot

The Bland-Altman plot was used to assess the agreement between the data in several comparison. The structure of this graph is as follows:

- the Y-axis shows the differences between the values

- the X-axis shows the mean of the values

- the middle line represents the mean of the differences between the scores

- the upper and lower lines indicate the confidence interval

Points on the graph that fall within the confidence interval indicate statistically consistent results. If there is no systematic error, the median line should be around zero. On the other hand, if there is an increasing or decreasing pattern, then there is a proportional error. This method is extremely useful to better understand the relationship between our data. For each Person Correlation analysis, the correspondent Bland-Altman Plot will be shown. In addition, a one-sample T-test was carried out, to test whether the mean of the differences between two measurement methods is significantly different from zero:

t_stat, p_value = ttest_1samp (differences, 0)

where *t_stat* is the computed T-statistic. If the *p-value* is higher than the significance level ($\alpha = 0.05$), we fail to reject the null hypothesis, suggesting no significant bias.

CHAPTER 4 – RESULTS

4.1 Segmentation Output

In this first paragraph, the results obtained from the output segmentation are presented (Figure 4.1). All images were acquired with the slices positioned along the plane perpendicular to the long axis of the heart. The region segmented is the left ventricle which has a thickened wall compared to the right ventricle. Besides, myocardial tissue is bright, while blood appears dark since black-blood technique was used in the acquisition phase. Segmentation requires careful observation of the ventricular structure to exclude elements that cannot be classified as myocardial tissue such as inner cavities or heart trabeculae. Generally, in the basal slice, the ventricular wall is easily recognizable, and the mid-ventricular septum is clearly distinguishable. Figure 4.1(A) clearly shows the junction between right ventricle and left ventricle. However, in some MRI images, the middle slice shows a less well-defined septum, leading to increased variability in its selection. The apical part of the ventricle has a smaller diameter compared to the basal and middle sections and in this case the septum could be less recognizable. The start point of the mid-ventricular septum is the point that divides segment 1 from segment 2 in the basal slice, segment 7 from segment 8 in the mid-ventricular slice, and segment 13 from segment 14 in apical slice.

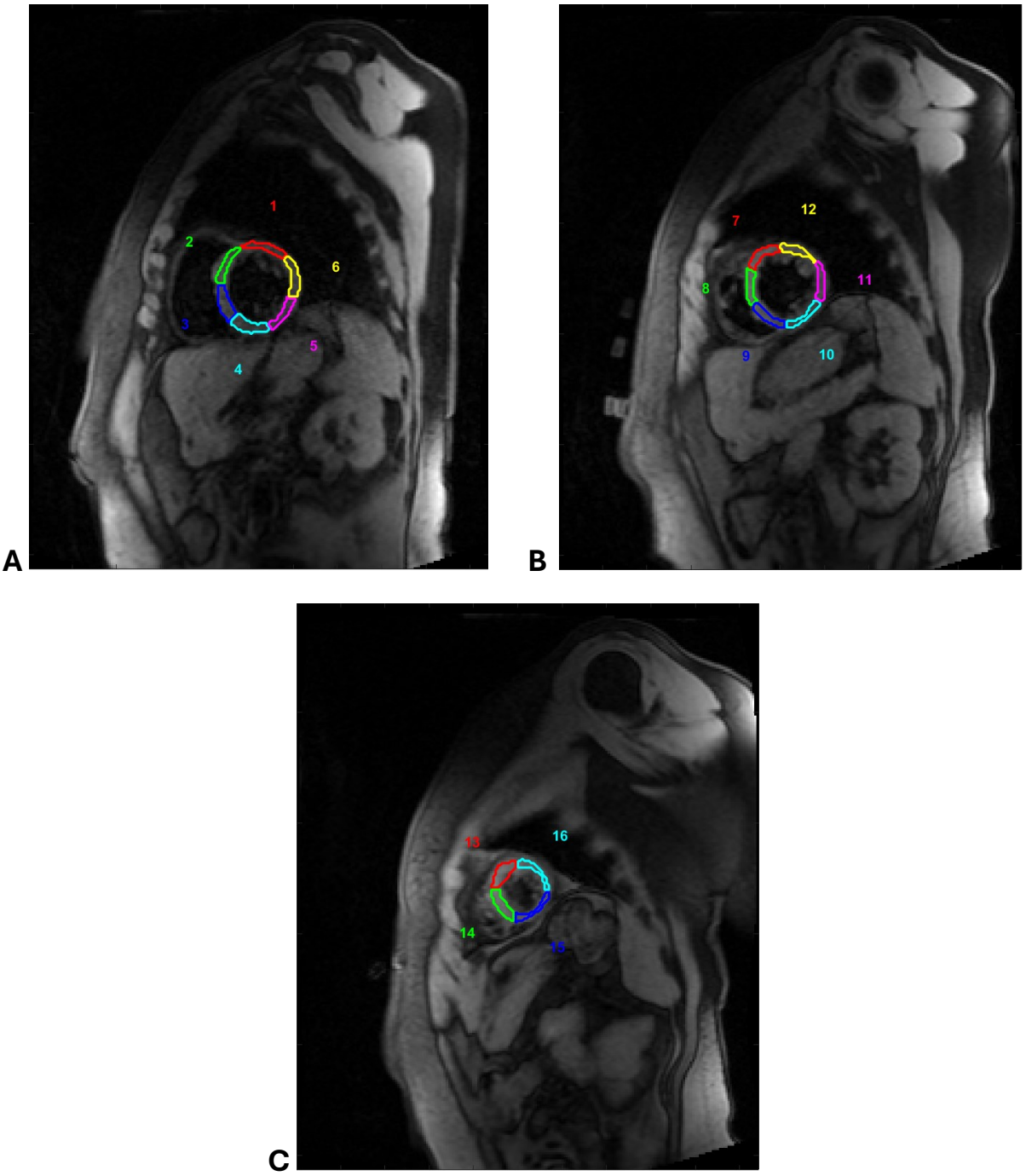

Figure 4.1 Output of myocardial segmentation: 6 segments in basal slice (A), 6 segments in medium slice (B), 4 segments in apical slice (C). Example of a healthy subject from Dataset 1.

4.2 Model results in Healthy Subjects

This section aims to analyse T2* values obtained from the implemented models, in order to show T2* maps obtained from pixel-wise approach, to investigate the effect of smoothing and illustrate T2* global distribution in each segment across all subjects. The coefficient of variation (CV) threshold is set to 1000% to exclude voxels with evident errors that does not belong to an exponential decay. Only the results coming from mono-exponential model, offset model and linear model will be considered. It was decided to exclude the bi-exponential model from further analysis because preliminary findings showed that the T2* map generated by the first component of the model is identical to the one generated by the second component. This suggests that the model cannot distinguish between the two components and effectively reduces to a mono-exponential model. As a result, the bi-exponential model will not be included in the analyses of either healthy subjects or patients.

4.2.1 T2* maps

The pixel-wise approach offers the advantage of generating T2* maps that provide a specific T2* value for each voxel. This allows for a detailed examination of the spatial distribution of T2*. It is particularly useful to analyse the T2* maps generated using all the models described above: S-EXP, LIN, C-EXP models, evaluating also their smoothing effect (Figure 4.2).

A1 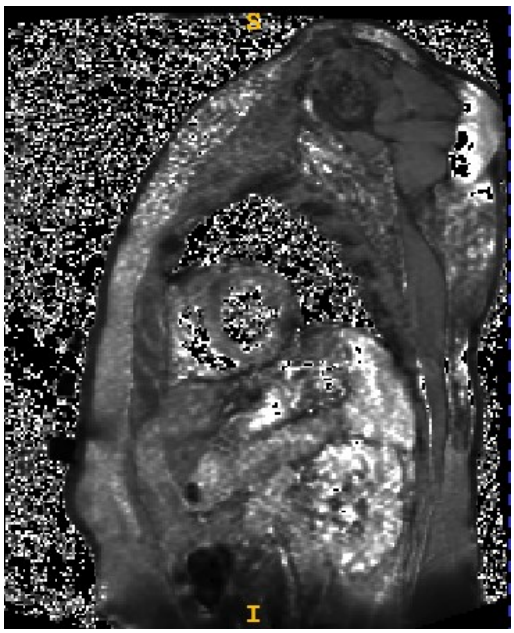

A2 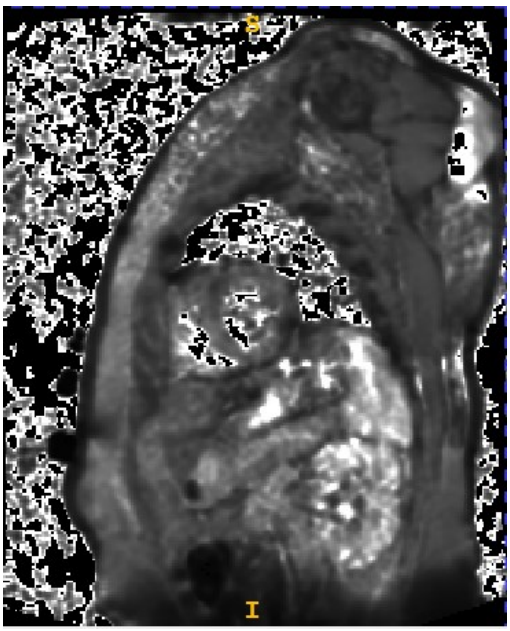

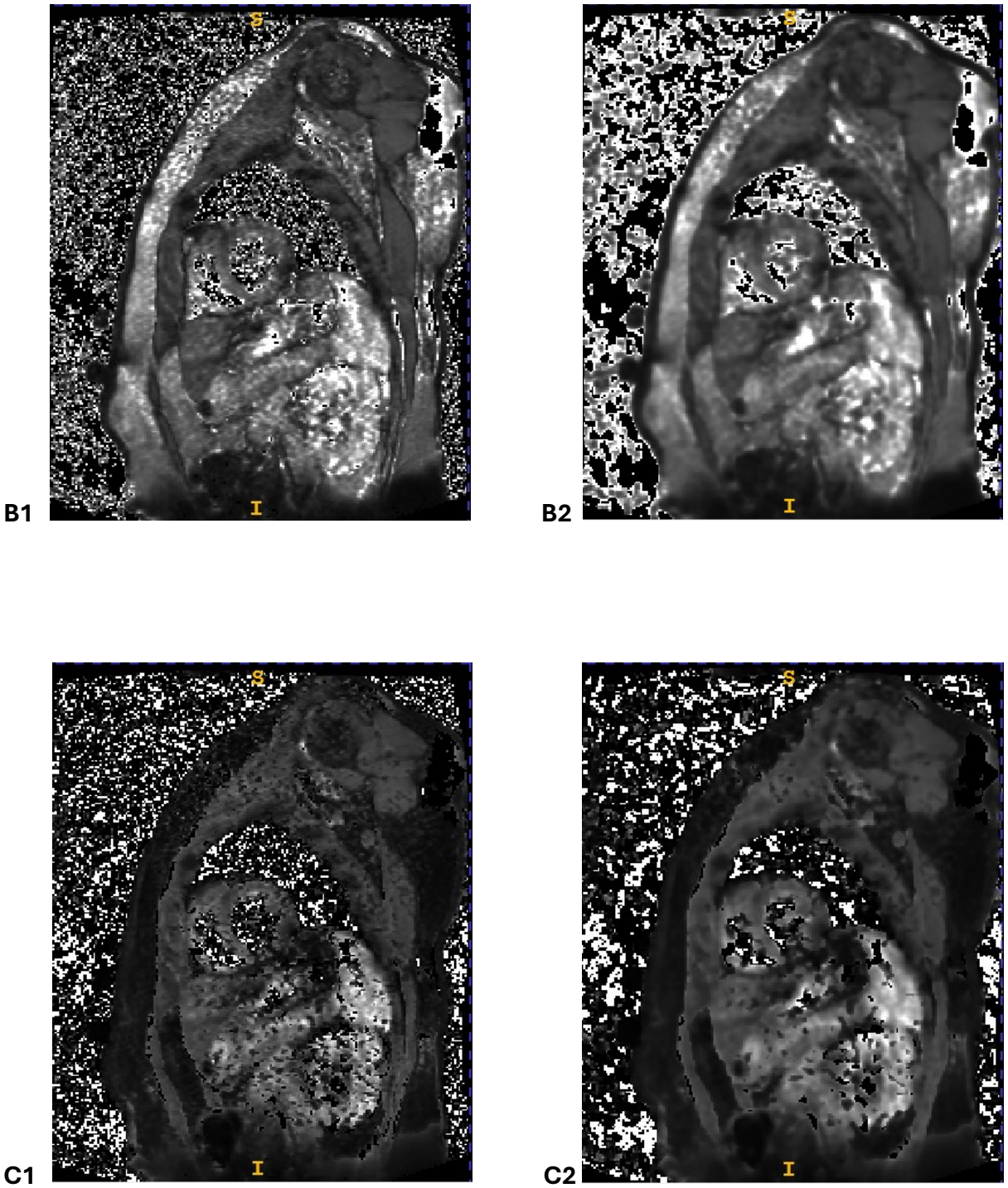

Figure 4.2. Comparison between T2* maps obtained from models without smoothing effect (first column) and with smoothing effect (second column). (A) Example of a T2* map obtained from S-EXP; (B) Example of a T2* map obtained from LIN; (C) Example of a T2* map obtained from C-EXP. This example refers to the mid-ventricular slice. The range of visualization is set to 0-100 ms (ITK-SNAP Software)

4.2.2 Smoothing evaluation

This analysis aims to perform a side-by-side comparison between mean T2* values, calculated in each segment by averaging T2* across all subjects, obtained from the S-EXP, LIN and C-EXP models in both their smoothed and unsmoothed versions. This approach highlights any significant differences in the mean T2* estimation for each segment across all subjects (the '*' symbol aims to indicate in which segment the difference is significative). As shown in Figure 4.3 (A-B-C) smoothing effect does not introduce consistent differences across all the sixteen segments. All results in this section were generated using a pixel-wise approach, with a coefficient of variation (CV) threshold set to 1000%, and not considering T2* estimates higher than 200 ms, considered as not reliable and not physiologically plausible.

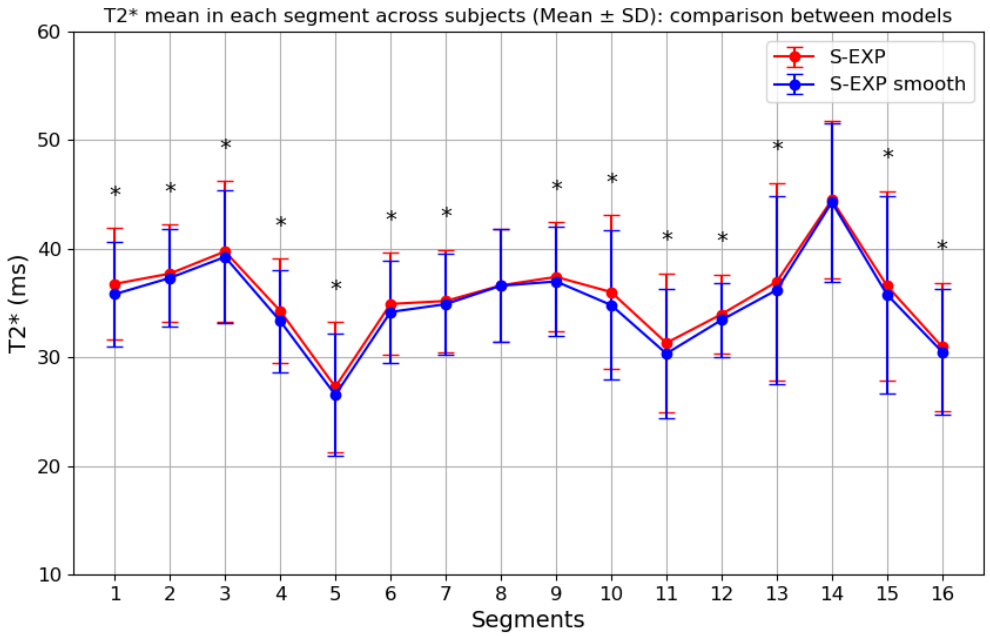

A

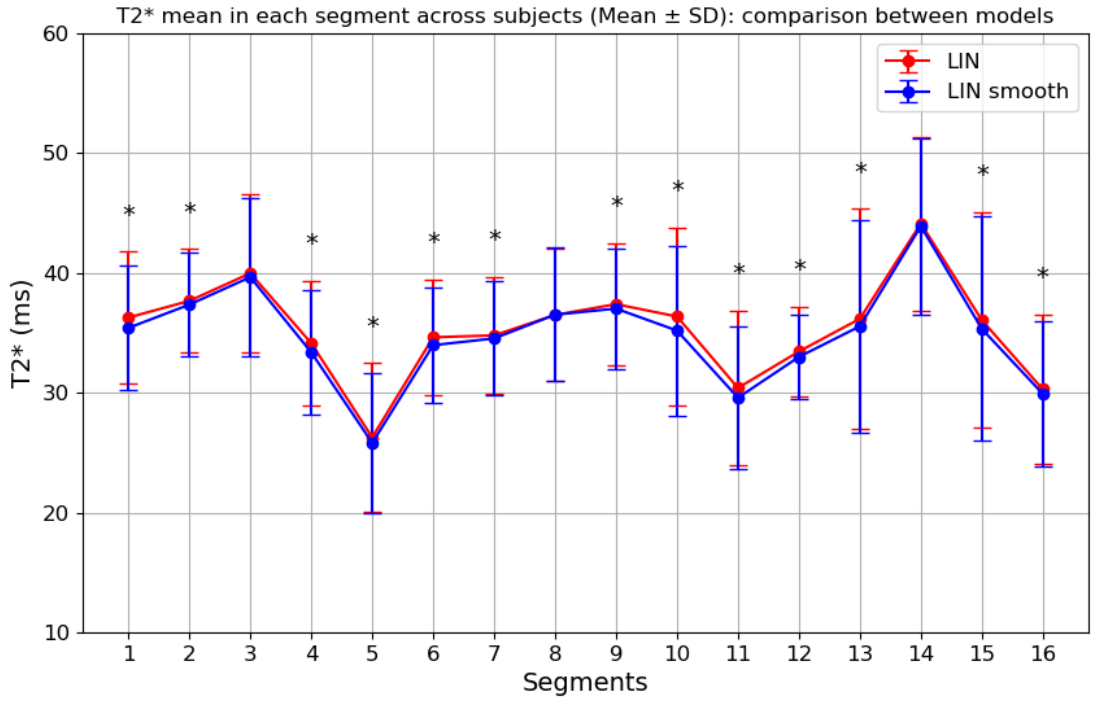

B

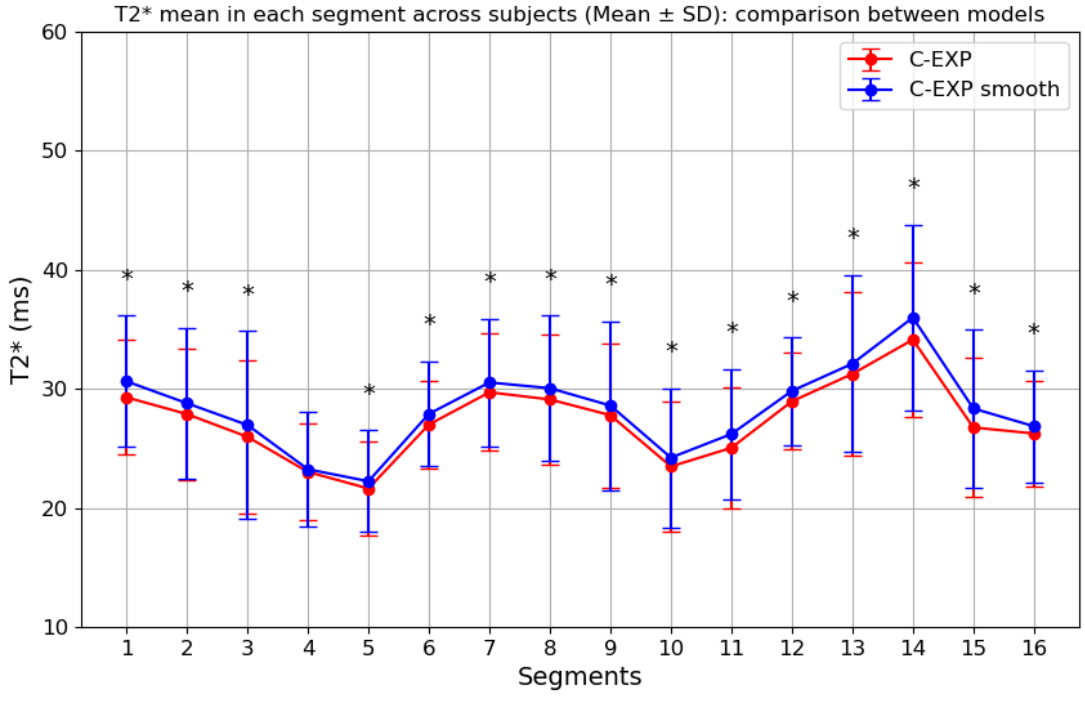

C

Figure 4.3. T2* mean values obtained by applying smoothing and non-smoothing technique in S-EXP (A), LIN (B), C-EXP (C) models considering all healthy subjects.

From these figures we can also observe that T2* means obtained from LIN model and S-EXP model led to similar T2* estimations, however C-EXP model underestimates T2*. To compare the overall trend in these models, the results of T2* global estimates (averaging T2* values across healthy subjects) are reported here. The three superimposed curves are shown in the Figure 4.4. This plot refers to model results without smoothing.

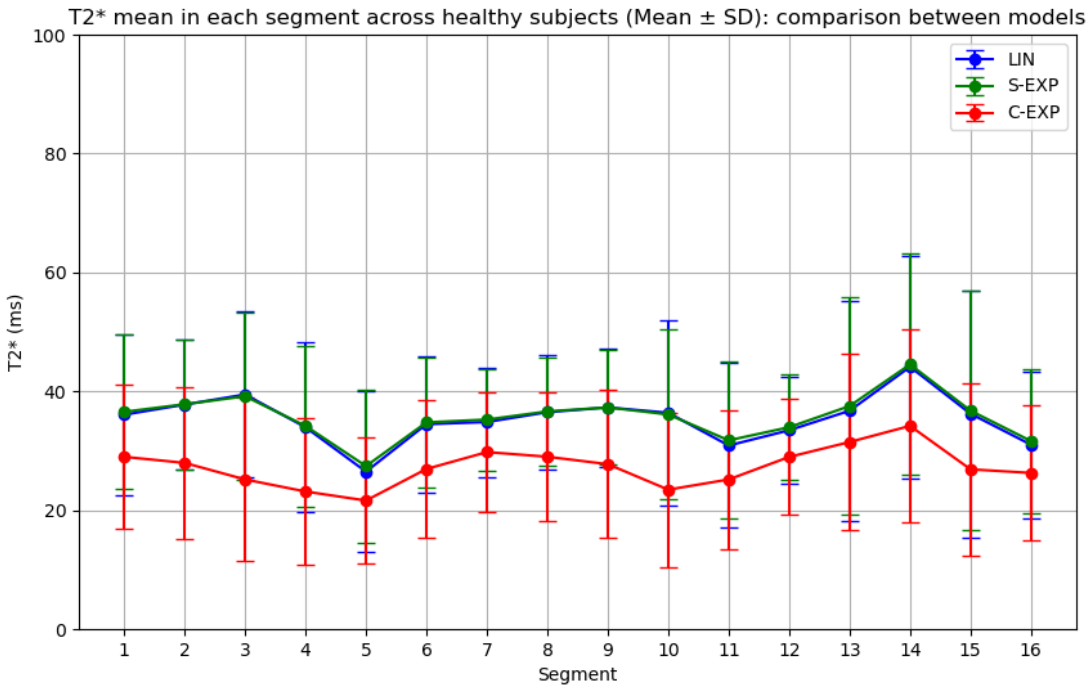

Figure 4.4. T2* mean and standard deviation obtained in each segment across all healthy subjects with LIN, S-EXP, C-EXP models (without smoothing)

4.2.3 T2* Distribution

The effect of the smoothing is discussed in the next chapter, however we anticipate that since the estimated values using or not using smoothing are comparable and also the trend across the segments is not greatly influenced by the smoothing procedure, from this point onwards only non-smoothing version will be considered. We can now evaluate which is the variability in T2* values obtained with S-EXP, LIN, C-EXP models (Figure 4.5). It is worth noting that the variance across segments is similar between S-EXP and LIN, however for C-EXP model the variance in the estimates is larger. The three models considered however produce a similar trend for the myocardial segments.

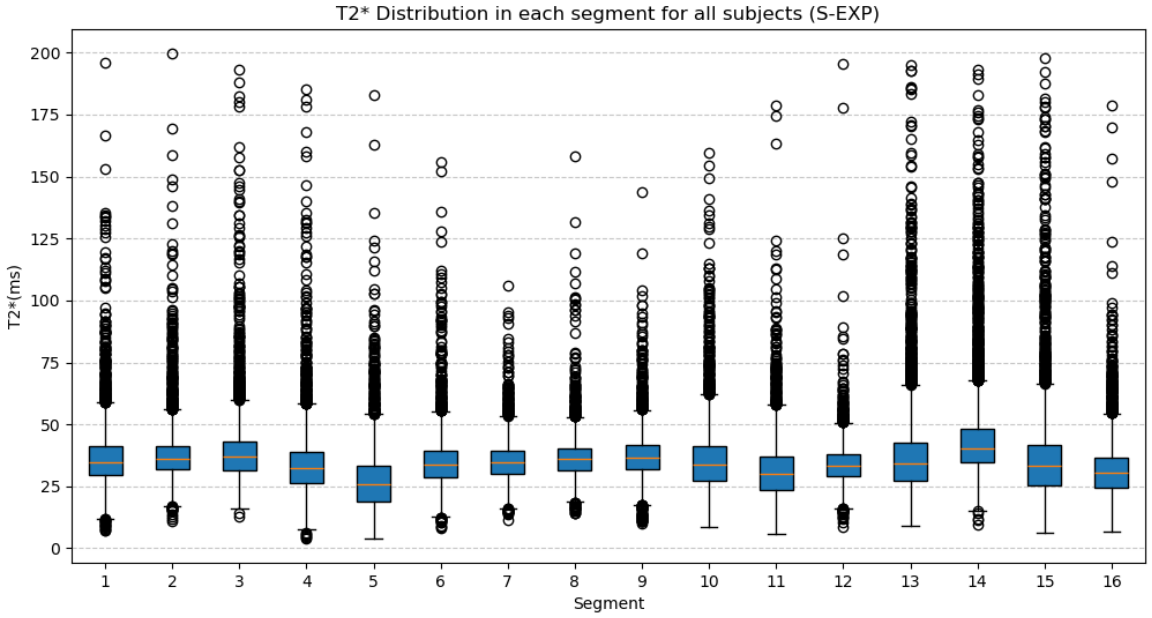
T2* Distribution in each segment for all subjects (S-EXP)
T2*(ms)
Segment

A

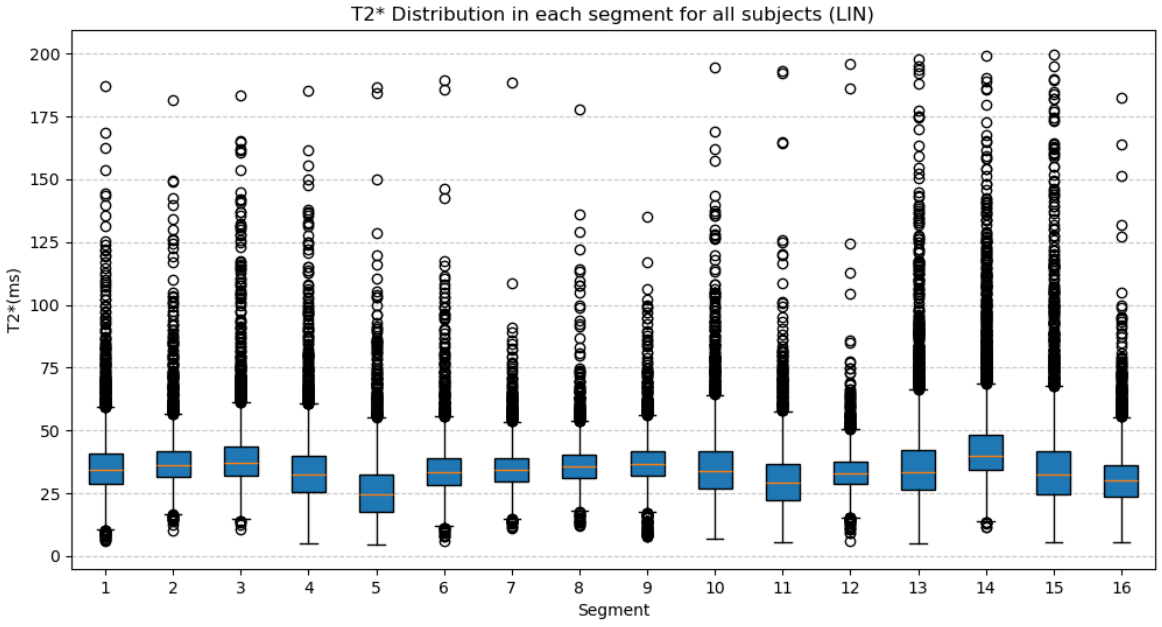
T2* Distribution in each segment for all subjects (LIN)
T2*(ms)
Segment

B

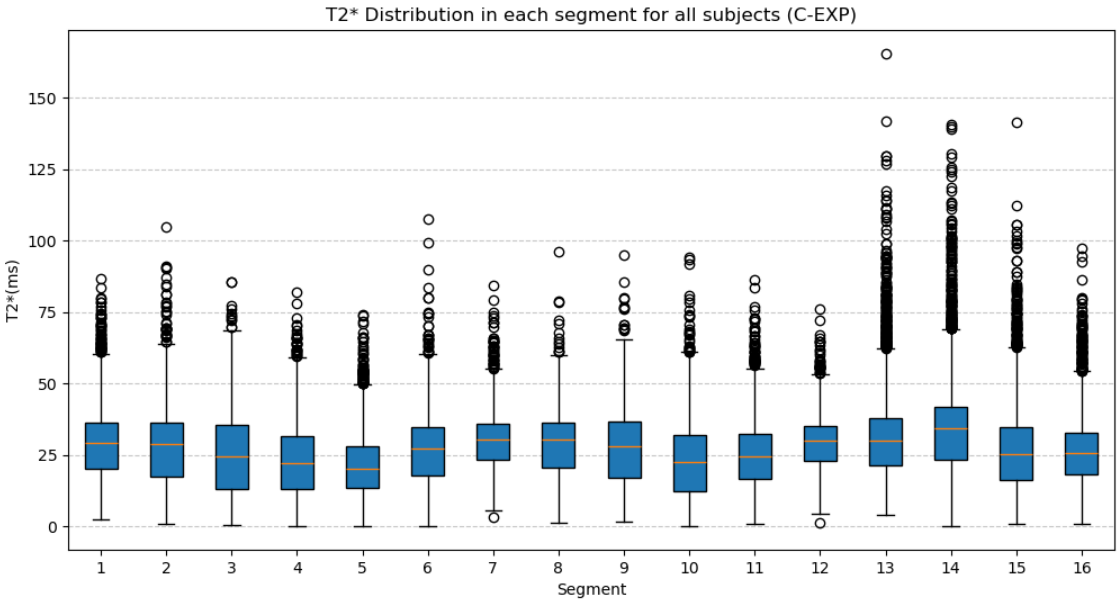

C

Figure 4.5. Boxplot for S-EXP (A), LIN (B), C-EXP (C), considering all healthy subjects.

4.3 Model results in Patients

In this section the same images and plots that were reported for healthy subjects are shown, in to see if the results obtained in patients are different or lead to similar conclusions.

4.3.1 T2* maps

This first section contains T2* maps obtained coming from the mono-exponential model, the offset model, and the linear model. In each model we evaluated also the smoothing effect (Figure 4.6).

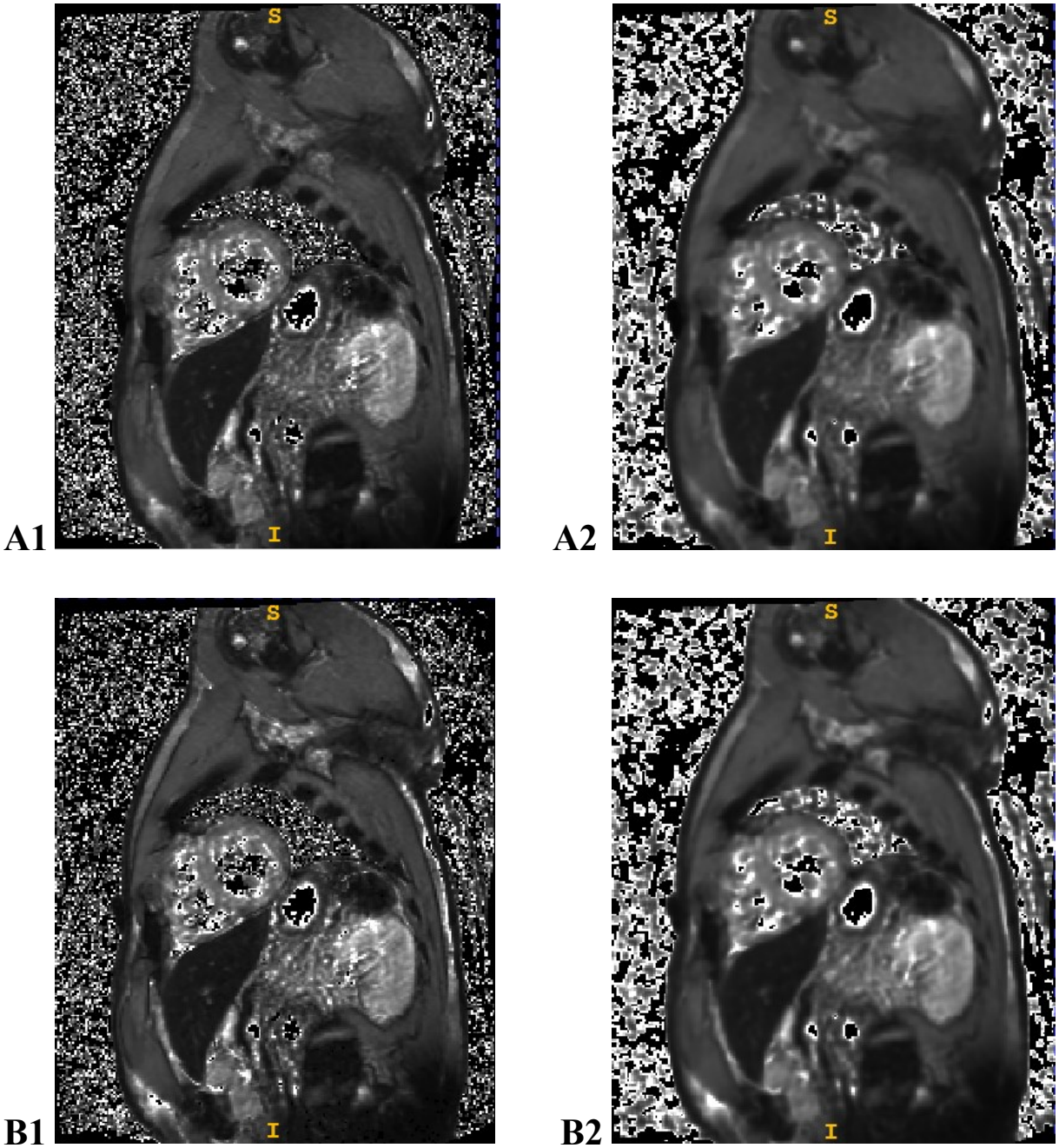

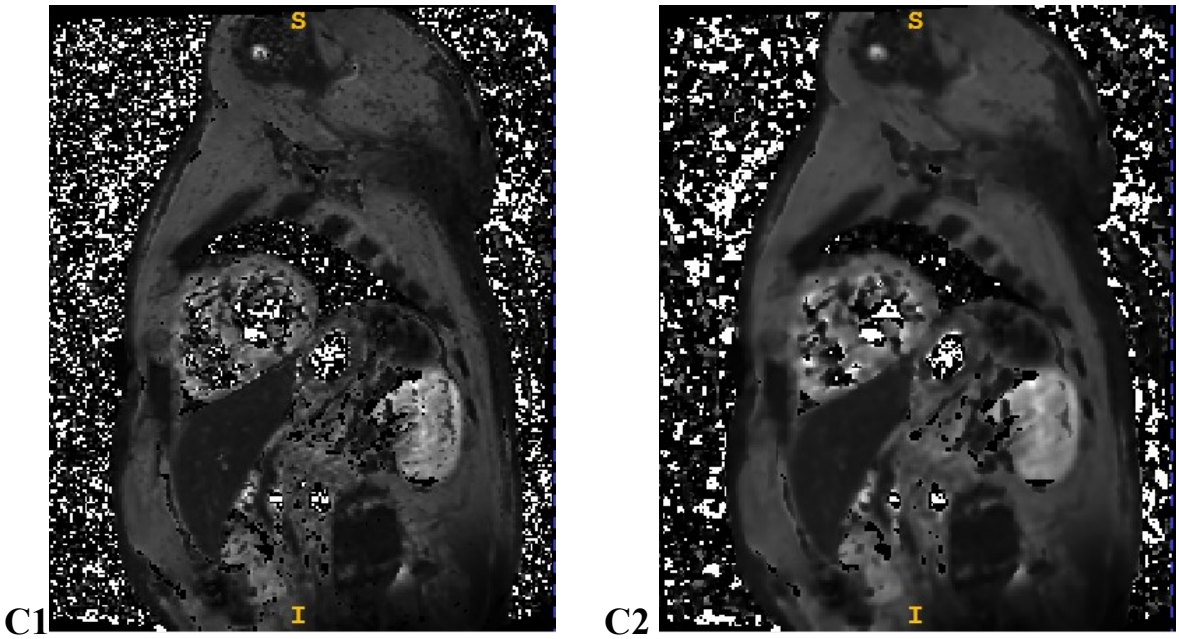

Figure 4.6. Comparison between T2* maps obtained from models without smoothing effect (first column) and with smoothing effect (second column). (A) T2* map obtained from S-EXP; (B) T2* map obtained from LIN; (C) T2* map obtained from C-EXP. This example refers to the mid-ventricular slice of a patient. The range of visualization is set to 0-100 ms (ITK-SNAP Software)

4.3.2 Smoothing Evaluation

The same considerations explained in paragraph 4.2.2 remain valid also in patient analysis. So, we evaluated produced by the smoothing effect in each model (Figure 4.7).

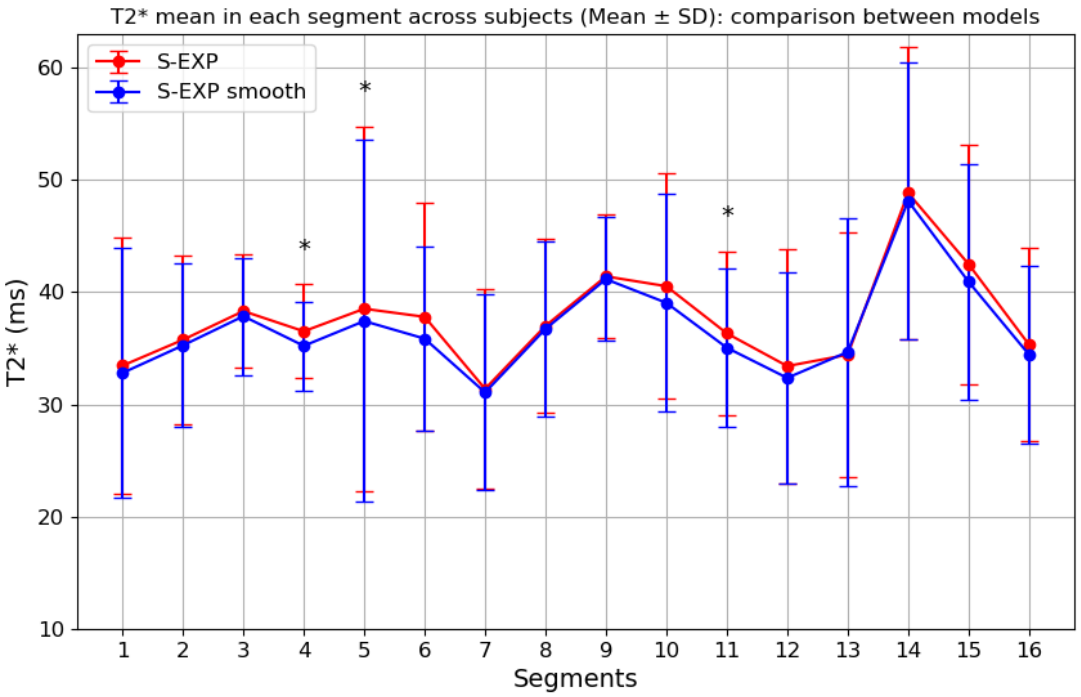

A

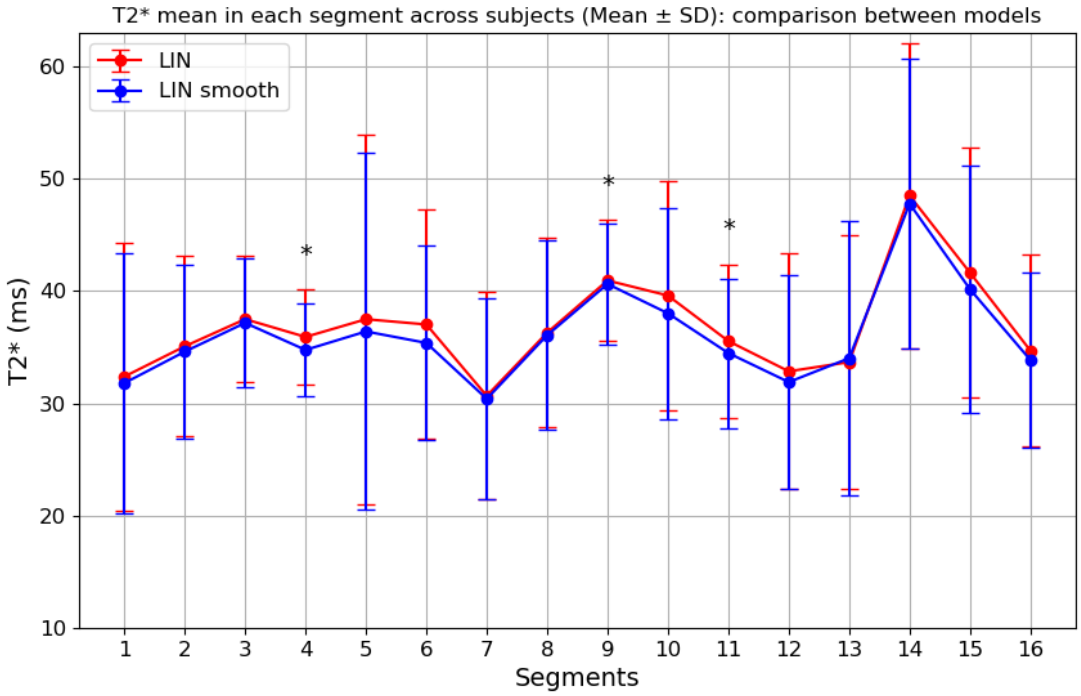

B

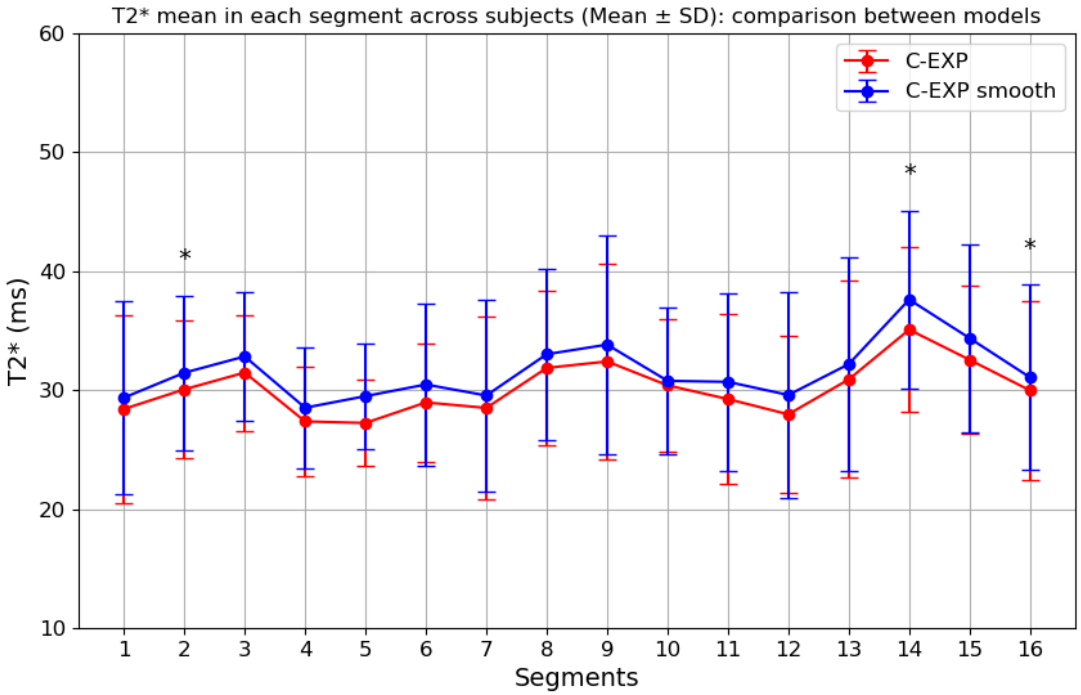

C

Figure 4.7. T2* mean values obtained by applying smoothing and non-smoothing technique in S-EXP (A), LIN (B), C-EXP (C) models considering all patients

From these figures we can also observe that T2* means obtained from LIN model and S-EXP model led to similar T2* estimations, however C-EXP model underestimates T2*. To compare the overall trend in these models, the results of T2* global estimates (averaging T2* values across subjects) are reported here. The three superimposed curves are shown in the Figure 4.8. This plot refers to model results without smoothing.

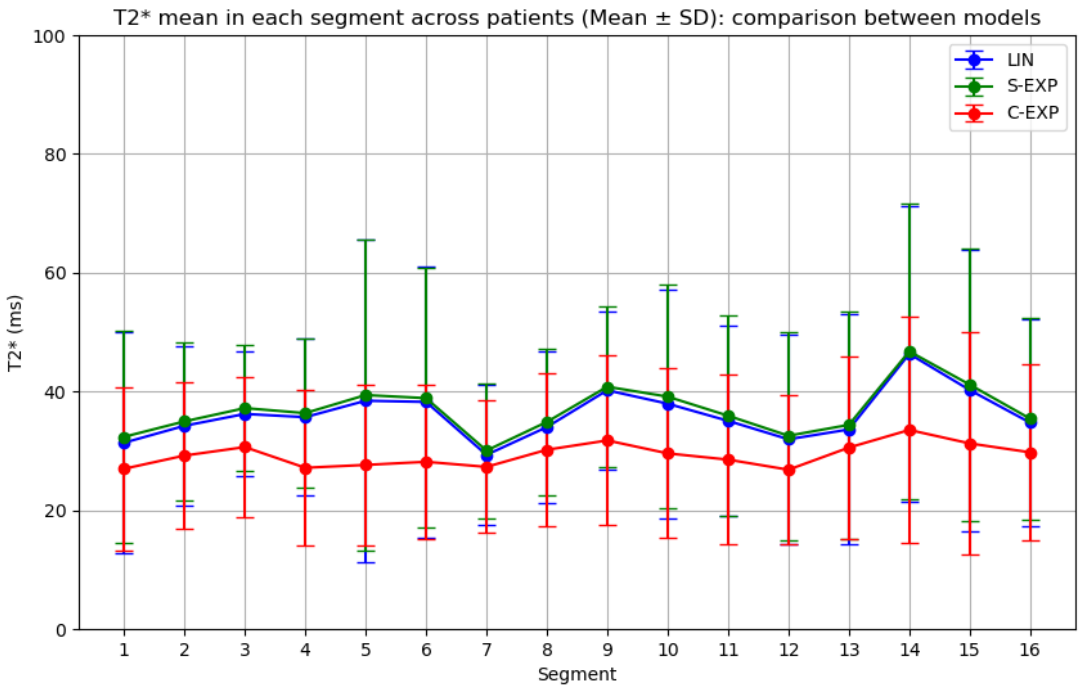

Figure 4.8. T2* mean and standard deviation obtained in each segment across all patients with LIN, S-EXP, C-EXP models (without smoothing)

4.3.3 T2* Distribution

We can now evaluate which is the variability in T2* values obtained with S-EXP, LIN, C-EXP models (Figure 4.9). Since the results are very similar (like in healthy subjects), only non-smoothing version will be considered. As for the Dataset 1, when analysing the variance across segments it is worth noting that the variance is larger for T2* values obtained with C-EXP compared to S-EXP and LIN models. The trend is similar, however the underestimation in T2* values is evident.

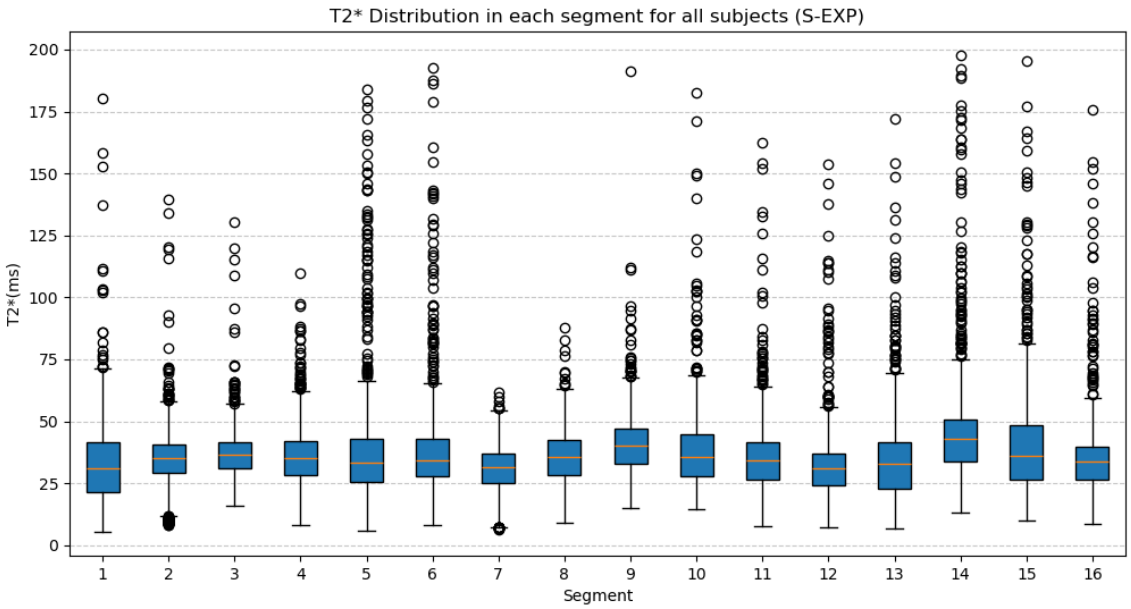
T2* Distribution in each segment for all subjects (S-EXP)
T2*(ms)
Segment

A

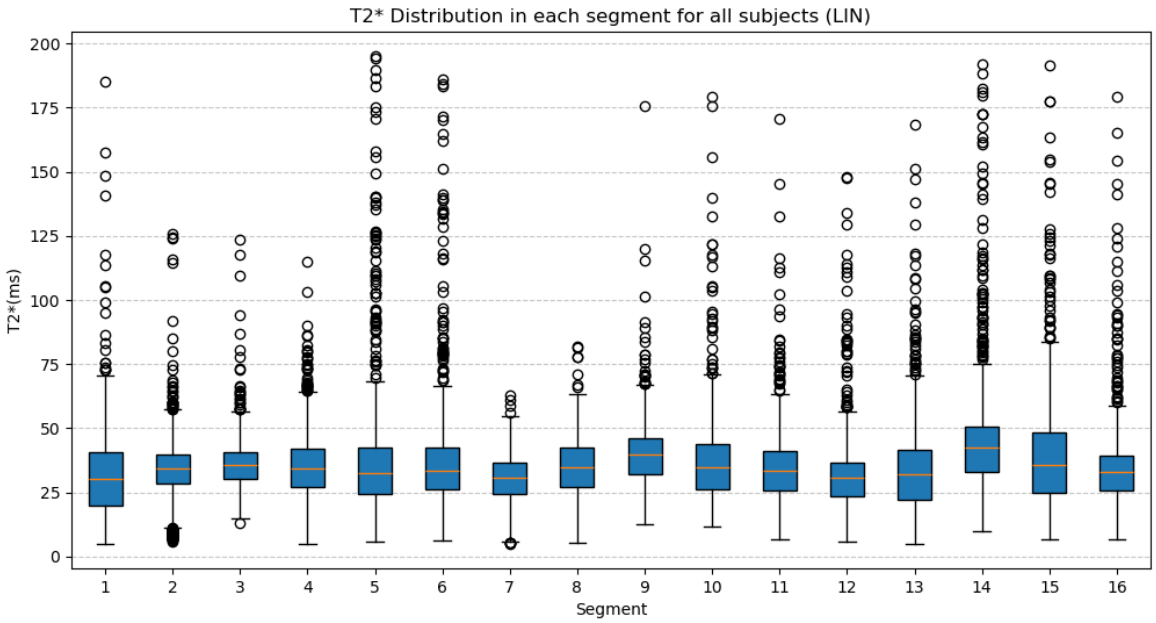
T2* Distribution in each segment for all subjects (LIN)
T2*(ms)
Segment

B

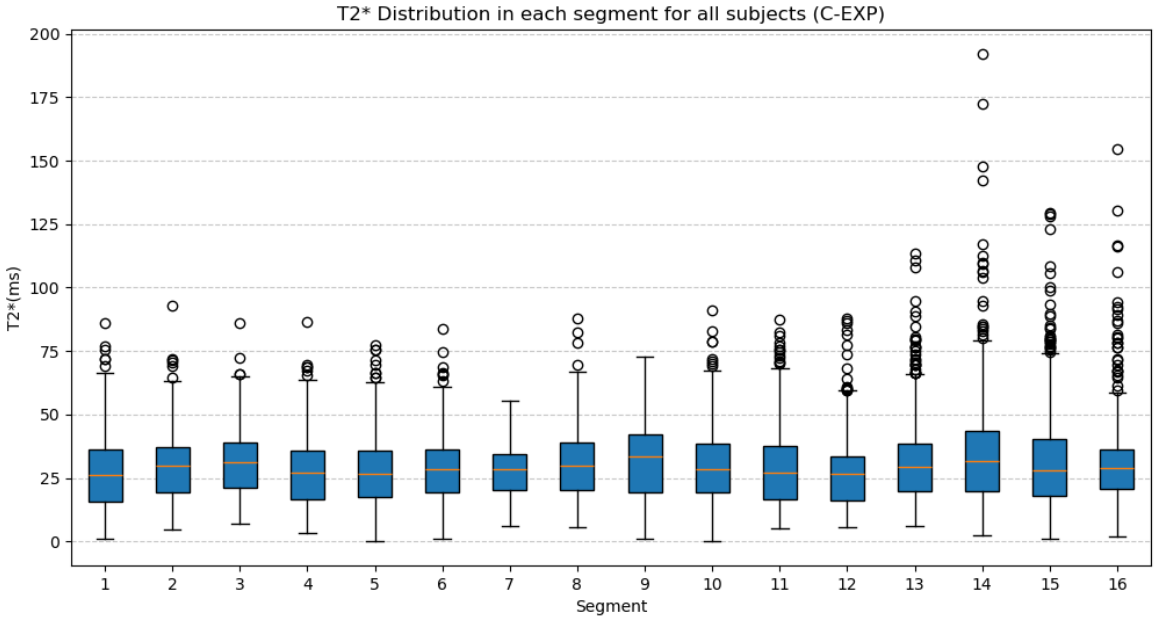

C

Figure 4.9. Boxplot for S-EXP (A), LIN (B), C-EXP (C), considering all patients.

4.4 Best model selection

To determine the best model for estimating T2* in myocardial tissue, the *Bayesian Information Criterion* (BIC) was employed. In the following subsections, we analyse the percentage of voxels in which one model outperforms another, considering all subjects. This analysis was conducted separately for each segment to identify potential variations in the distribution of the preferred model. The BIC comparison was applied to both pixel-wise models (with and without smoothing) and ROI-based models. The first section focuses on healthy subjects, while the second section examines patients. In both cases, a CV threshold of 1000% was considered.

4.4.1 Healthy Subjects

Figure 4.10, 4.11, 4.12 show the results obtained by the application of *Bayesian Information Criterion* in healthy subjects.

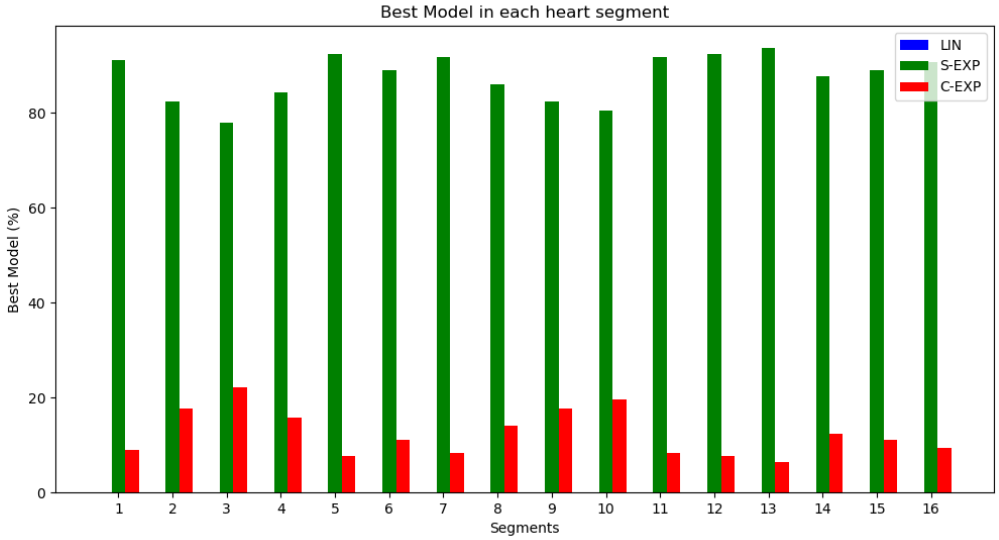

Figure 4.10. BIC results in S-EXP, LIN, C-EXP models with pixel-wise approach (without smoothing effect): each column shows the percentage of voxels where that model performs better.

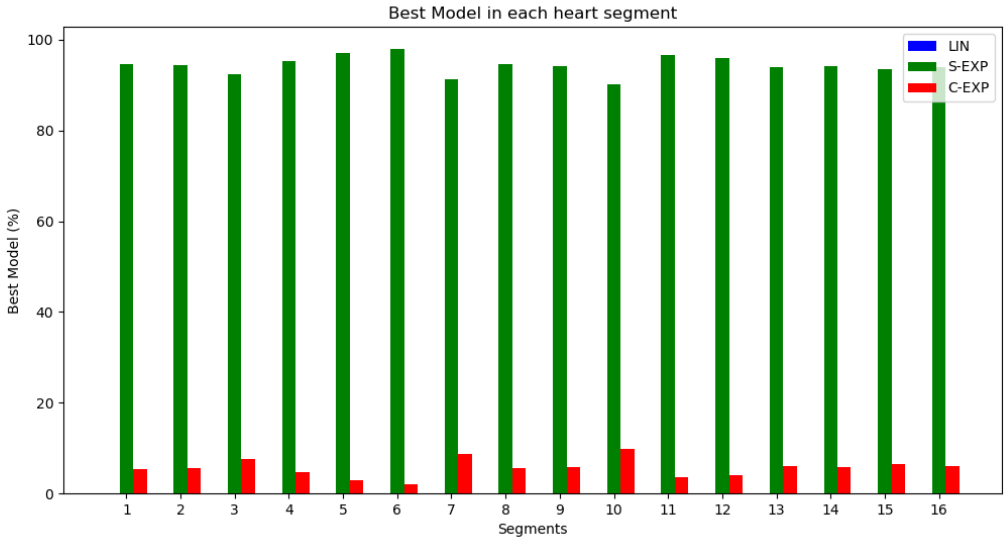

Figure 4.11. BIC results in S-EXP, LIN, C-EXP models with pixel-wise approach (with smoothing effect): each column shows the percentage of voxels where that model performs better.

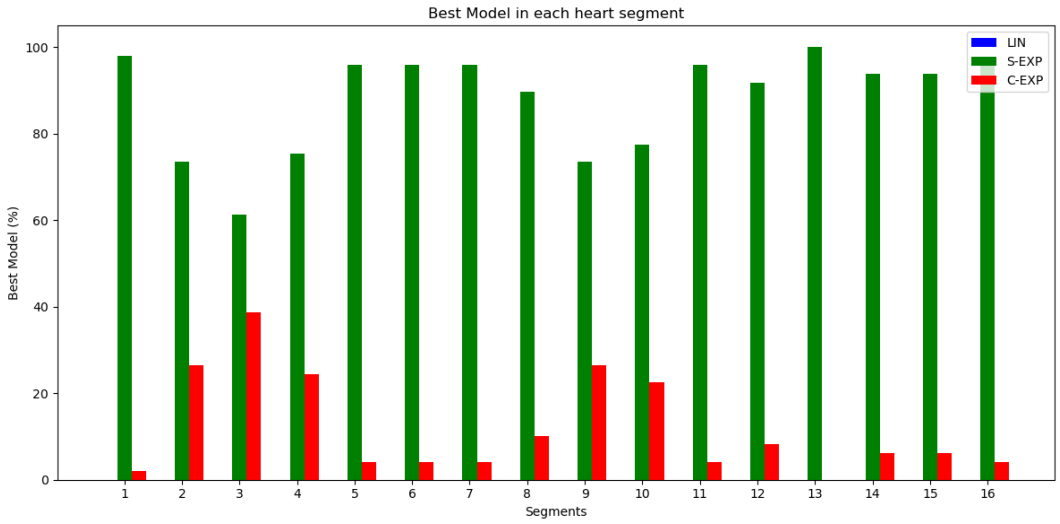

Figure 4.12. BIC results in S-EXP, LIN, C-EXP models with ROI-based approach: each column shows the percentage of segments where that model performs better.

The S-EXP model prevalence is clearly visible in these histograms. However, to identify the specific subjects contributing voxels where the C-EXP model performs better, the graph in Figure 4.13 was created (related only to Figure 4.10, since the pixel-wise approach allows to consider each T2* value). In this matrix, the x-axis represents the subjects, while the y-axis represents the segments. Focusing only on voxels where the mono-exponential model with constant provides the lowest BIC index, the graph shows the percentage of these voxels from each subject. The colour intensity reflects the percentage, as indicated by the accompanying colour bar.

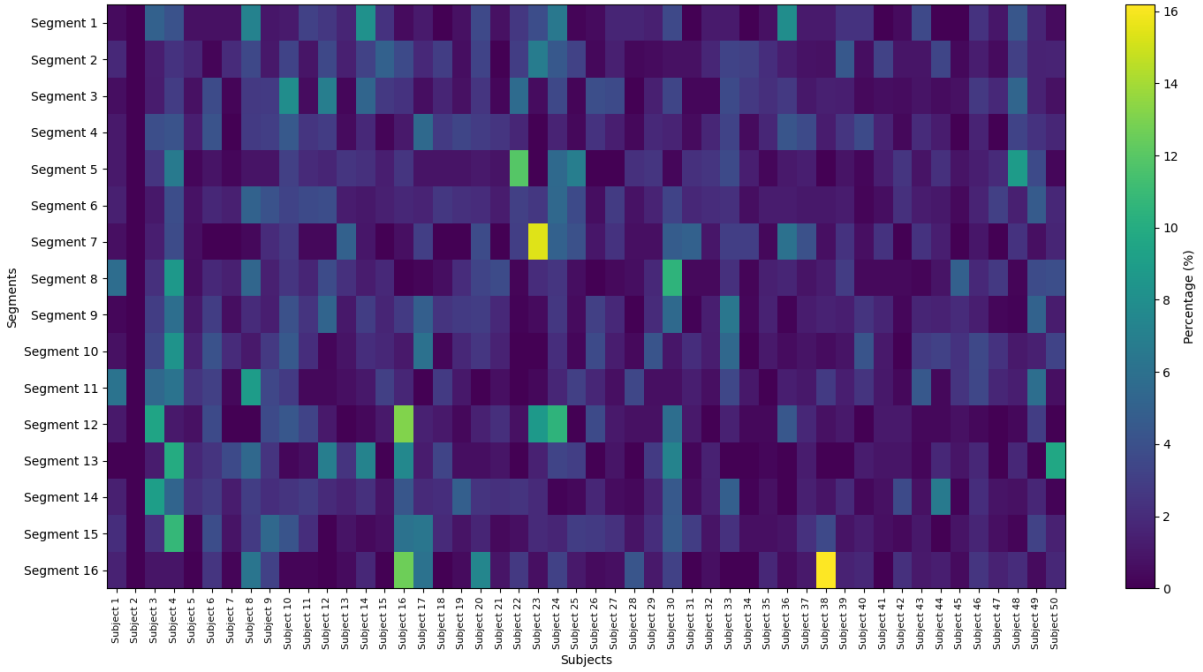

Figure 4.13. Relationship between segments and subjects in voxel where C-EXP performs better: in each segment is shown the percentage of voxels where C-EXP performs better distinguished across all subjects

The highest percentage are in correspondence of segment 7 of subject 23, and segment 16 of subject 38. To understand what happens in these segments, two histograms with all T2* mean values in each segment of subject 23 and subject 38 were plotted (Figure 4.14). Blue colour shows T2* mean values in each segment obtained with LIN model, orange colour shows T2* mean-values in each segment obtained with S-EXP model, and green colour shows T2* mean values in each segment obtained with C-EXP model. Each of these histograms can be interpreted as a bull's eye result, since it is usually used to represent mean values in each segment.

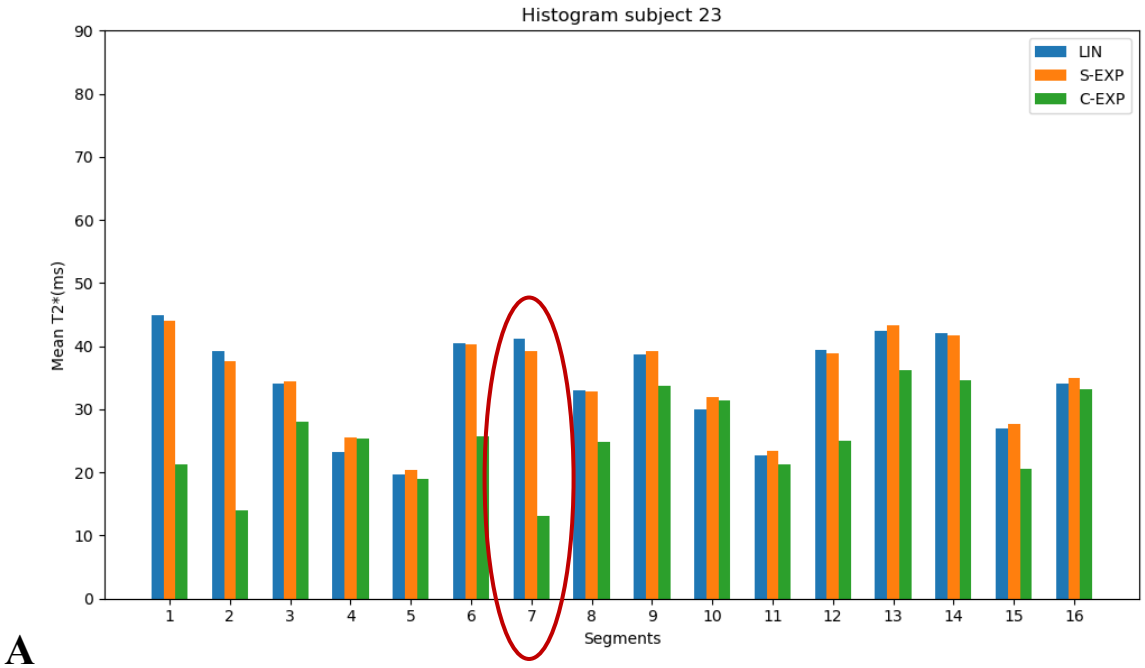

A

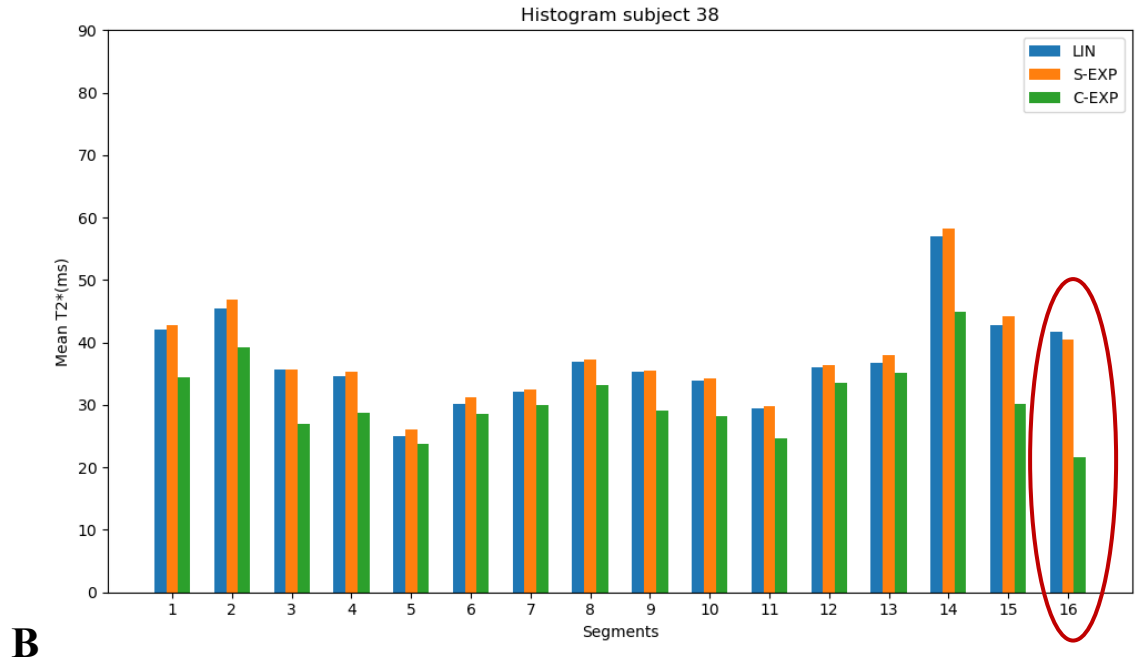

B

Figure 4.14. (A) T2* mean values of subjects 23. (B) T2* mean values of subject 38, with S-EXP, LIN, C-EXP models

4.4.2 Patients

Figure 4.15, 4.16, 4.17 show the results obtained by the application of *Bayesian Information Criterion* in healthy subjects.

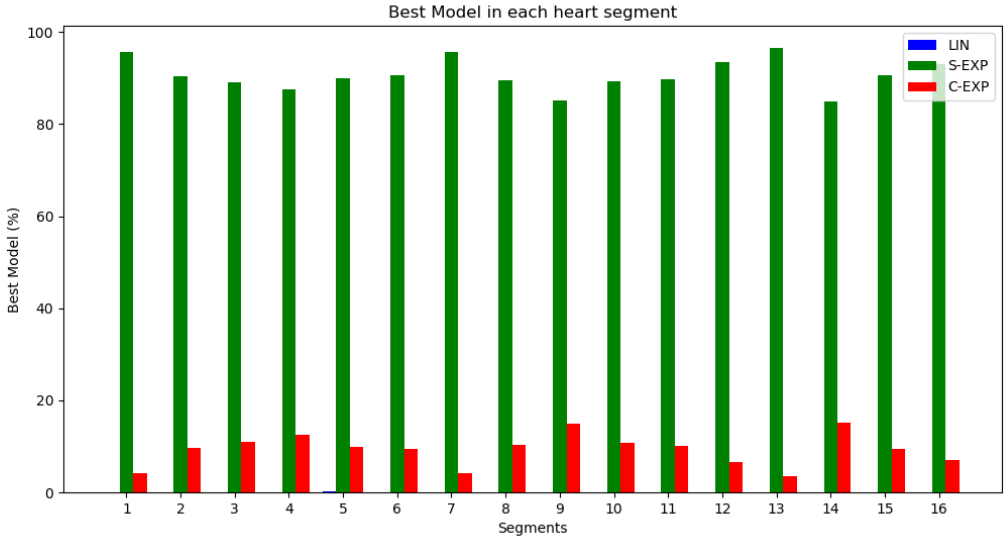

Figure 4.15. BIC results in S-EXP, LIN, C-EXP models with pixel-wise approach (without smoothing effect): each column shows the percentage of voxels where that model performs better.

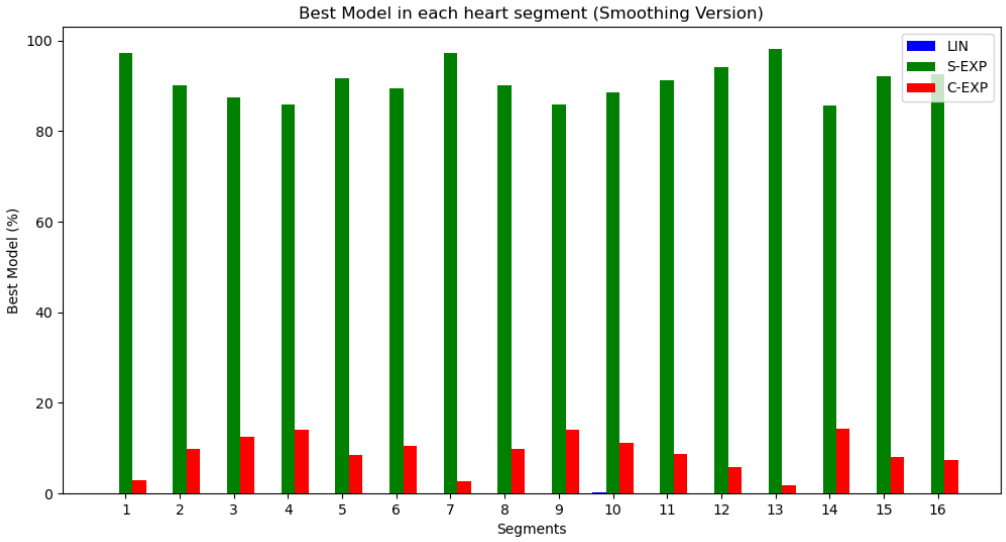

Figure 4.16. BIC results in S-EXP, LIN, C-EXP models with pixel-wise approach (with smoothing effect): each column shows the percentage of voxels where that model performs better.

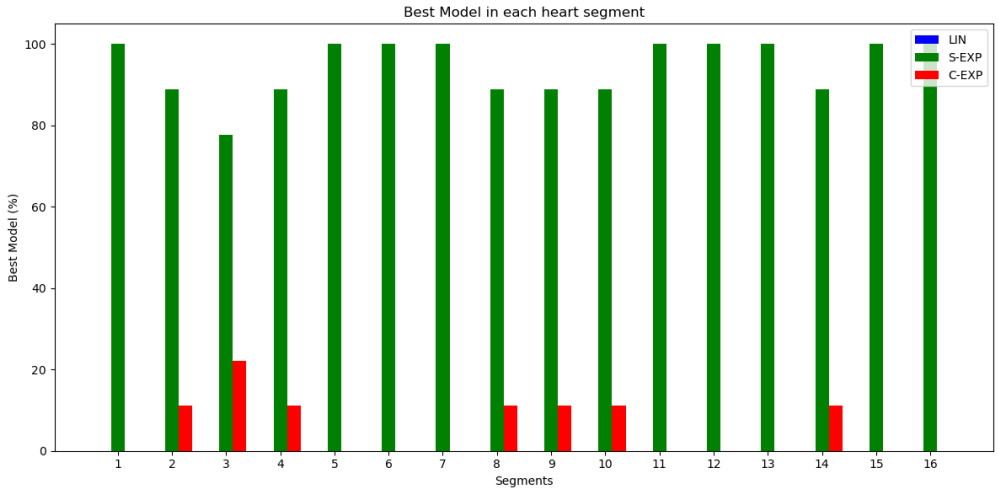

Figure 4.17. BIC results in S-EXP, LIN, C-EXP models with ROI-based approach: each column shows the percentage of segments where that model performs better.

Similarly to the healthy subjects, the same matrix (Figure 4.18) was made to understand the distribution of voxels where C-EXP predominates. Again, it must be interpreted in relation to Histogram 4.15.

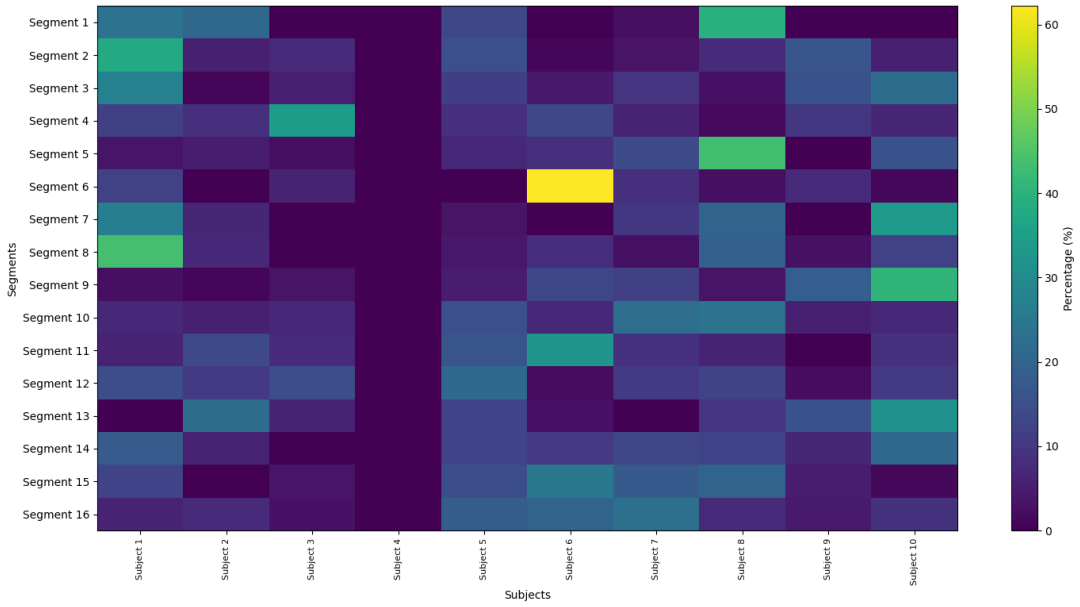

Figure 4.18. Relationship between segments and subjects in voxel where C-EXP performs better: in each segment is shown the percentage of voxels where C-EXP performs better distinguished across all subjects

The highest percentage are in correspondence of segment 6 of subject 6. To understand what happens in this segment, a histogram with all T2* mean values in each segment was plot (Figure 4.19).

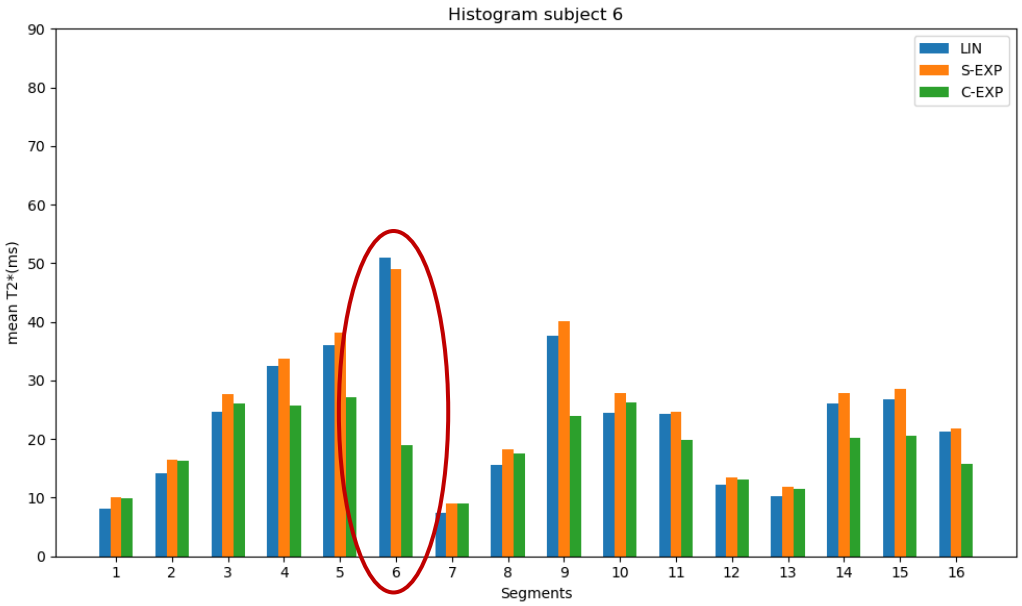

Figure 4.19. T2* mean values of patient number 6 obtained with S-EXP, LIN, C-EXP models

4.5 CV Threshold

Coefficient of variation parameter helps to understand where T2* estimates are reliable. Since the manual nature of the segmentation process makes it challenging to accurately trace the endocardial and epicardial contours, some voxels within the selected ROI lack an MR signal. As a result, no-signal voxels are inadvertently included (see Figure 4.20), and do not exhibit exponential decay.

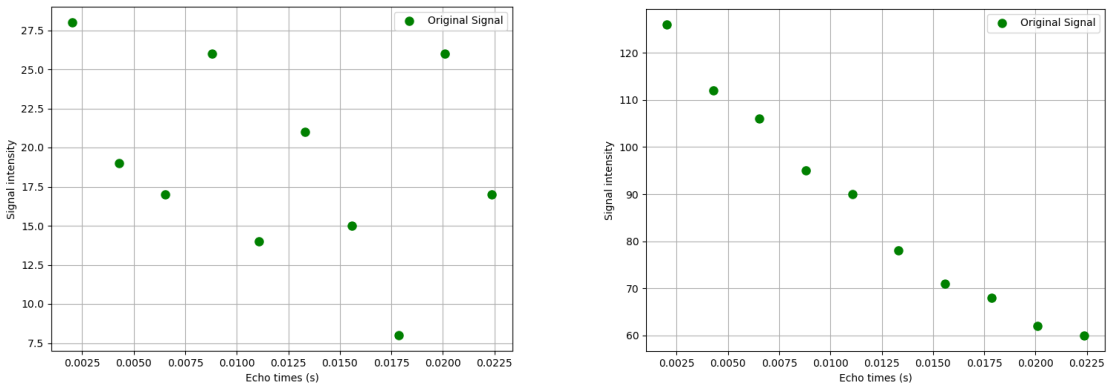

Figure 4.20. (A) No-signal voxel. (B) MR-signal in a myocardial voxel.

Initial CV threshold was set to 1000% only to exclude voxels with a glaring not exponential decay, but the number of outliers is too high with this approach, and this influences T2* mean estimation. Therefore, it was decided to decrease this value. In literature, usually a CV threshold equal to 10 is used to include only reliable voxels [56]. Setting this new threshold, the number of outliers decreases. In addition, we will present the percentage of discarded voxels by this stringent threshold, in each segment using a pixel-wise approach for all models (S-EXP, LIN, C-EXP), across both healthy subjects and patients. Furthermore, the percentage of discarded segments in the ROI-based approach will also be shown for both datasets.

4.5.1 Healthy Subjects

In the following histograms (Figure 21), the percentage of discarded voxels in each segment considering all healthy subjects are shown for each of the implemented models. The same analysis was performed with ROI-based approach models, and the percentage of discarded segments is shown Figure 22.

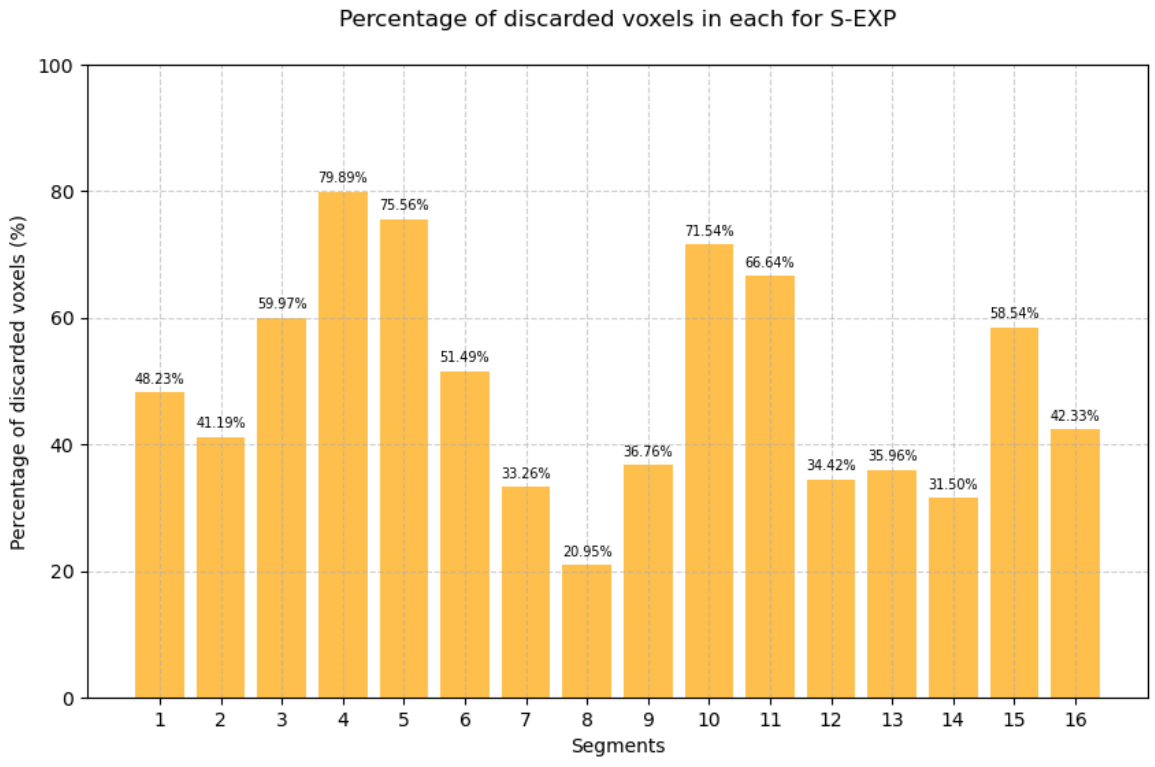

A

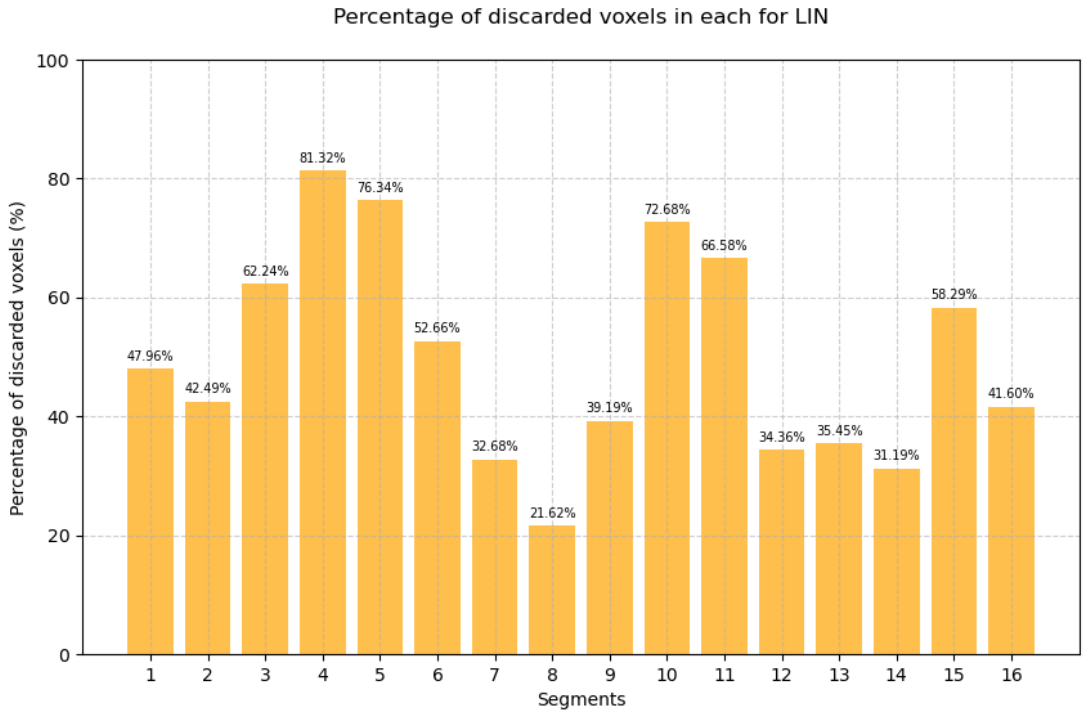

B

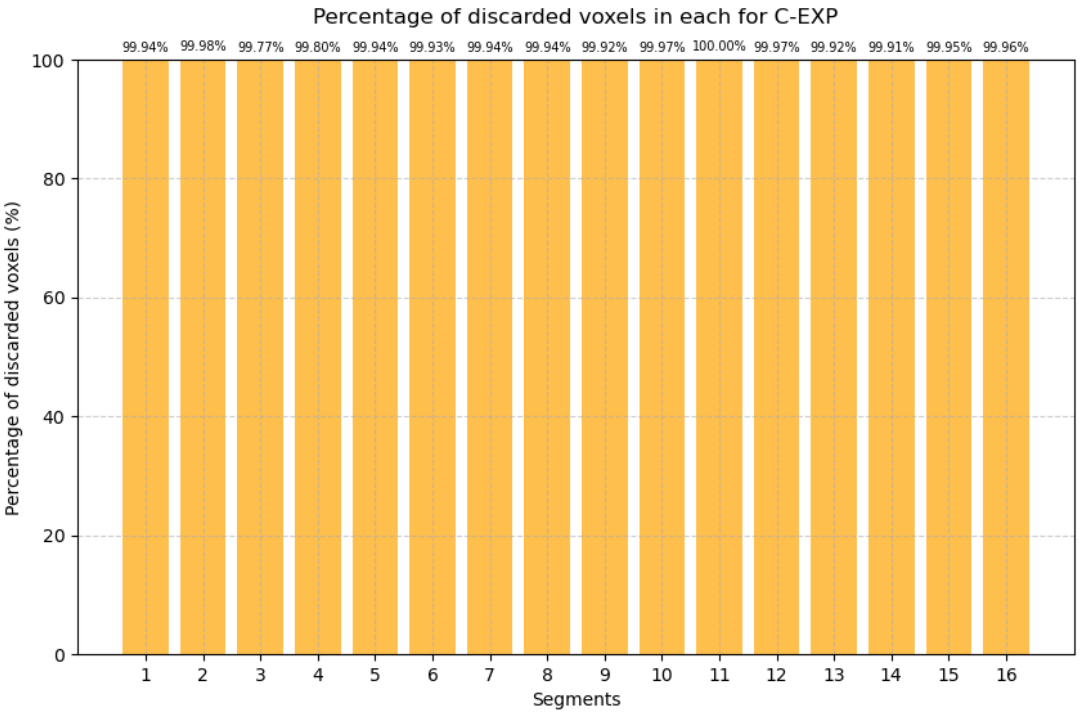

C

Figure 4.21. Percentage of deleted voxels across all healthy subjects by setting a cv threshold equal to 10% in S-EXP (A), LIN (B), C-EXP (C) models (pixel-wise approach).

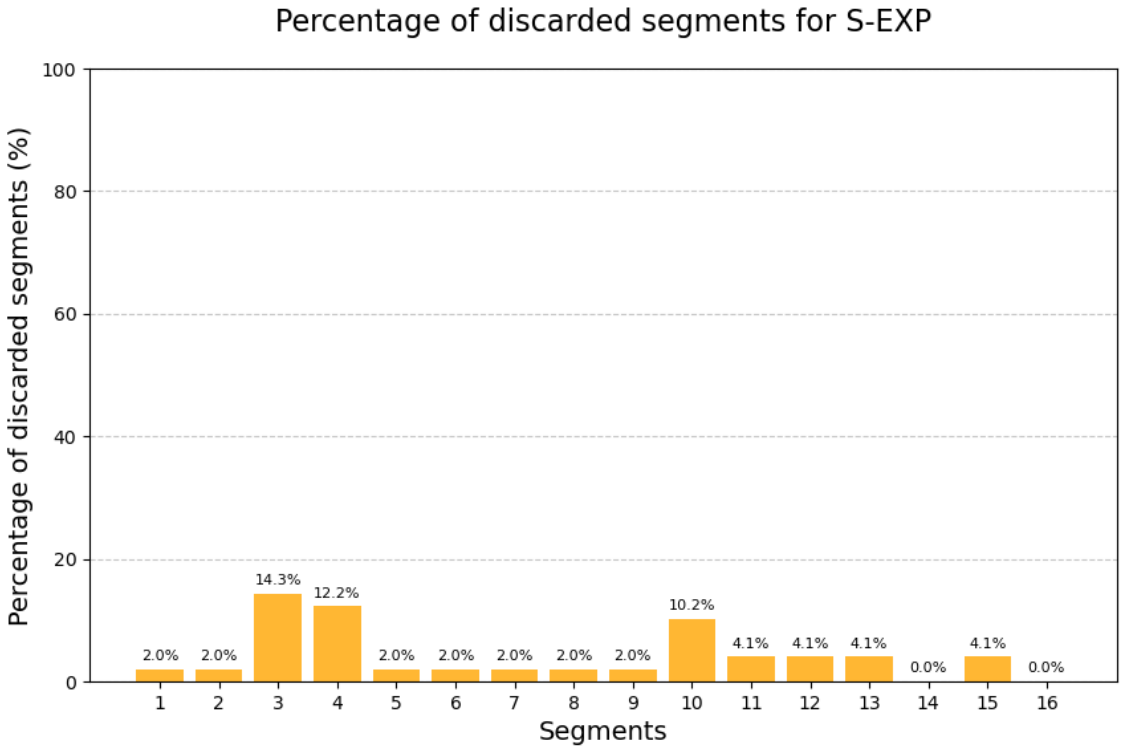
Percentage of discarded segments for S-EXP
Percentage of discarded segments (%)
Segments
100
80
60
40
20
0
1 2 3 4 5 6 7 8 9 10 11 12 13 14 15 16
2.0% 2.0% 14.3% 12.2% 2.0% 2.0% 2.0% 2.0% 2.0% 10.2% 4.1% 4.1% 4.1% 0.0% 4.1% 0.0%

A

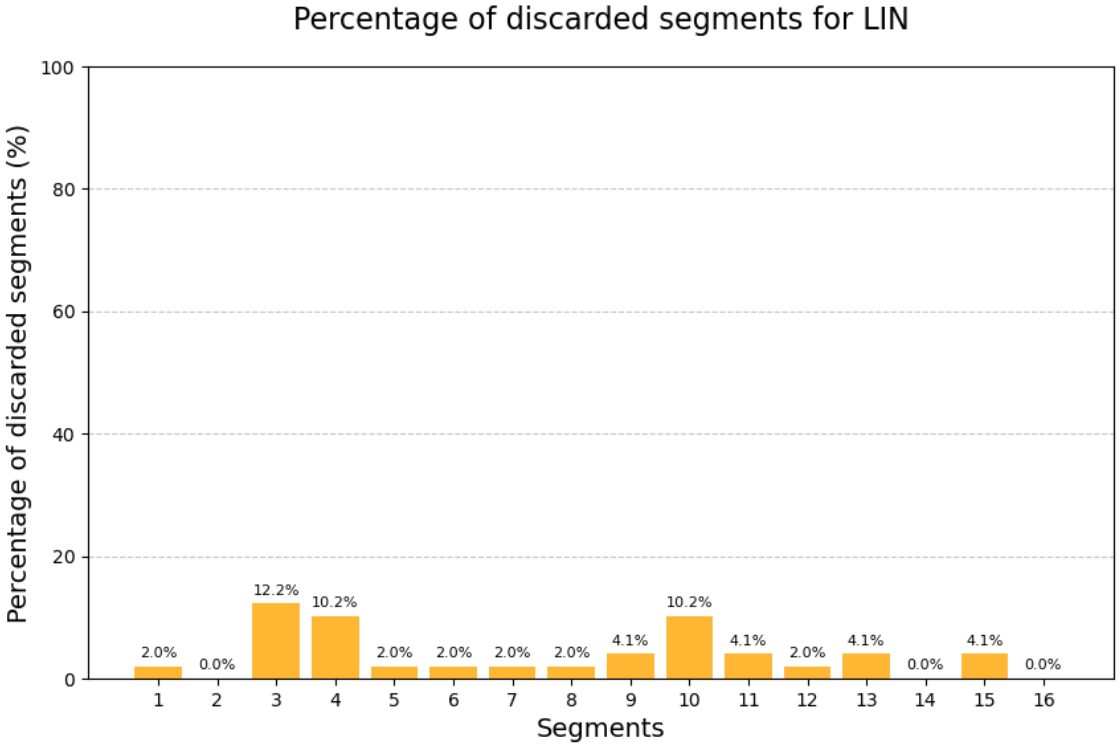
Percentage of discarded segments for LIN
Percentage of discarded segments (%)
Segments
100
80
60
40
20
0
1 2 3 4 5 6 7 8 9 10 11 12 13 14 15 16
2.0% 0.0% 12.2% 10.2% 2.0% 2.0% 2.0% 2.0% 4.1% 10.2% 4.1% 2.0% 4.1% 0.0% 4.1% 0.0%

B

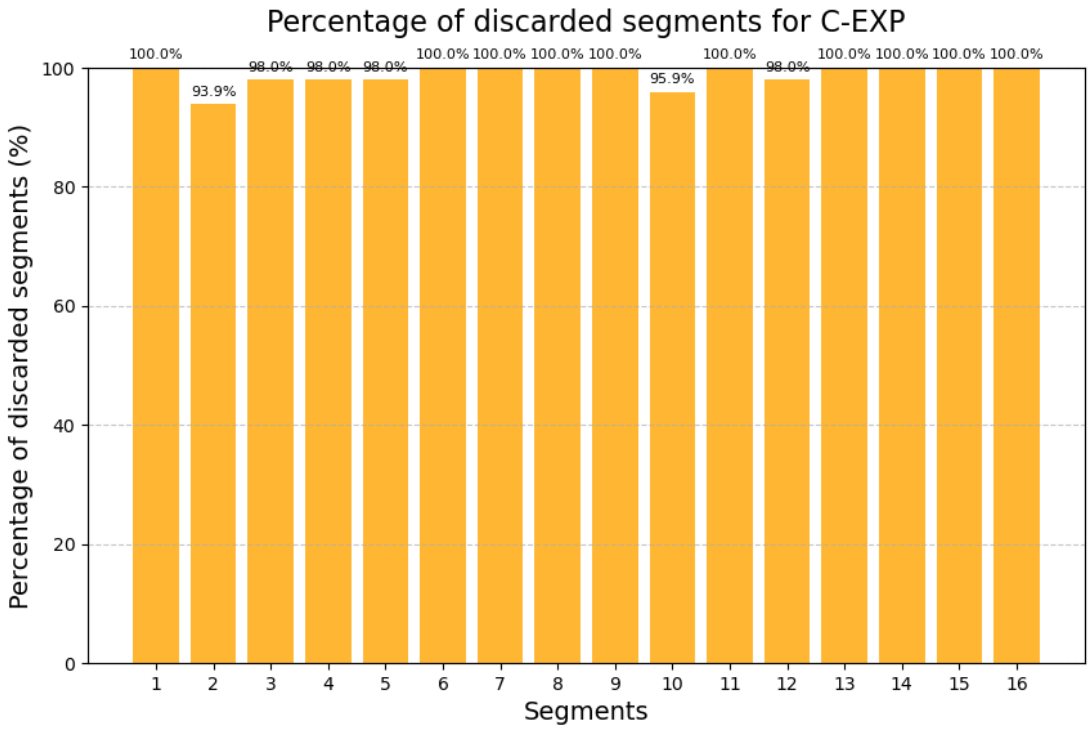

C

Figure 4.22. Percentage of deleted segments across all healthy subjects by setting a cv threshold equal to 10% in S-EXP, LIN, C-EXP model (ROI-based approach).

4.5.2 Patients

In the following histograms (Figure 23), the percentage of discarded voxel in each segment considering all patients are shown for each of the implemented models. The same analysis was performed with ROI-based approach models, and the percentage of discarded segments is shown Figure 24.

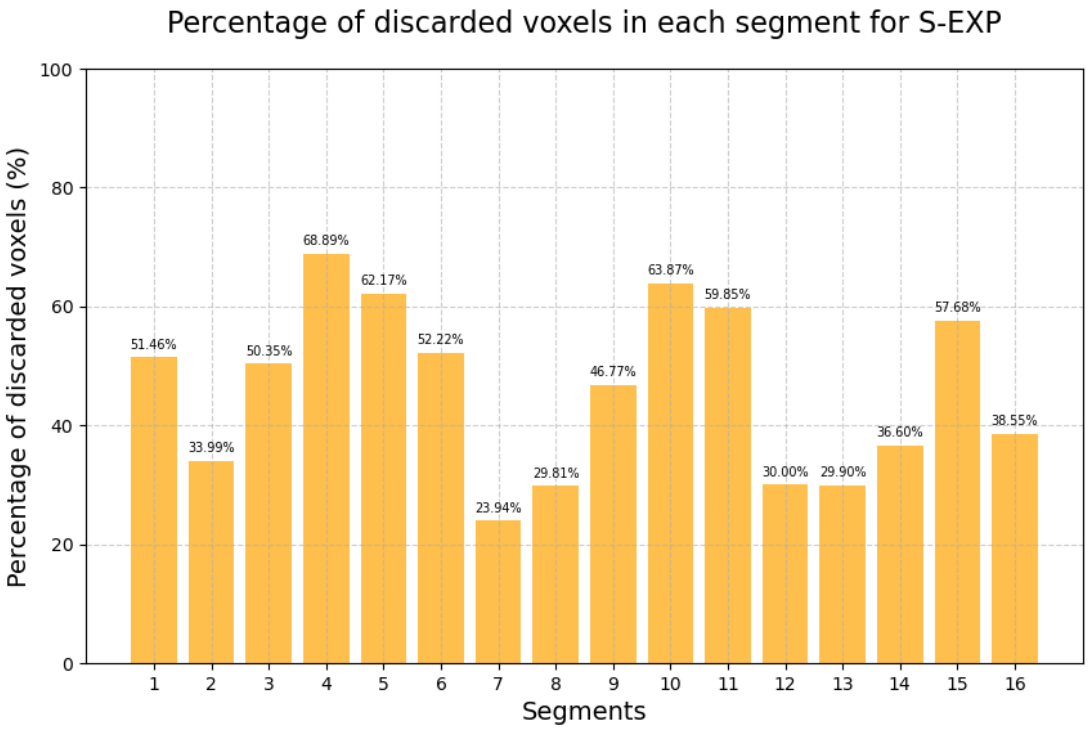
Percentage of discarded voxels in each segment for S-EXP
Percentage of discarded voxels (%)
Segments
0
20
40
60
80
100
1
2
3
4
5
6
7
8
9
10
11
12
13
14
15
16
51.46%
33.99%
50.35%
68.89%
62.17%
52.22%
23.94%
29.81%
46.77%
63.87%
59.85%
30.00%
29.90%
36.60%
57.68%
38.55%

A

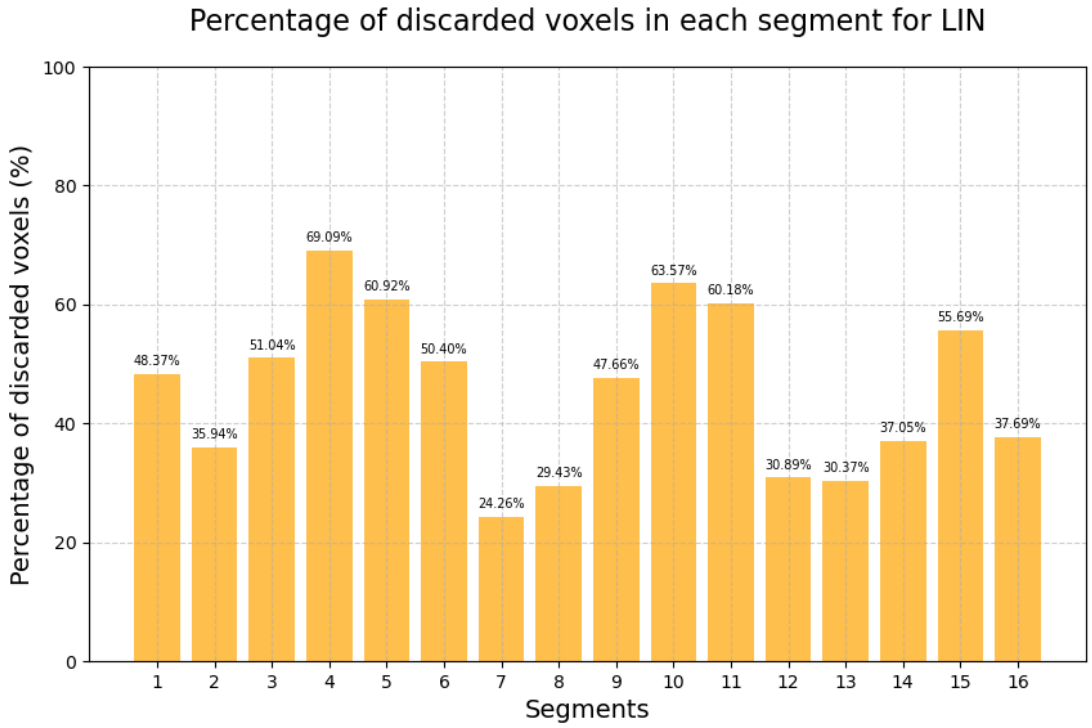
Percentage of discarded voxels in each segment for LIN
Percentage of discarded voxels (%)
Segments
0
20
40
60
80
100
1
2
3
4
5
6
7
8
9
10
11
12
13
14
15
16
48.37%
35.94%
51.04%
69.09%
60.92%
50.40%
24.26%
29.43%
47.66%
63.57%
60.18%
30.89%
30.37%
37.05%
55.69%
37.69%

B

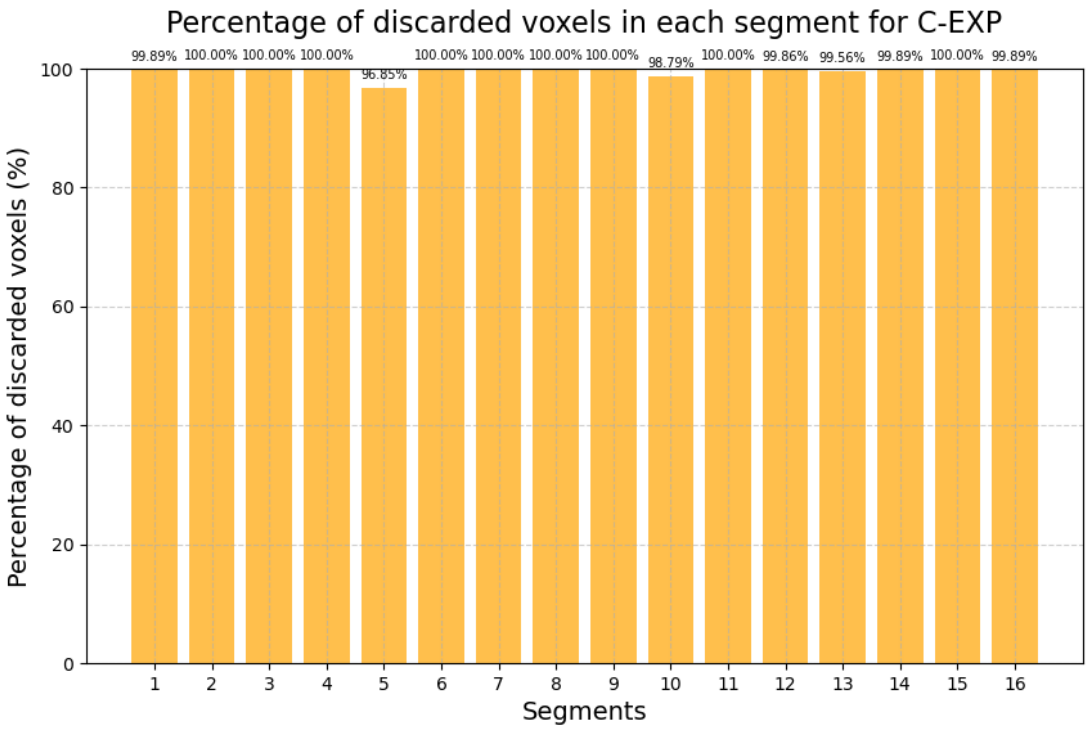

C

Figure 4.23. Percentage of deleted voxels across all patients by setting a cv threshold equal to 10% in S-EXP (A), LIN (B), C-EXP (C) models (pixel-wise approach).

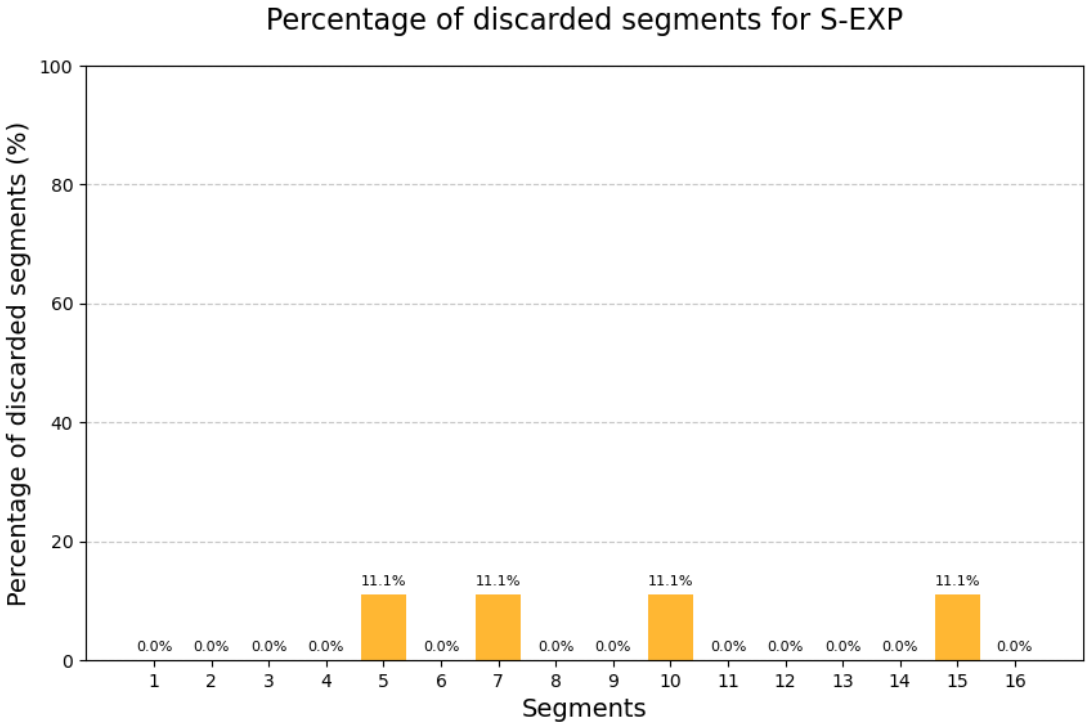

A

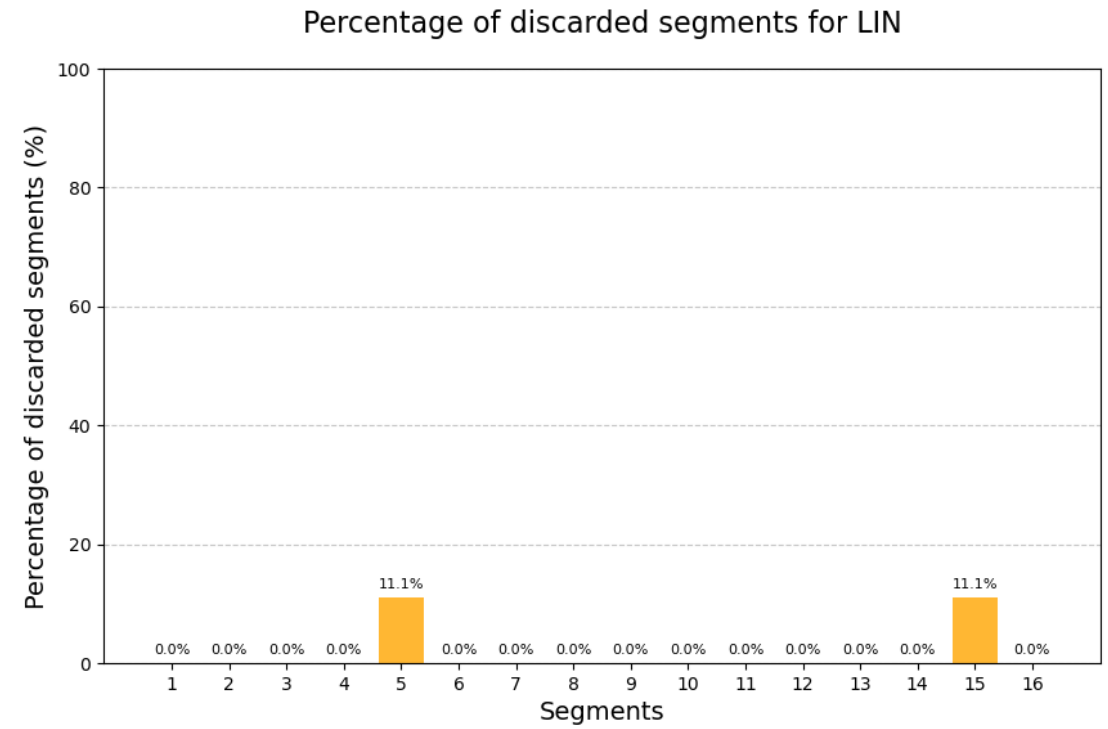

B

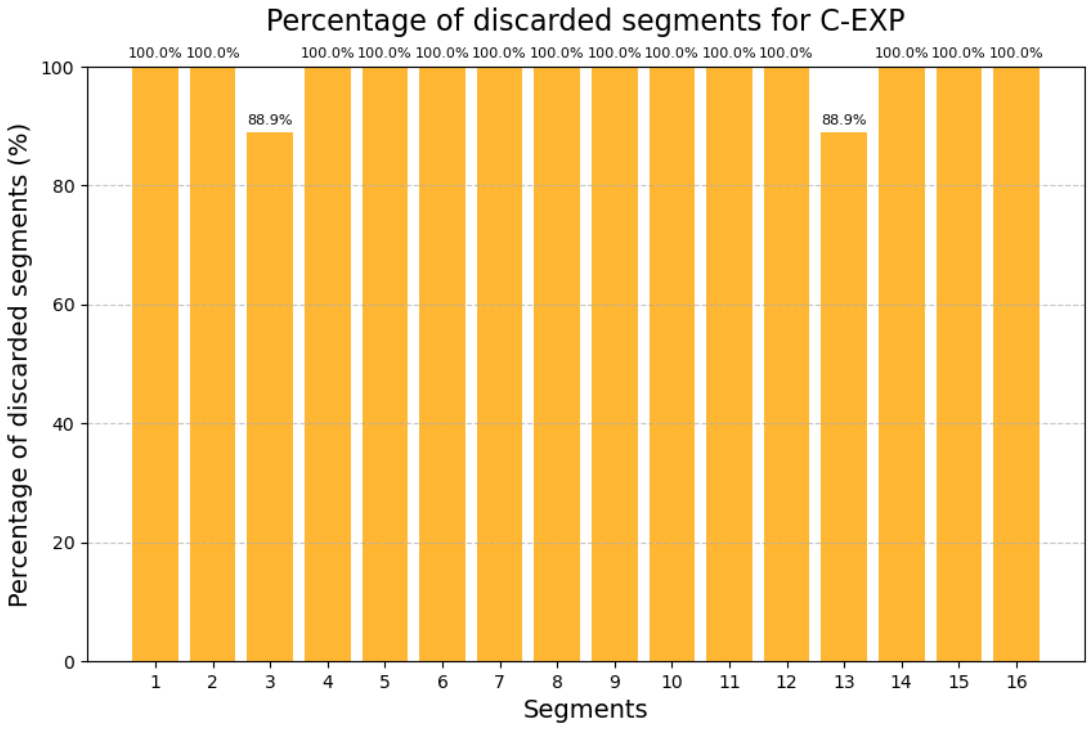

C

Figure 4.24 Percentage of deleted segments across all patients by setting a cv threshold equal to 10% in S-EXP, LIN, C-EXP model (ROI-based approach).

4.5.3 Best model selection considering CV threshold

From the results shown in the previous section, it is possible to observe that in C-EXP model all the voxels show a CV threshold (associated with T2* estimates) that are higher than 10% and so in this model all voxels are discarded. The same consideration is valid also in ROI-based results, where all segments are deleted for the same reason. This analysis is better discussed in the next chapter, however we anticipate that, since the C-EXP model provided a very low precision in the estimation of the T2*, it will not be considered in the subsequent results. Moreover, to evaluate other aspect of robustness and how they impact the construction of the correction maps, we decided to exclude the linear model from further analysis and focus only on the single-exponential model. Histograms presented in section 4.4, which displays the results of the Bayesian Information Criterion analysis. Those histograms reveal a high percentage of voxels (in the pixel-wise approach) or segments (in the ROI-based approach) where S-EXP proves to be the best model. Moreover, the distribution of the estimates using the LIN and the S-EXP showed a very good agreement. Besides, we show through the boxplot below (Figure 4.25 and 4.26) how T2* values distribution changes with the new CV threshold.

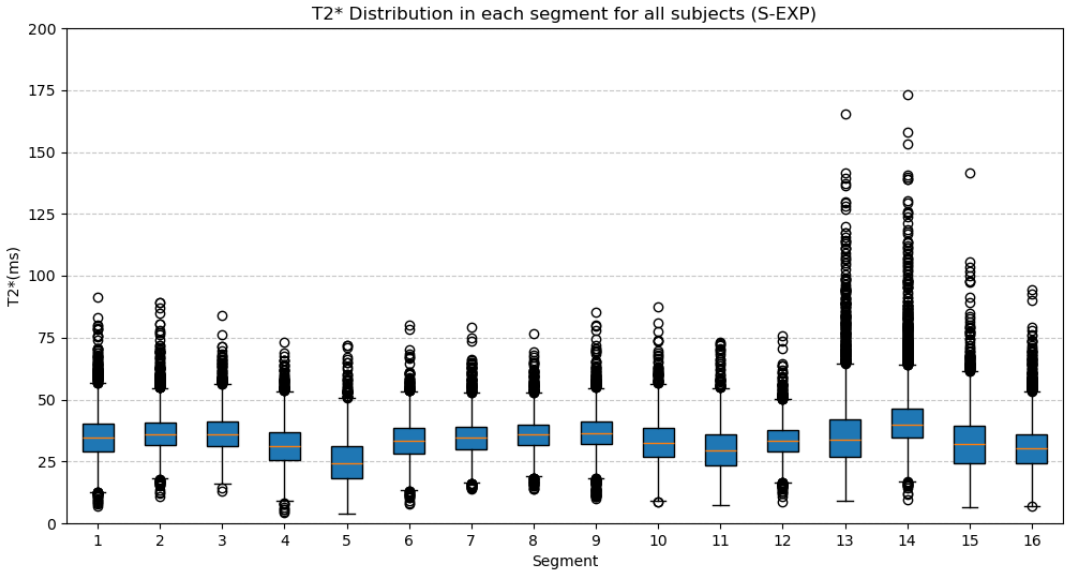

Figure 4.25. Boxplot for S-EXP model considering all healthy subjects with CV threshold equal to 10%.

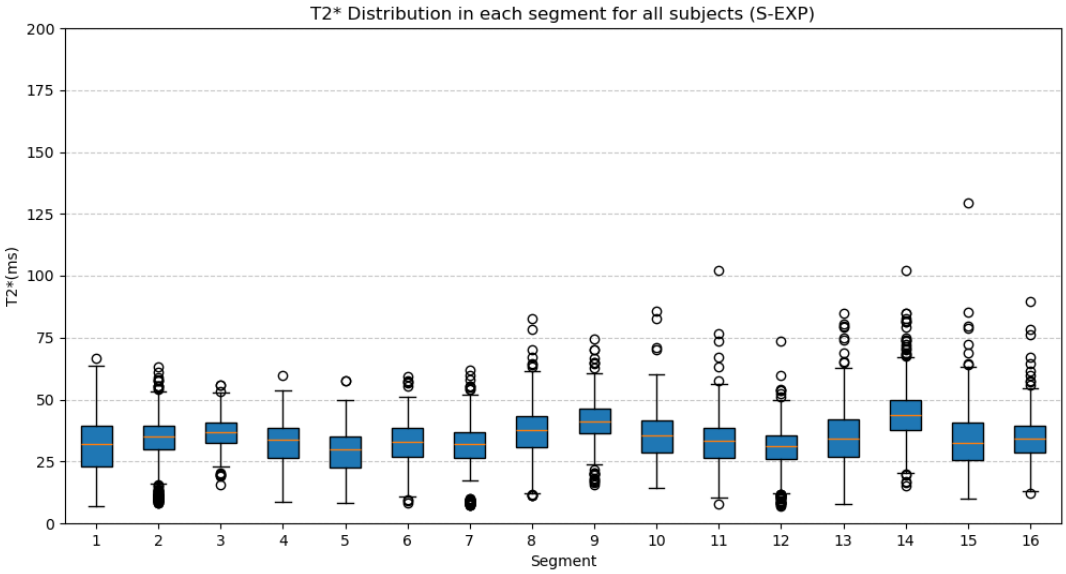

Figure 4.26. Boxplot for S-EXP model considering all patients with CV threshold equal to 10%.

4.6 S-EXP Results: comparison between Healthy Subjects and Patients (pixel-wise and ROI-based approach)

The aim of this section is to compare the trend of T2* values along segments in both healthy subjects and patients, in order to see if similar patterns characterize them. In Figure 4.27, mean and standard deviation in each segment across all healthy subjects is plotted against mean and standard deviation in each segment across all patients (both with pixel-wise approach). In figure 4.28, the same trend is analysed but considering ROI-based approach. Besides, also T2* estimated with HIPPO Software are reported in Figure 4.29. The last figures want to compare differences in T2* estimation between pixel-wise approach and ROI-based approach in healthy subjects (Figure 4.30 and 4.31) and patients (Figure 4.32 and 4.33).

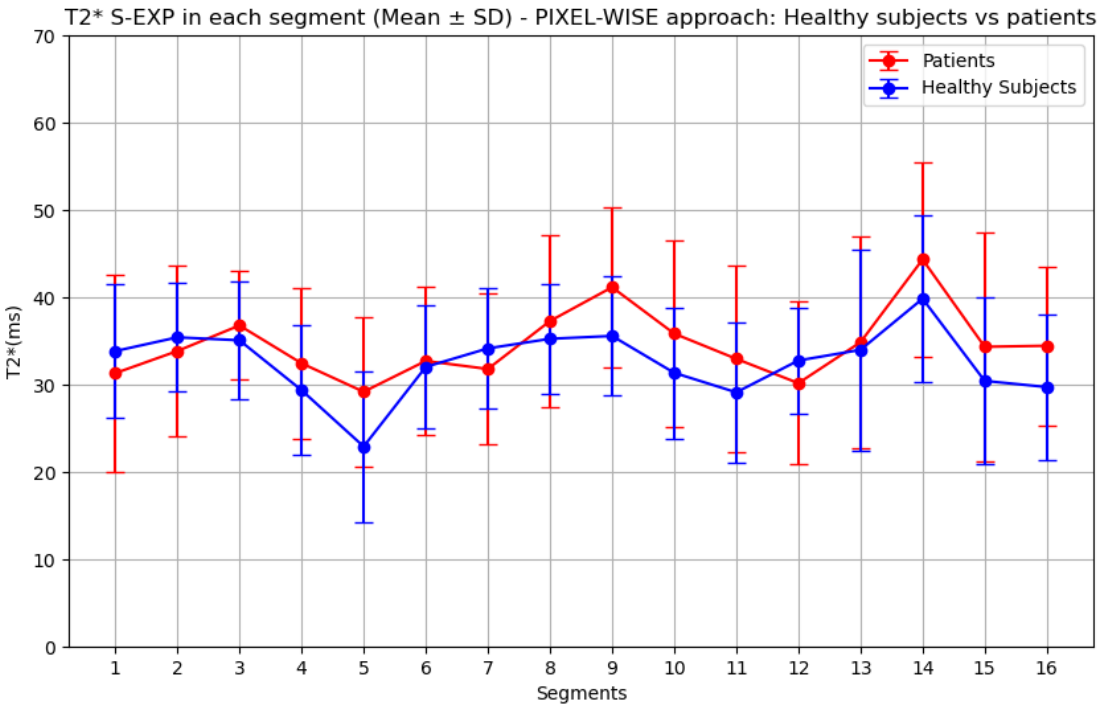

Figure 4.27. Healthy subjects VS Patients in S-EXP model with pixel-wise approach

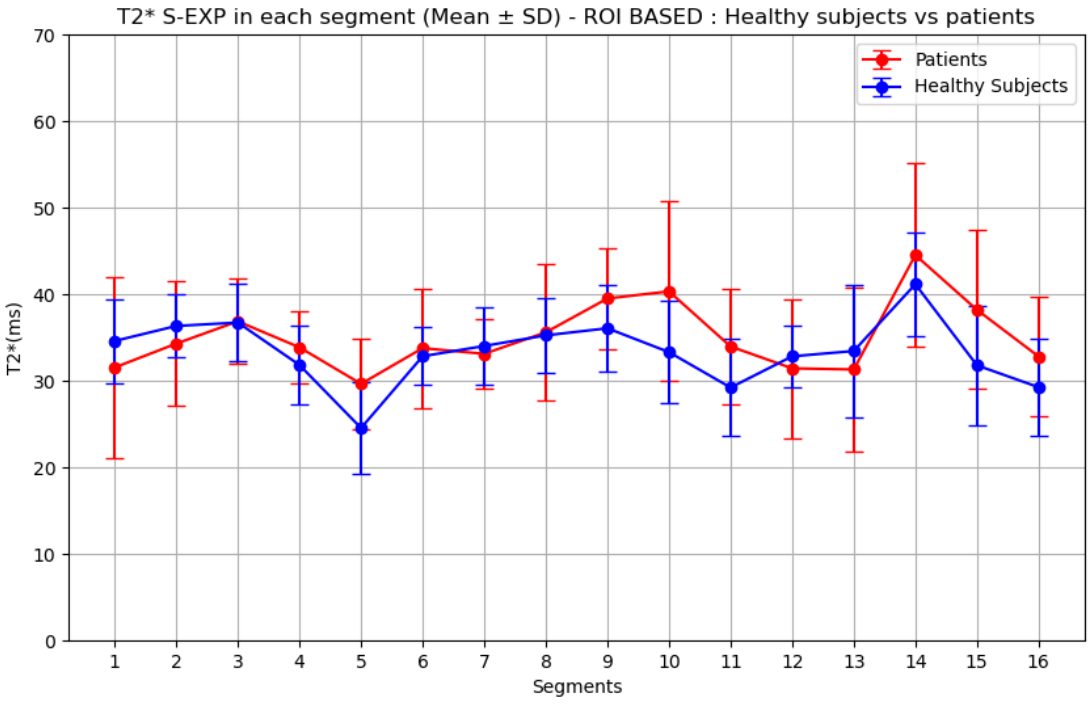

Figure 4.28. Healthy subjects VS Patients in S-EXP model with ROI-based approach

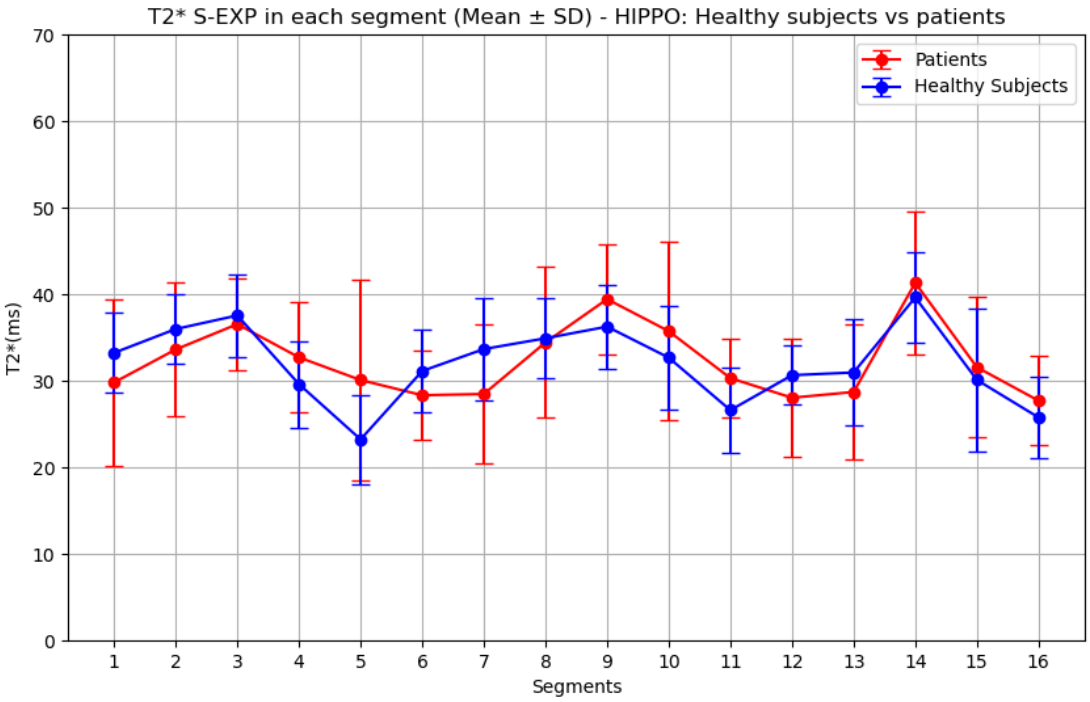

Figure 4.29. Healthy subjects VS Patients in HIPPO Software

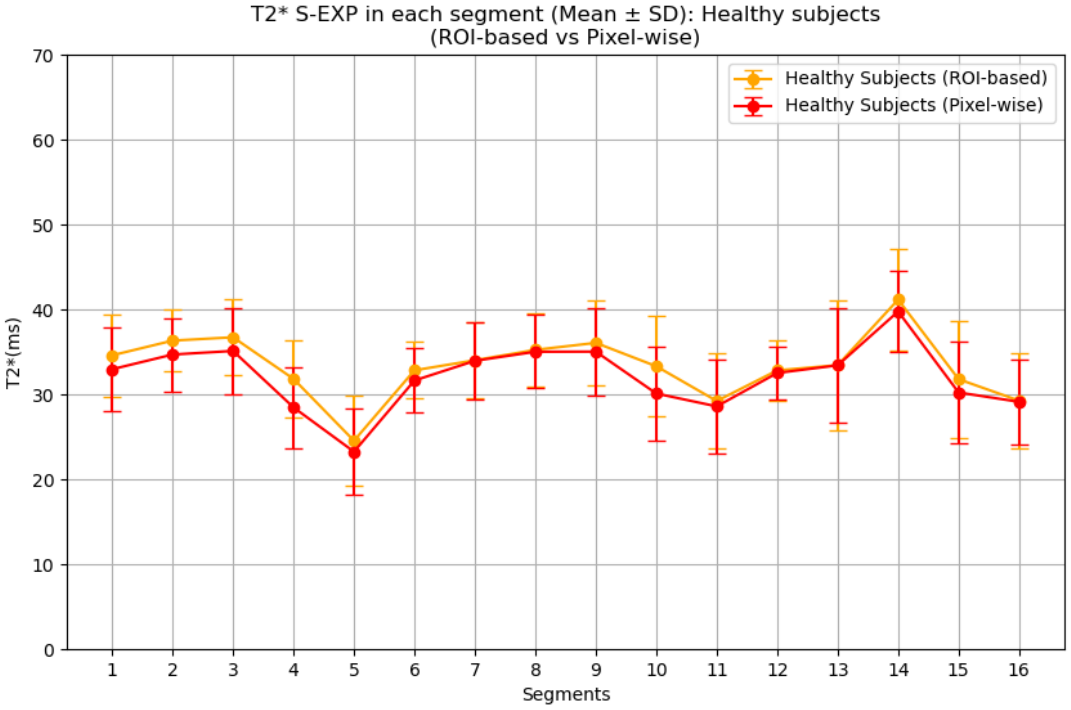

Figure 4.30. S-EXP model in pixel-wise approach VS ROI-based approach in healthy subjects

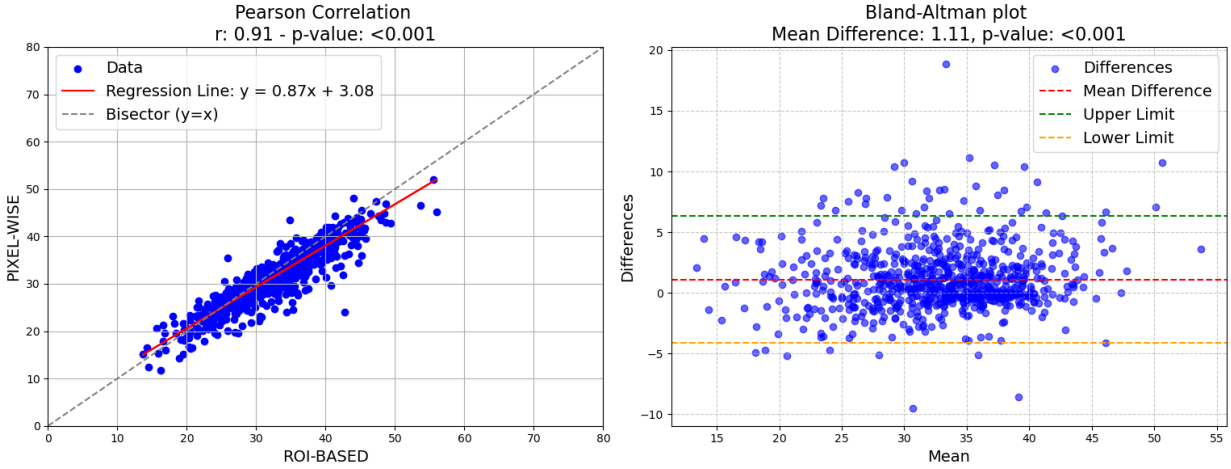

Figure 4.31. Pearson Correlation and Bland-Altman Plot between T2* values calculated in pixel-wise approach and ROI-based approach in healthy subjects

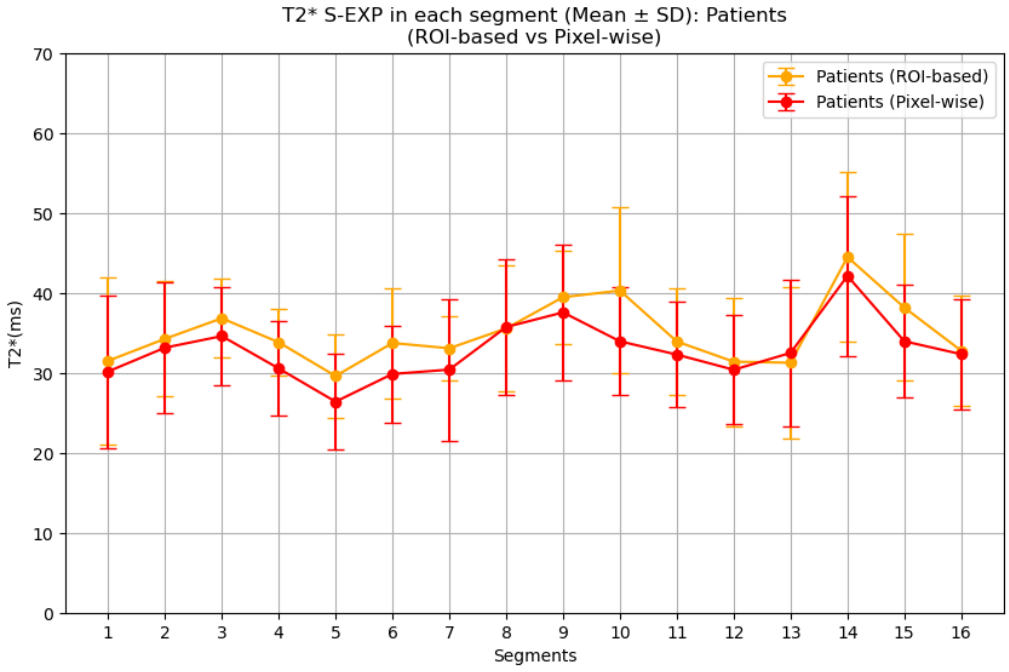

Figure 4.32. S-EXP model in pixel-wise approach VS ROI-based approach in patients

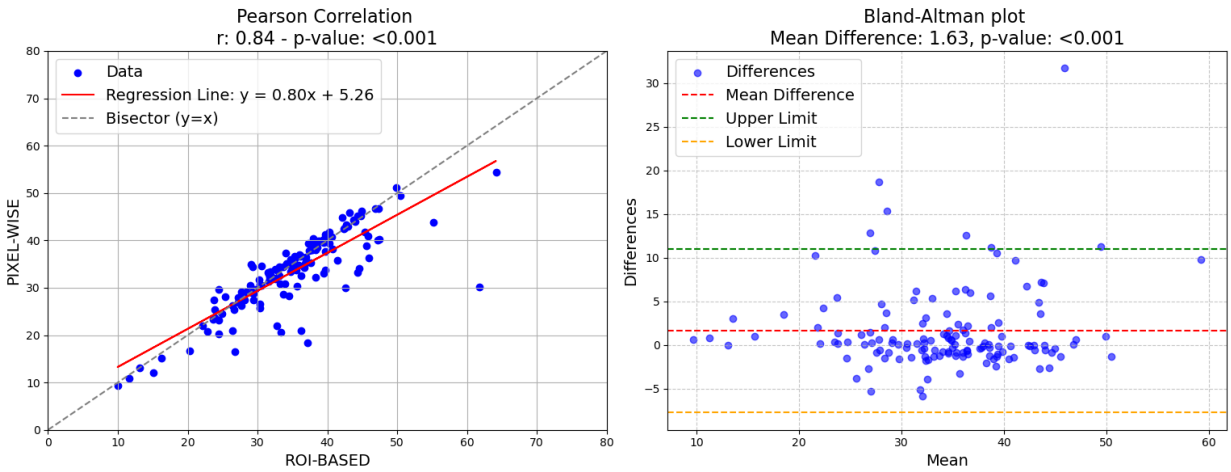

Figure 4.33. Pearson Correlation and Bland-Altman Plot between T2* values calculated in pixel-wise approach and ROI-based approach in patients

4.7 Test-retest in Patients

Pearson's correlation and the Bland-Altman plot were used to analyse the test-retest results obtained in patients (Dataset 2). Figure 4.34 shows the mean T2* values obtained in each segment with the pixel-wise approach in both acquisitions, Figure 4.35 shows T2* values obtained with the ROI-based approach and Figure 4.36 the values calculated by the HIPPO software (pre-correction version). As specified before, all the estimations derive from the mono-exponential model. The pixel-wise approach led to a better agreement between the test and retest session, since the correlation coefficient is higher when compared with both HIPPO and the ROI based approach. Moreover, the Bland-Altman plot does not reveal any particular intrinsic or fixed bias when using the S_EXP model at the pixel-wise level, with a 10% CV threshold on the T2* parameter.

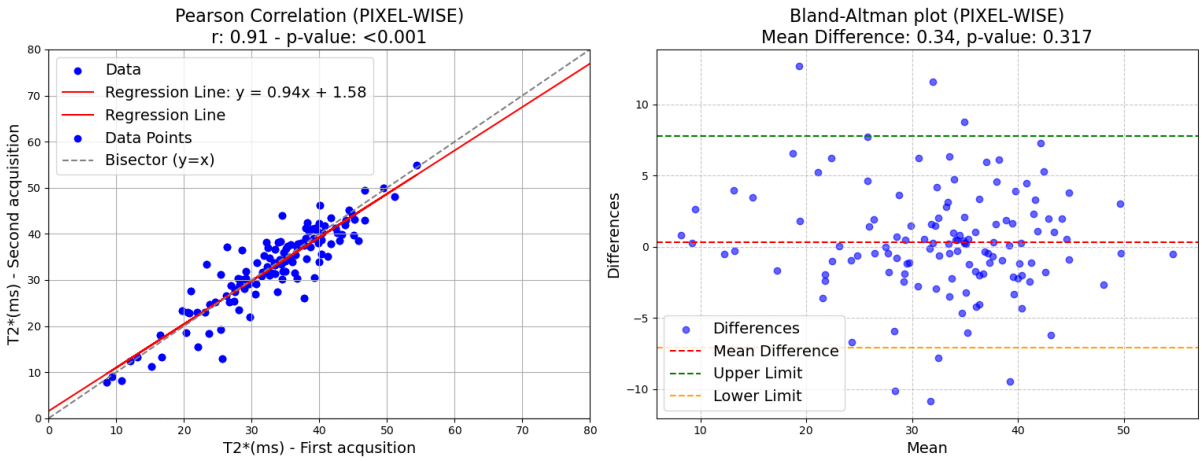

Figure 4.34. Pearson Correlation and Bland-Altman Plot between T2* obtained with pixel-wise approach in patients

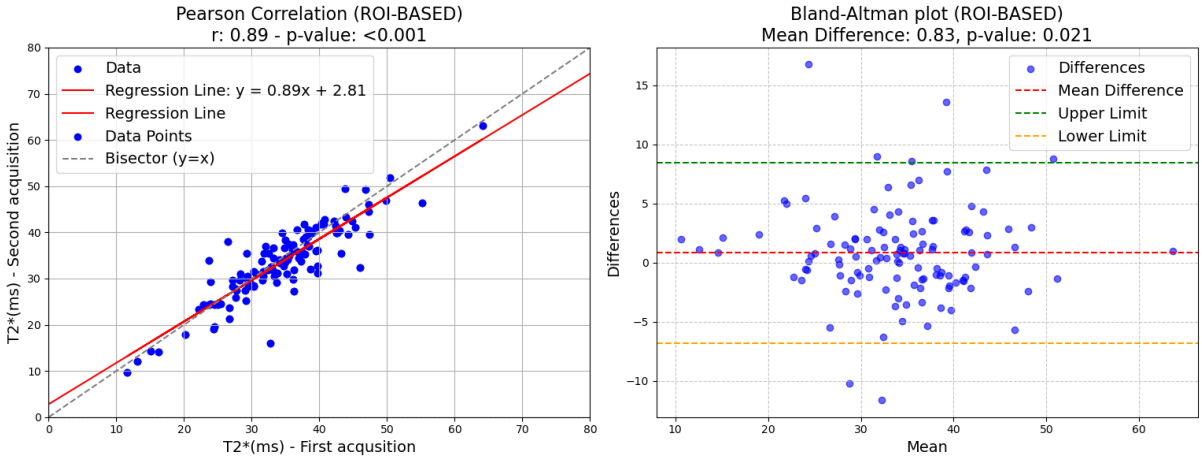

Figure 4.35. Pearson Correlation and Bland-Altman Plot between T2* obtained with ROI-based approach in patients

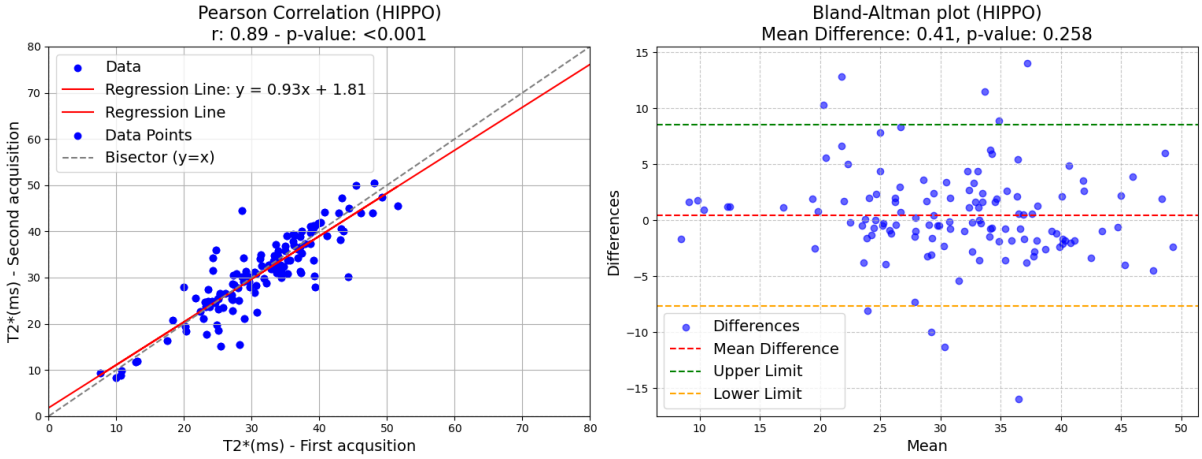

Figure 4.36. Pearson Correlation and Bland-Altman Plot between T2* obtained by HIPPO Software in patients

4.8 Comparison Between HIPPO results and S-EXP results

To better understand the differences between T2* estimates obtained using the implemented mono-exponential model and those generated by the HIPPO software, the Pearson correlation and Bland-Altman plot analyses were exploited again. The first section (Figures 4.37, 4.38, 4.39) presents the mean T2* values for the segments derived from healthy subjects while the second section (Figures 4.40, 4.41, 4.42) focuses on the mean T2* values for the segments from patients. The analysis involved T2* values obtained using a pixel-wise approach, with both the mean and median calculated. In fact, for each patient and segment, it was possible to select either the mean T2* value across the voxels in that specific segment or the median value. Both approaches were evaluated to identify potential differences, as the median is less sensitive to outliers and could provide a more robust result. Additionally, the results were evaluated using T2* values obtained in ROI-based approach, consistent with the algorithm employed in HIPPO. In ROI-based approach, only one T2* value for segment is directly obtained in the estimation process, and so it is no possible to account median values. We observe that in pixel-wise approach, median values and mean values lead to the same Pearson correlation index, in both healthy subjects and patients. Moreover, Bland-Altman plots show a mean difference almost equal to zero, and do not reveal any particular or systematic bias. In ROI-based approach, different results were obtained. We see a stronger correlation in both healthy subjects and patients, and a systematic bias is introduced in Bland-Altman Plot.

4.8.1 Healthy subjects

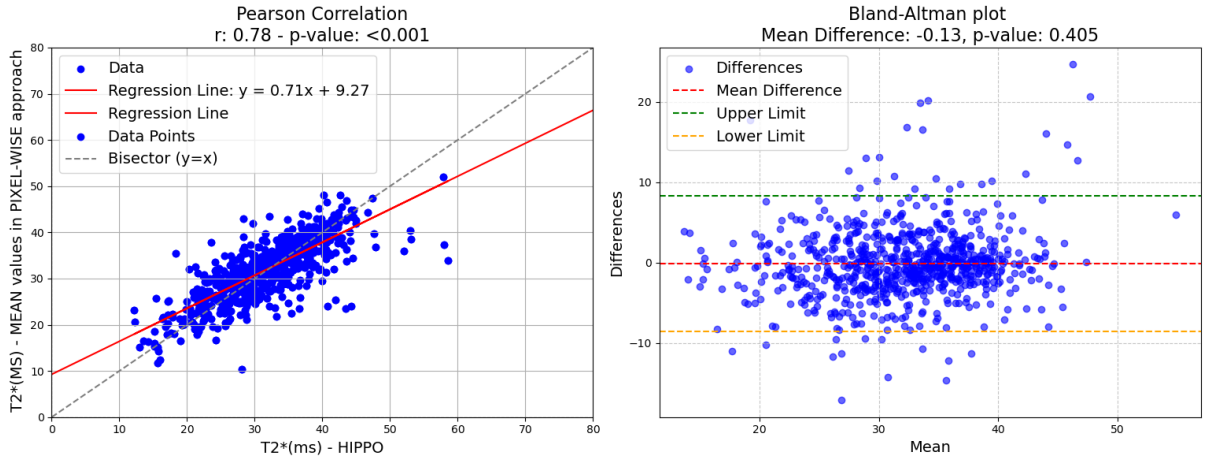

Figure 4.37. Pearson Correlation and Bland-Altman Plot between T2* mean values obtained in pixel-wise analysis and T2* mean values provided by HIPPO

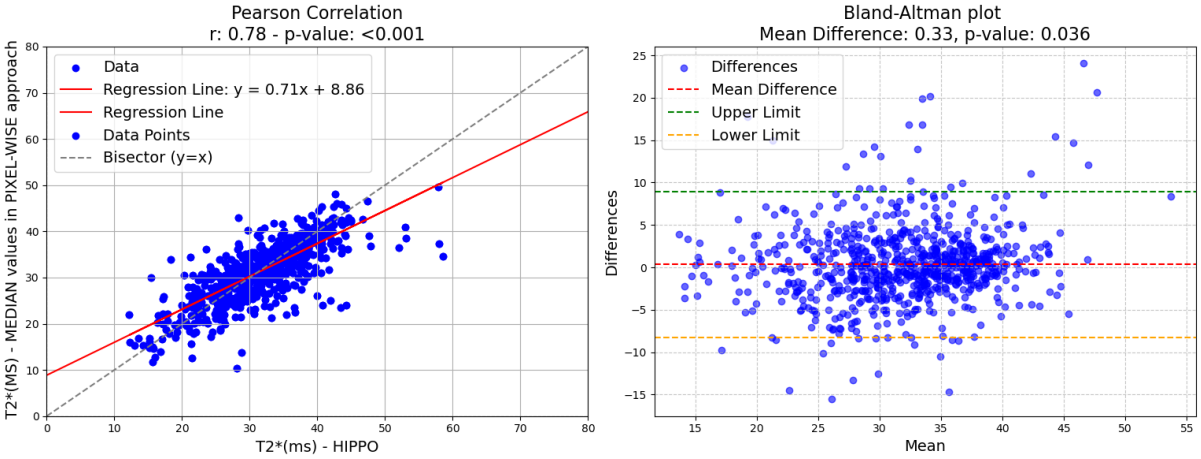

Figure 4.38. Pearson Correlation and Bland-Altman Plot between T2* median values obtained in pixel-wise analysis and T2* mean values provided by HIPPO

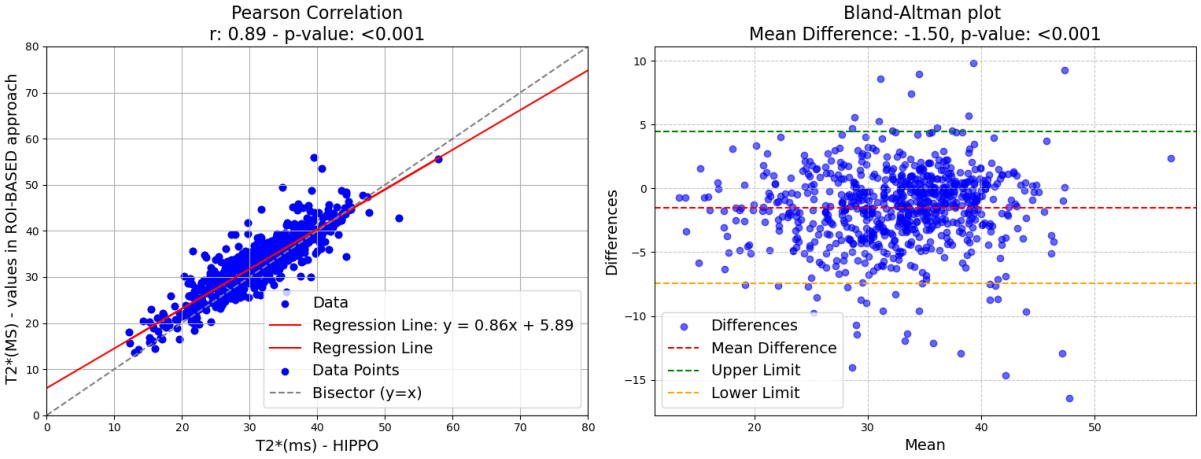

Figure 4.39. Pearson Correlation and Bland-Altman Plot between T2* mean values obtained in ROI-based analysis and T2* mean values provided by HIPPO

4.8.2 Patients

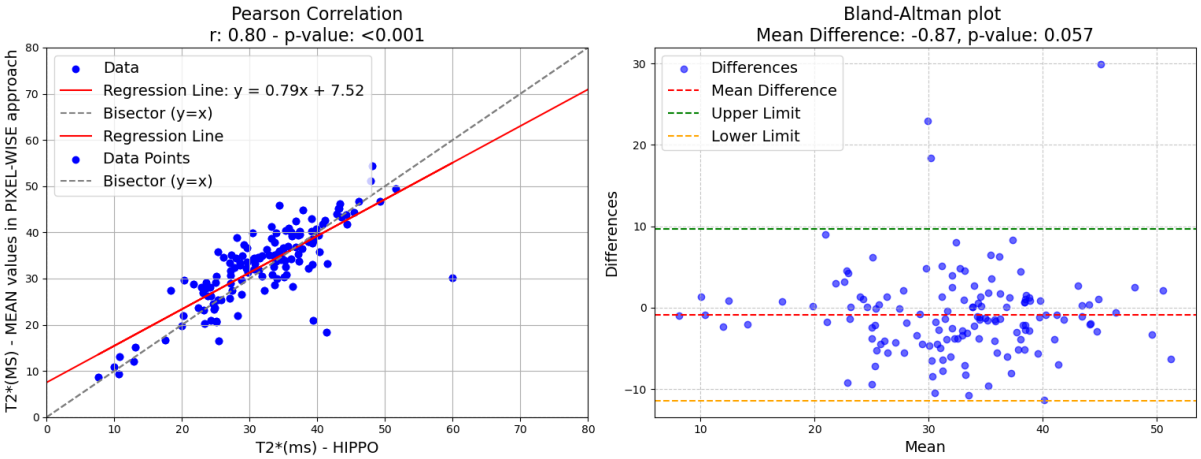

Figure 4.40. Pearson Correlation and Bland-Altman Plot between T2* mean values obtained in pixel-wise analysis and T2* mean values provided by HIPPO

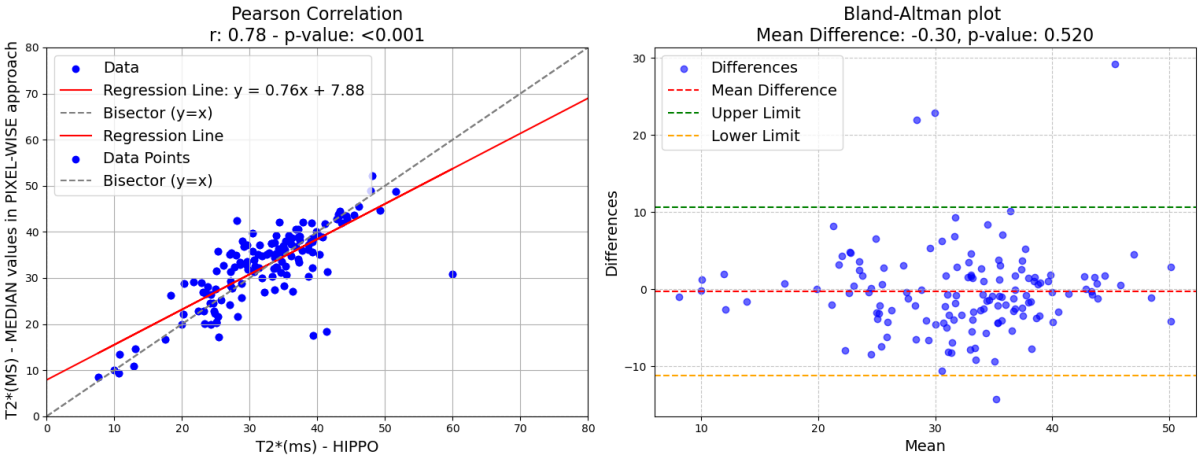

Figure 4.41. Pearson Correlation and Bland-Altman Plot between T2* median values obtained in pixel-wise analysis and T2* mean values provided by HIPPO

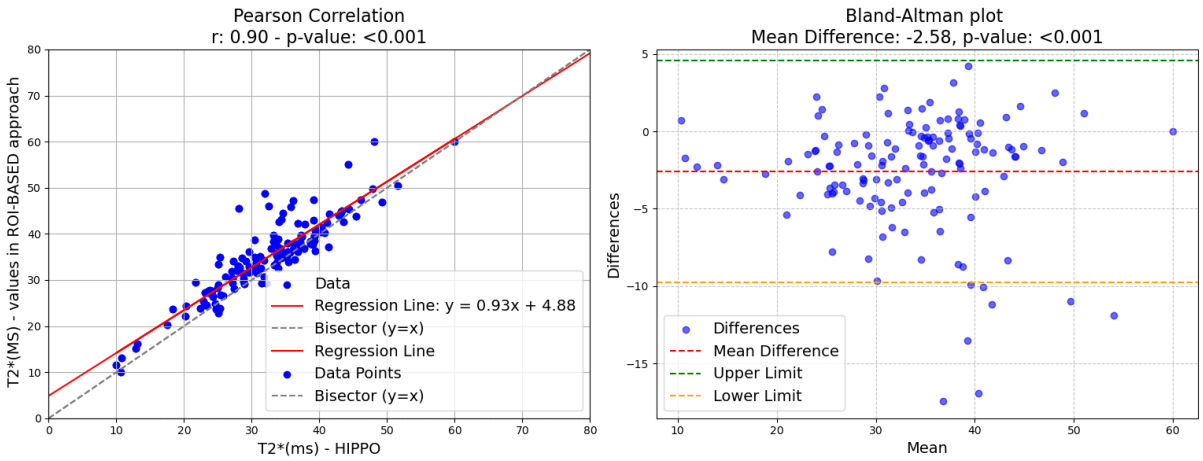

Figure 4.42. Pearson Correlation and Bland-Altman Plot between T2* mean values obtained in ROI-based analysis and T2* mean values provided by HIPPO

In the following Table (4.1) we report Pearson index coefficients obtained from the correlations analysis presented for both healthy subjects and patients.

	HEALTHY SUBJECTS S-EXP		
HEALTHY SUBJECTS HIPPO	Pixel-wise (mean)	Pixel-wise (median)	ROI-based
	0.78	0.78	0.89

A

	PATIENTS S-EXP		
PATIENTS HIPPO	Pixel-wise (mean)	Pixel-wise (median)	ROI-based
	0.80	0.78	0.90

B

Table 4.1. Pearson index obtained from correlation between T2* values obtained with HIPPO and with the implemented S-EXP model in all approaches for both health subjects (A) and patients (B)

4.9 Correction Factors

4.9.1 Correction Factors obtained with different approaches

This section is reserved to the calculation of correction factors. These factors were calculated with different approaches to see how much changes their values in terms of magnitude and sign. All factors in each method were calculated only exploiting T2* values of healthy subjects and with S-EXP model. In Table 4.2 are present R2* correction factors (expressed in Hz) obtained in pixel-wise approach T2* estimation (with both mean and median values) and ROI-based approaches. This means that the second column (CF_mean) shows the correction factors obtain considering T2* mean values in each segment of all subjects (following the procedure described in paragraph 2.3.1), while the third column (CF_median) shows the correction factors obtained with the same methodology but considering T2* median values across voxels in each segment. In the fourth column (CF_roibased), the factors obtained considering T2* values directly obtained from ROI-based method are shown. Pearson Correlation results between CF_mean and CF_median, and between CF_mean and CF_roibased are shown in Figure 4.43.

SEG	CF_mean	CF_median	CF_roibased	CF_cvi42
1	1,908	2,226	0,944	2.1
2	0,107	-0,006	-0,570	-0,7
3	0,209	0,141	-0,471	-1,1
4	6,934	6,775	3,488	20,3
5	15,485	16,988	14,060	22,8
6	2,835	2,487	2,345	4,1
7	0,884	0,849	1,307	4,1
8	-0,181	-0,159	0,168	2,2
9	0,181	0,159	-0,168	-2,2
10	5,753	6,254	2,449	3,7
11	7,057	7,232	6,730	19,4
12	1,804	1,675	2,105	8,2
13	1,953	2,504	2,785	14,7
14	-3,728	-3,582	-3,866	-5,6
15	5,417	6,303	4,580	-4,1
16	6,450	6,332	6,984	22

Table 4.2. Correction Factors obtained with different approaches from T2* values estimated in healthy subjects

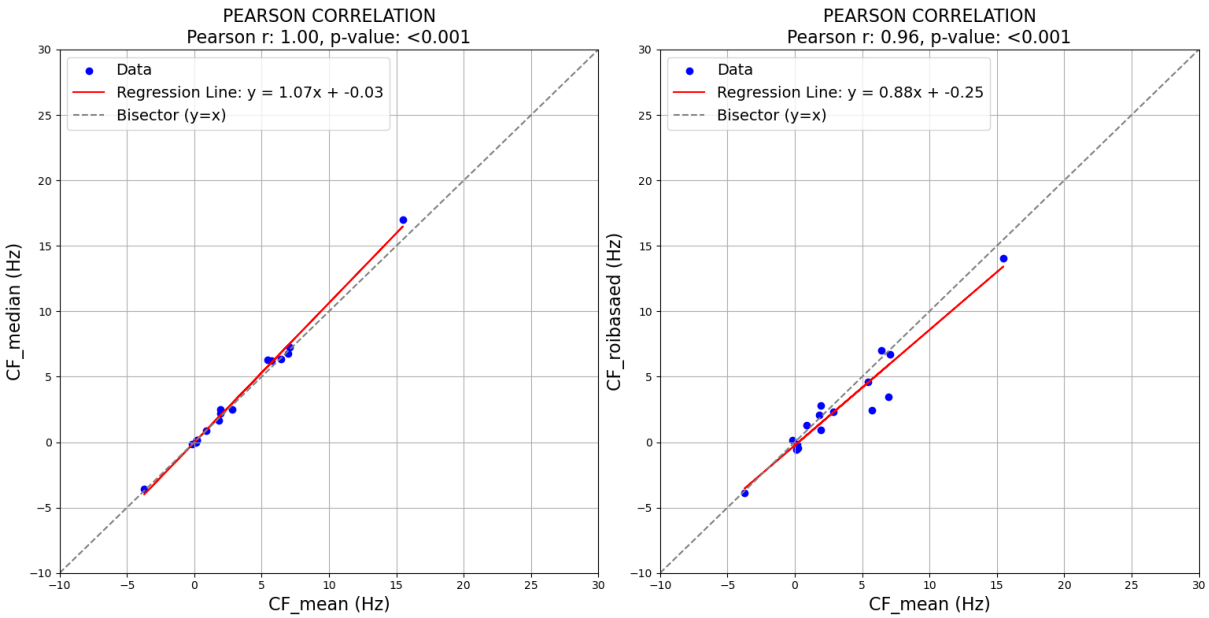

Figure 4.43. Pearson Correlation results between correction factors obtained in pixel-wise approach with mean T2*and median T2* (A) and between correction factors obtained in pixel-wise approach with mean T2*and ROI-based approach (B).

The same correction factors were calculated from the same Dataset of healthy subjects also in a previous thesis work [57], in which a Software called cvi42 (CIRCLE Cardiovascular imaging), specific for cardiac MRI analysis, was used. The correction factors obtained are presented in the last column of Table 4.2 (CF_cvi42). The segmentation with this tool was performed in a different way: all sixteen segments were manually drawn singularly. Pearson correlation and Bland-Altman Plot between the correction factors obtained from T2* mean values of each subject (CF_mean) and the correction factors obtained with cvi42 (CF_cvi42) are shown in next Figure (4.44). From this point onwards, only correction factors obtained considering T2* mean values in pixel-wise approach will be used.

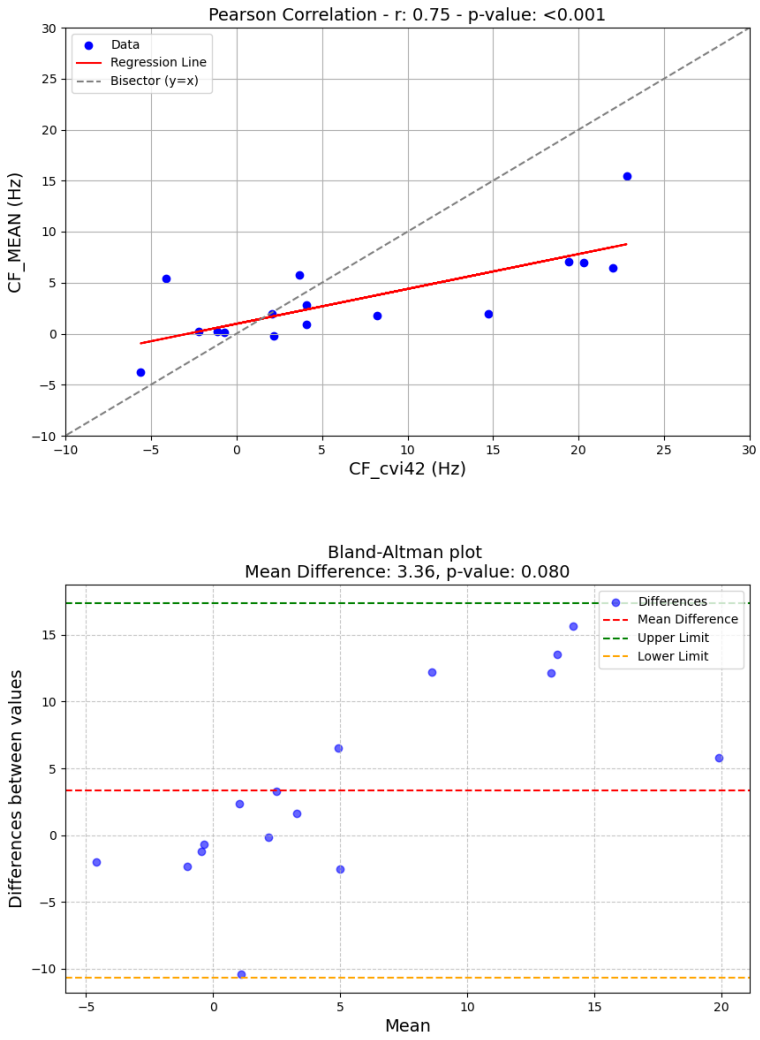

Figure 4.44. Pearson Correlation and Bland-Altman Plot between correction factors obtained from T2* mean values in pixel-wise technique and in cvi42 Software

4.9.2 Effect of the correction in T2* cut-off values

To identify the effect of the correction factors when the T2* estimated mean value in one segment is equal to 20 ms (cut-off conventionally used to determine if there is iron accumulation), we applied our correction factors to this T2* value. In addition, we repeat the same procedure considering an initial T2* value of 4 ms, which indicates a condition of extremely severe myocardial iron-overload (par 1.5.1). The aim of this table (4.3) is identifying in which segments there are important differences between the T2* value pre and post correction, and if this outcome is different in myocardial segments with a high quantity of iron. The more evident differences have been highlighted below.

Seg	Correction Factors (Hz)	Initial T2* (ms)	Corrected T2* (ms)	Initial T2* (ms)	Corrected T2* (ms)
1	1,908	20	20,79	4	4,03
2	0,107	20	20,04	4	4,00
3	0,209	20	20,08	4	4,00
4	6,934	20	23,22	4	4,11
5	15,485	20	28,97	4	4,26
6	2,835	20	21,20	4	4,05
7	0,884	20	20,36	4	4,01
8	-0,181	20	19,93	4	4,00
9	0,181	20	20,07	4	4,00
10	5,753	20	22,60	4	4,09
11	7,057	20	23,29	4	4,12
12	1,804	20	20,75	4	4,03
13	1,953	20	20,81	4	4,03
14	-3,728	20	18,61	4	3,94
15	5,417	20	22,43	4	4,09
16	6,450	20	22,96	4	4,11

Table 4.3. Effect of the correction in moderate myocardial iron-overload and in severe myocardial iron-overload

4.9.3 Correction Factors obtained considering subgroups of healthy subjects

To investigate the robustness of the correction factors (CF), the original dataset of healthy subjects was divided into five subgroups of 10 subjects each, and the factors were recalculated from the data of each subgroup. The results of the correction factors are shown in the Table 4.4, where the first column shows the original correction factors (calculated with the whole dataset and already shown in the first column of table 4.2), while the following columns (from 2 to 6) show the factors obtained from the subdivisions into groups of subjects. Figure 4.45 shows the trend of these calculated factors against the trend of true correction factors, while Figure 4.46 shows the differences between original factors and the other calculated factors.

CORRECTION FACTORS (Hz)						
Seg	**1-50**	**1-10**	**11-20**	**21-30**	**31-40**	**41-50**
1	1,908179	1,364151	1,570738	4,470109	0,331938	1,749554
2	0,10679	-0,03669	1,087705	0,352223	-1,32193	0,438294
3	0,208711	1,091861	1,206595	-0,13597	-0,82429	-0,20633
4	6,933942	10,0718	7,206649	7,471956	4,755358	5,477734
5	15,48488	17,41178	15,65931	14,09041	18,73382	11,72177
6	2,835165	3,513393	3,404323	4,629842	0,520668	2,175423
7	0,884143	0,422099	1,738032	2,530005	-1,22531	0,909684
8	-0,18081	-1,21426	-0,03638	0,645881	-0,62713	0,22451
9	0,180807	1,214263	0,03638	-0,64588	0,627128	-0,22451
10	5,75329	11,07804	4,733826	4,731507	4,051245	4,704308
11	7,057396	3,624626	6,798267	8,978217	8,66097	6,881623
12	1,804048	1,595038	3,406411	2,367626	-0,73397	2,364232
13	1,952612	2,080384	3,502266	-0,04303	-0,74745	4,983663
14	-3,72808	-3,31576	-2,07937	-3,75424	-5,83149	-3,61827
15	5,416756	7,125378	7,782726	3,204738	0,575287	8,566511
16	6,449772	3,514628	6,053705	4,877186	9,367234	8,14259

Table 4.4. Correction Factors obtained considering subgroups of healthy subjects

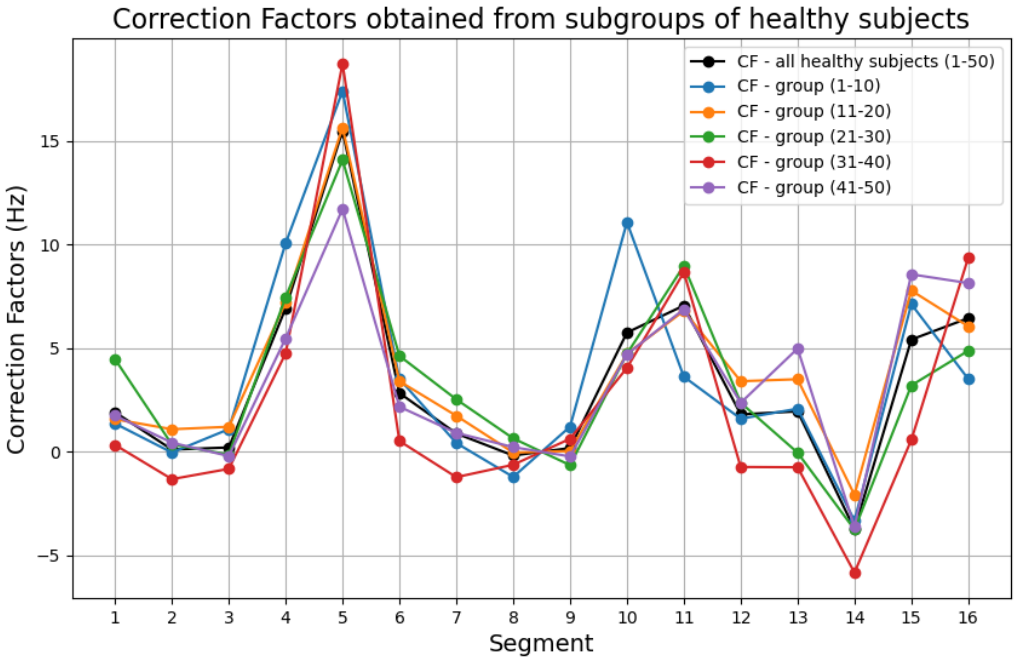

Figure 4.45. Correction Factors obtained from all healthy subjects (column 1 of Table 4.4) against factors obtained from each subgroup of subjects (columns 2-6 of Table 4.4)

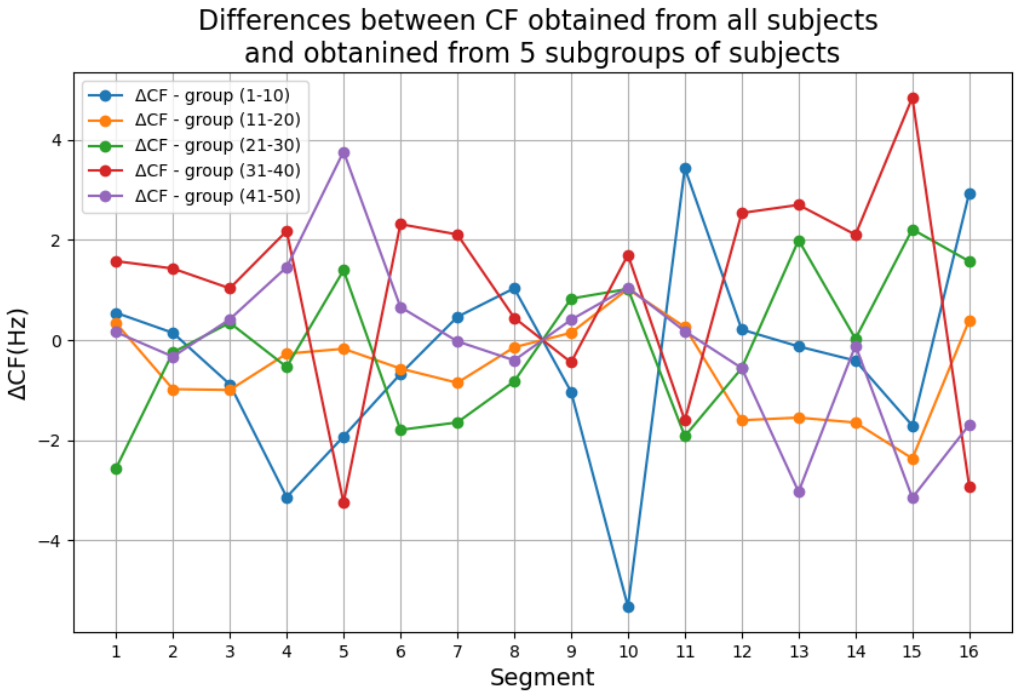

Figure 4.46. Differences between Correction Factors obtained from all healthy subjects (column 1 of Table 4.4) and factors obtained from each subgroup of subjects (columns 2-6 of Table 4.4)

The single magnitude of the correction factor does not provide meaningful information about its impact on the correction process. To address this, the following table presents all T2* values adjusted using the corresponding correction factors listed in the previous table. Additionally, correlations between the T2* values corrected with the original factors and those adjusted using the newly calculated correction factors were analysed and are illustrated in Figure 4.47. Given that a T2* value of 20 ms is the established threshold for diagnosing iron overload, this value was considered in each segment prior to the application of the correction map. The corrected T2* values derived from this process aim to demonstrate the influence of the correction methodology on diagnostic outcomes and shows the results for borderline patients.

T2* (ms) - POST CORRECTION						
Seg	**1-50**	**1-10**	**11-20**	**21 -30**	**31-40**	**41-50**
1	20,79356	20,56097	20,64867	21,96359	20,13366	20,7252
2	20,04281	19,98534	20,44476	20,14189	19,48485	20,17687
3	20,08383	20,44649	20,49457	19,94576	19,67563	19,91781
4	23,22014	25,04495	23,36812	23,5139	22,10206	22,46067
5	28,97281	30,68594	29,11998	27,84772	31,98344	26,12451
6	21,20224	21,51157	21,46122	22,04092	20,21046	20,90975
7	20,36002	20,17028	20,72025	21,06594	19,5216	20,37062
8	19,92794	19,52581	19,98546	20,26173	19,75226	20,09021
9	20,07259	20,49779	20,01456	19,74494	20,25404	19,9106
10	22,60055	25,69244	22,09155	22,09042	21,76338	22,07715
11	23,2869	21,56317	23,14722	24,37729	24,19021	23,19197
12	20,74863	20,65904	21,46218	20,99412	19,71066	20,99263
13	20,81279	20,86828	21,50642	19,9828	19,70542	22,21416
14	18,61224	18,75618	19,20146	18,60318	17,91104	18,65036
15	22,42995	23,32382	23,68699	21,36968	20,23279	24,13507
16	22,96199	21,51214	22,75505	22,16174	24,61068	23,89063

Table 4.5. Post-correction T2* values (using correction factors obtained in table 4.4)

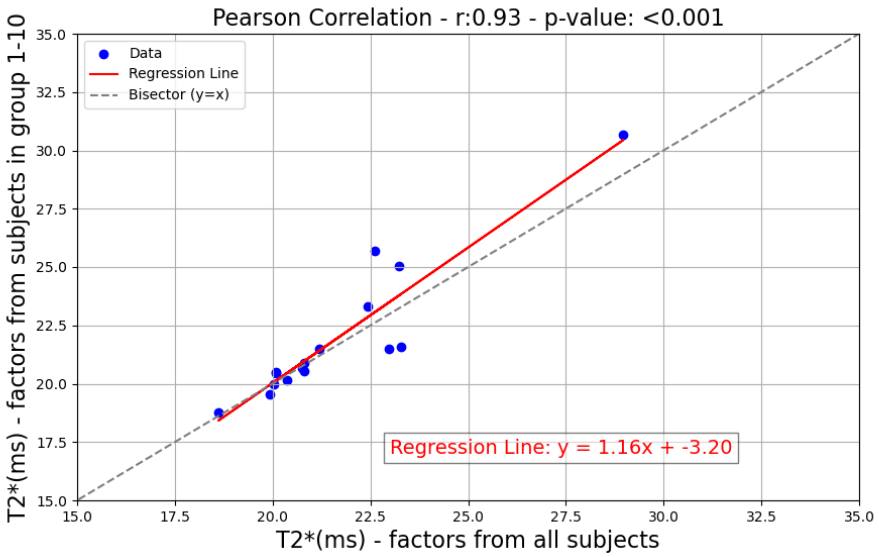

A

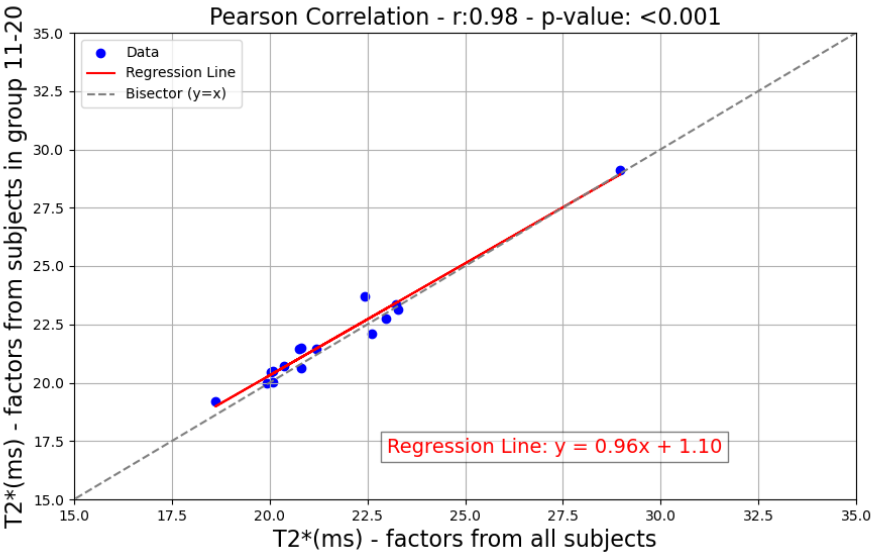
Pearson Correlation - r:0.98 - p-value: <0.001
Data
Regression Line
Bisector (y=x)
Regression Line: y = 0.96x + 1.10
T2*(ms) - factors from subjects in group 11-20
T2*(ms) - factors from all subjects

B

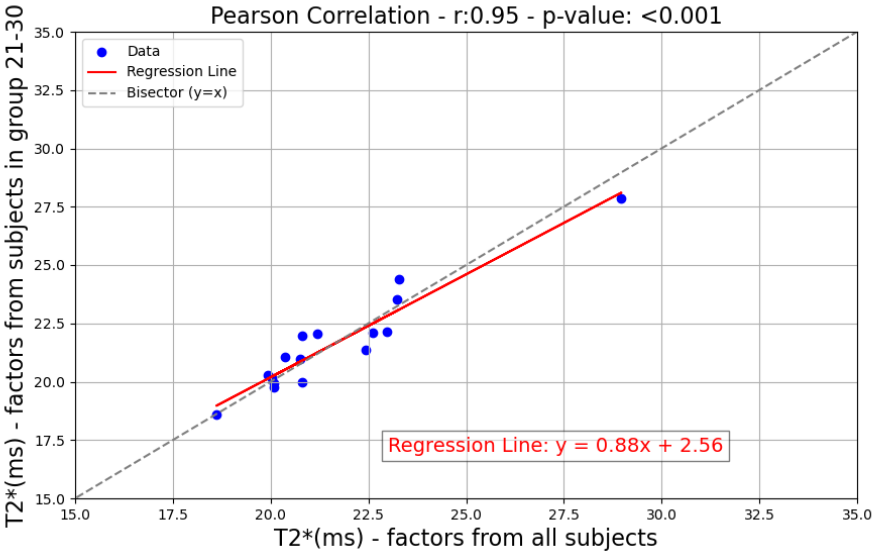
Pearson Correlation - r:0.95 - p-value: <0.001
Data
Regression Line
Bisector (y=x)
Regression Line: y = 0.88x + 2.56
T2*(ms) - factors from subjects in group 21-30
T2*(ms) - factors from all subjects

C

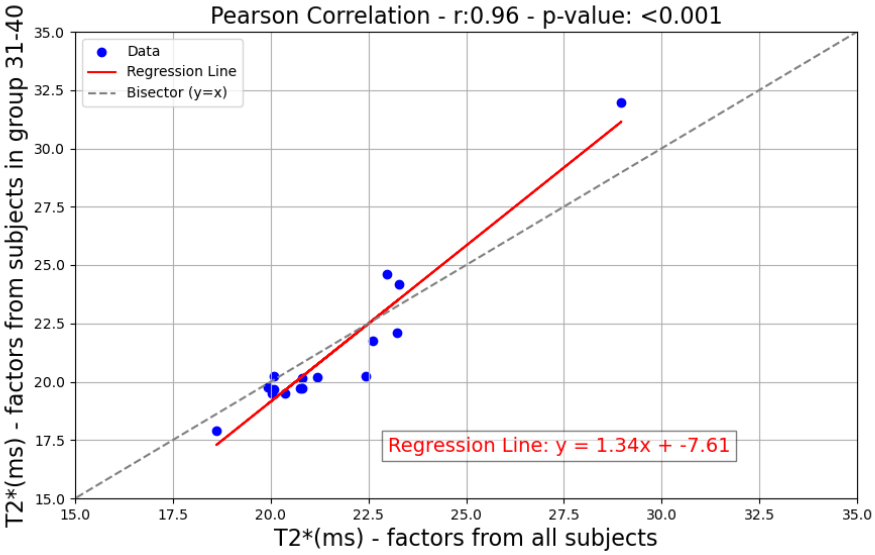
Pearson Correlation - r:0.96 - p-value: <0.001
Data
Regression Line
Bisector (y=x)
Regression Line: y = 1.34x + -7.61
T2*(ms) - factors from subjects in group 31-40
T2*(ms) - factors from all subjects

D

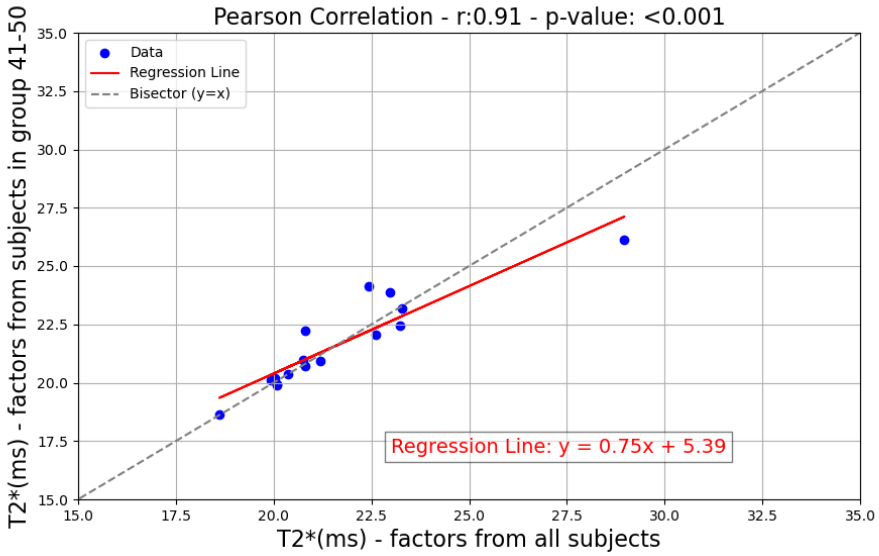

E

Figure 4.47. Pearson Correlation between T2* corrected with original factors (X-axis) and factors obtained of each subgroup (Y-axis) distinguished in each subplot: (A) group with subjects from 1 to 10, (B) group with subjects from 11 to 20, (C) group with subjects from 21 to 30, (D) group with subjects from 31 to 40, (E) group with subjects from 41 to 50.

Correction factors derived from each subgroup were applied to the patient dataset. The differences between T2* values corrected using the original factors (calculated from the entire healthy cohort) and those corrected using subgroup-specific factors were computed. For each subgroup, the mean difference vector was calculated by averaging the differences across the 10 patients. The five resulting mean difference vectors, along with their means and standard deviations, are represented in the following graph (Figure 4.48).

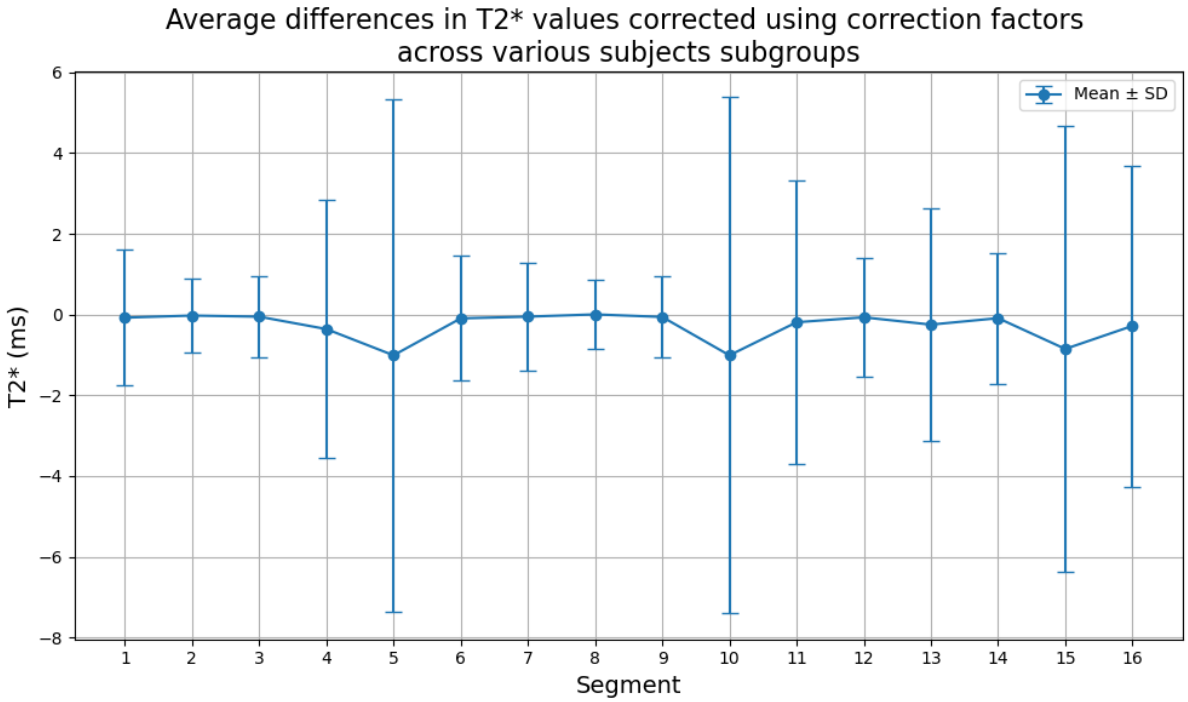

Figure 4.48. Mean and Standard deviation of differences in T2* values, across patients, corrected with original factors and corrected with factors obtained in each subgroup.

4.9.4 Correction Factors obtained through Fixed-Angles Mask Segmentation Rotations

Since the selection of the starting point of the interventricular septum is manually determined by the radiologist, it is crucial to account for the variability introduced by this process. Specifically, we aim to evaluate the robustness of the correction factors under the influence of systematic errors. To this end, we assume that all masks are rotated by fixed angles of 2°, 5°, 10°, and 20°, both clockwise and counterclockwise (with counterclockwise rotation considered positive). The resulting correction factors under these assumptions are provided below (Table 4.6). As in the previous section, a T2* value of 20 ms was uniformly assigned to each segment, and the new correction maps were applied. This analysis explores how variations in rotation affect the corrected outcomes (see Table 4.7 and Figure 4.49) and highlights the sensitivity of the correction methodology to systematic errors. Each plot in Figure 4.47 presents T2* values corrected with the original factors on the X-axis, while the Y-axis represents T2* values corrected with a specific angle of rotation. The first column illustrates results for counterclockwise rotations, whereas the second column shows results for clockwise rotations of the same angle.

CORRECTION FACTORS (Hz)									
Seg	**20°**	**10°**	**5°**	**2°**	**0°**	**-2°**	**-5°**	**-10°**	**-20°**
1	-0,789	-0,026	0,960	1,419	1,908	2,221	2,889	3,742	6,039
2	0,334	0,149	0,071	0,130	0,107	0,135	0,206	0,152	0,213
3	1,327	0,593	0,326	0,244	0,209	0,370	0,508	0,351	0,750
4	17,307	11,411	9,769	8,208	6,934	6,333	5,581	4,061	2,366
5	10,099	13,179	14,131	15,354	15,485	15,410	15,458	14,678	16,115
6	0,429	1,296	1,849	2,325	2,835	3,358	3,819	4,652	7,100
7	-0,239	0,302	0,549	0,818	0,884	0,968	1,330	1,601	2,593
8	-1,032	-0,611	-0,386	-0,242	-0,181	-0,127	-0,009	0,132	0,406
9	1,032	0,611	0,386	0,242	0,181	0,127	0,009	-0,132	-0,406
10	8,932	6,478	6,301	5,826	5,753	5,262	4,413	3,275	2,364
11	4,928	6,117	6,856	7,154	7,057	7,209	7,452	7,759	7,775
12	-0,215	0,687	1,236	1,533	1,804	2,039	2,406	3,201	3,547
13	-0,999	0,449	1,143	1,881	1,953	2,018	2,574	3,203	3,918
14	-3,663	-3,620	-3,716	-3,734	-3,728	-3,723	-3,570	-3,461	-2,756
15	8,730	7,198	6,008	5,609	5,417	5,160	5,021	3,910	1,849
16	5,133	6,090	6,083	6,425	6,450	6,458	6,983	7,272	7,952

Table 4.6. Correction factors obtained after rotating segmentation mask of a fix angle (+ refers to counterclockwise rotation, - refers to clockwise rotation)

T2* (ms) – POST CORRECTION									
Seg	**20°**	**10°**	**5°**	**2°**	**0°**	**-2°**	**-5°**	**-10°**	**-20°**
1	19,689	19,990	20,391	20,584	20,794	20,930	21,226	21,618	22,747
2	20,135	20,060	20,028	20,052	20,043	20,054	20,083	20,061	20,086
3	20,545	20,240	20,131	20,098	20,084	20,149	20,205	20,141	20,304
4	30,588	25,914	24,857	23,928	23,220	22,901	22,513	21,768	20,994
5	25,062	27,158	27,880	28,863	28,973	28,910	28,950	28,311	29,512
6	20,173	20,532	20,768	20,976	21,202	21,440	21,654	22,052	23,310
7	19,905	20,122	20,222	20,333	20,360	20,395	20,547	20,662	21,094
8	19,596	19,759	19,847	19,904	19,928	19,949	19,997	20,053	20,164
9	20,421	20,247	20,155	20,097	20,073	20,051	20,003	19,947	19,839
10	24,350	22,977	22,884	22,638	22,601	22,353	21,936	21,402	20,992
11	22,187	22,788	23,178	23,339	23,287	23,369	23,503	23,674	23,682
12	19,914	20,279	20,507	20,633	20,749	20,850	21,011	21,368	21,527
13	19,608	20,181	20,468	20,782	20,813	20,841	21,086	21,369	21,700
14	18,635	18,650	18,616	18,610	18,612	18,614	18,667	18,705	18,955
15	24,231	23,363	22,731	22,527	22,430	22,302	22,232	21,697	20,768
16	22,288	22,774	22,770	22,949	22,962	22,966	23,247	23,404	23,782

Table 4.7. Post-correction T2* values (using correction factors obtained in table 4.6)

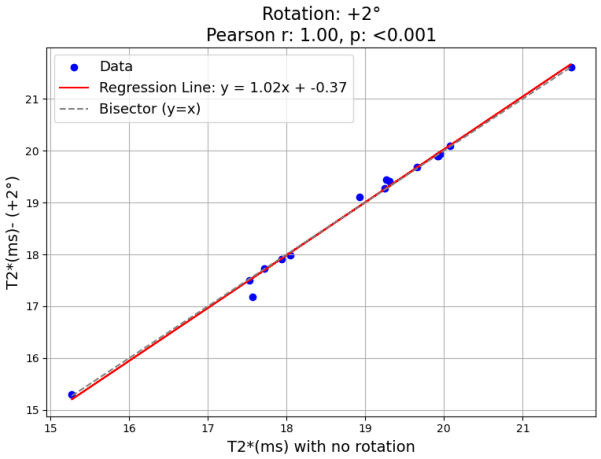
Rotation: +2°
Pearson r: 1.00, p: <0.001
Data
Regression Line: y = 1.02x + -0.37
Bisector (y=x)
T2*(ms)- (+2°)
T2*(ms) with no rotation

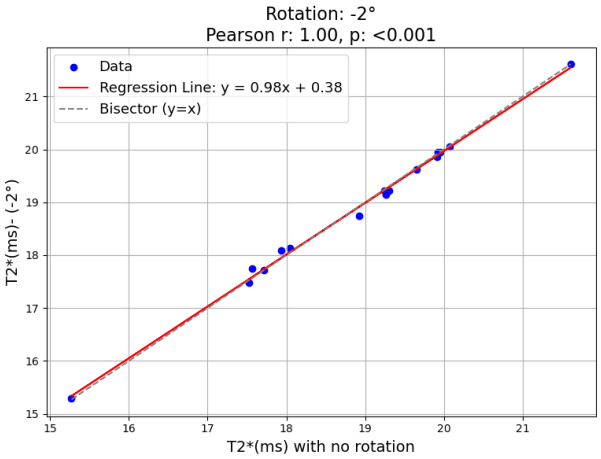
Rotation: -2°
Pearson r: 1.00, p: <0.001
Data
Regression Line: y = 0.98x + 0.38
Bisector (y=x)
T2*(ms)- (-2°)
T2*(ms) with no rotation

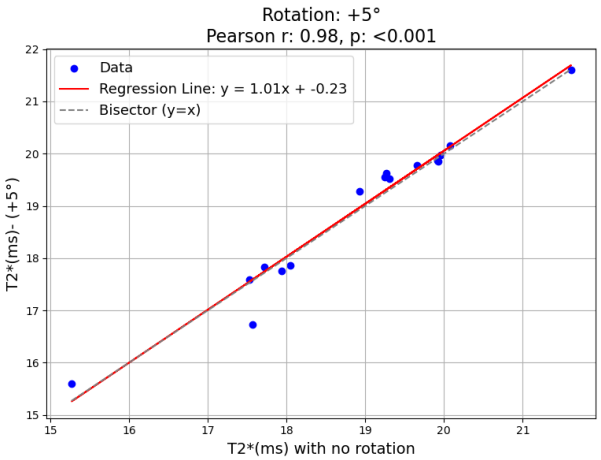
Rotation: +5°
Pearson r: 0.98, p: <0.001
Data
Regression Line: y = 1.01x + -0.23
Bisector (y=x)
T2*(ms)- (+5°)
T2*(ms) with no rotation

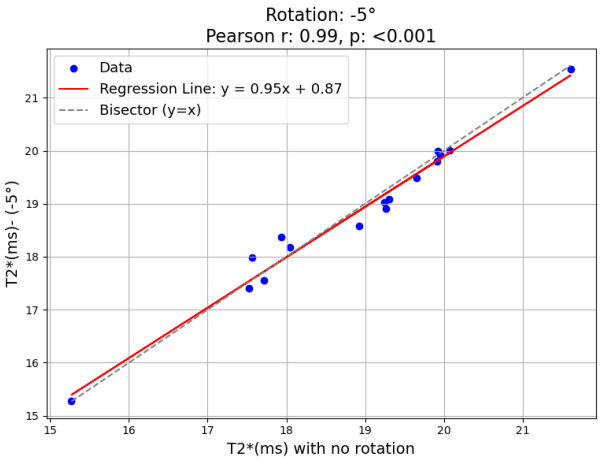
Rotation: -5°
Pearson r: 0.99, p: <0.001
Data
Regression Line: y = 0.95x + 0.87
Bisector (y=x)
T2*(ms)- (-5°)
T2*(ms) with no rotation

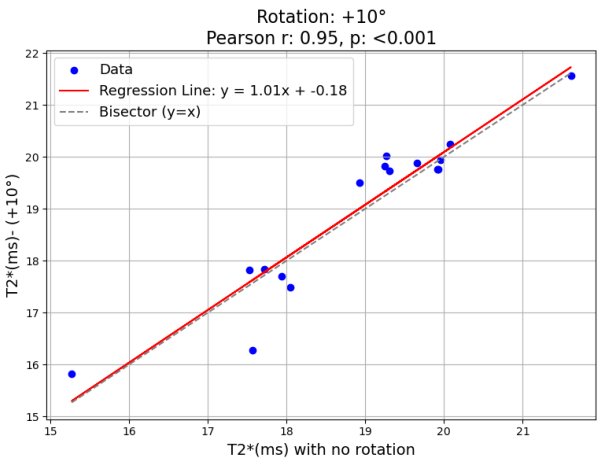
Rotation: +10°
Pearson r: 0.95, p: <0.001
Data
Regression Line: y = 1.01x + -0.18
Bisector (y=x)
T2*(ms)- (+10°)
T2*(ms) with no rotation

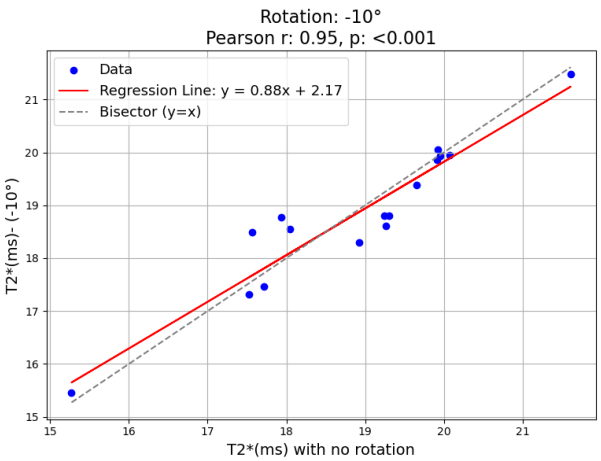
Rotation: -10°
Pearson r: 0.95, p: <0.001
Data
Regression Line: y = 0.88x + 2.17
Bisector (y=x)
T2*(ms)- (-10°)
T2*(ms) with no rotation

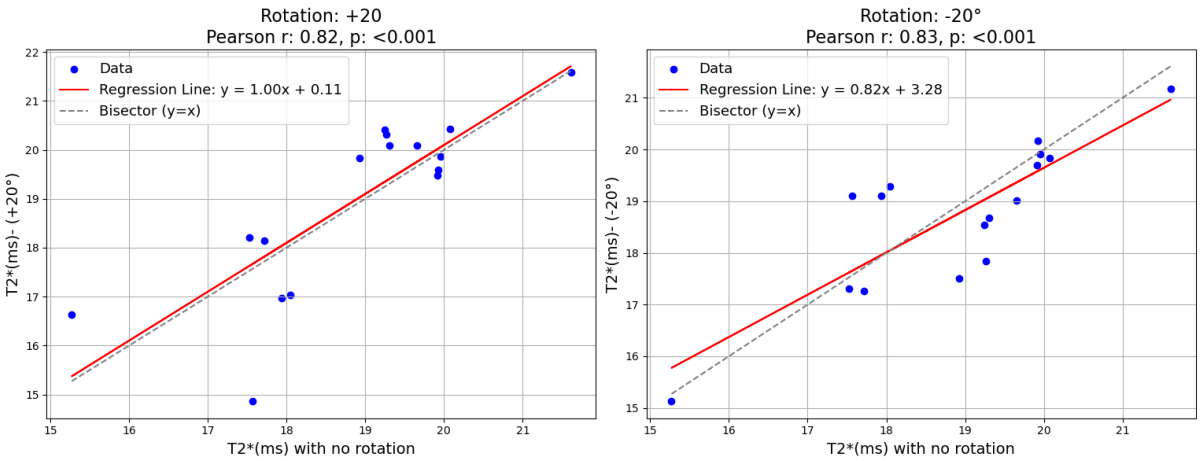

Figure 4.49. Pearson Correlation between T2* values corrected with original factors and T2* values corrected with different angles (in each row a different couple of angles is shown)

4.9.5 Correction Factors obtained through Random Mask Segmentation Rotations

In this section we examine how correction factors behave in the presence of random errors. A simulation with a uniform probability for each angle (only the integer values in this range were considered) in a range of ±10 degrees was selected for this simulation. Specifically, each slice of each subject was randomly rotated by an amount within this range. A total of 50 independent simulations were performed. The mean and standard deviation of the calculated factors across all the fifty simulations are plotted against true correction factors (obtained considering mean T2* values of all healthy subjects in pixel-wise approach) in Figure 4.50. The resulting correction factors from these simulations are presented in the final appendix, together with T2* corrected segments (always considering a T2* initial value equals to 20 ms in each segment). The mean and standard deviation calculated in each segment (so selecting the entire row) across all the fifty simulations in both correction factors and T2* values are in illustrated in Table 4.8. To improve the meaning of this values, means and standard deviations are illustrated in Figure 4.51.

SEG	Correction Factors (Hz)	Correction Factors (Hz)		T2* corrected (ms)	
		Mean	SD	Mean	SD
1	1,908	1,800	0,313	20,748	0,135
2	0,107	0,116	0,162	20,047	0,065
3	0,209	0,373	0,285	20,151	0,116
4	6,934	7,782	0,678	23,692	0,379
5	15,485	14,597	0,509	28,252	0,406
6	2,835	2,870	0,283	21,219	0,128
7	0,884	0,946	0,191	20,386	0,080
8	-0,181	-0,176	0,084	19,930	0,033
9	0,181	0,176	0,084	20,071	0,034
10	5,753	5,095	0,503	22,272	0,248
11	7,057	7,111	0,293	23,317	0,159
12	1,804	1,758	0,272	20,729	0,117
13	1,953	1,842	0,277	20,766	0,120
14	-3,728	-3,650	0,160	18,640	0,055
15	5,417	5,533	0,330	22,490	0,167
16	6,450	6,476	0,186	22,976	0,098

Table 4.8. Mean and Standard deviation obtained in each segment across 50 random simulations in Correction Factors results and T2* corrected results.

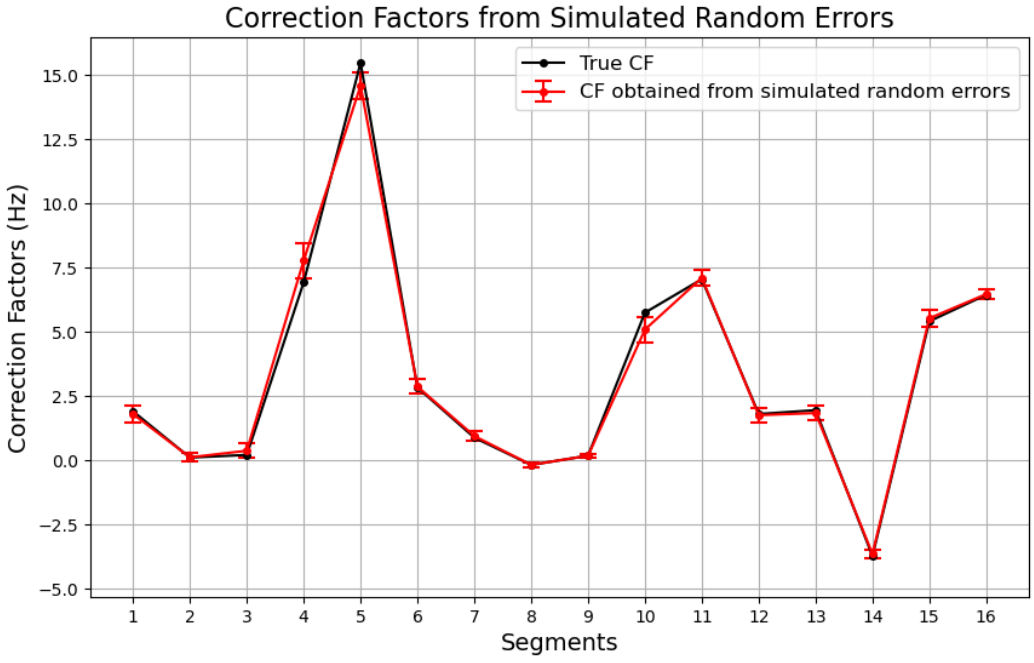

Figure 4.50. Mean and Standard deviation obtained in each segment across 50 random simulations in correction factors (second and third columns of Table 4.8) against true correction factors (first column)

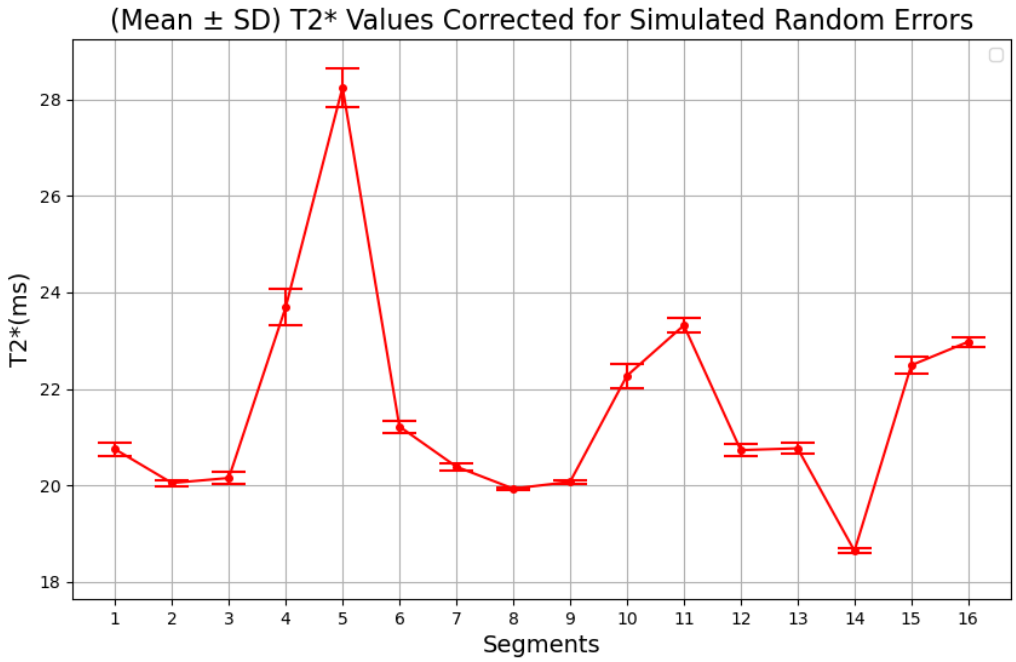

Figure 4.51. Mean and Standard deviation obtained in each segment across 50 random simulations in T2* corrected results (fourth and fifth columns of Table 4.8)

4.10 Improved Segmentation

4.10.1 Segmentation Output

A new kind of segmentation was carried out to improve the selection of the inter-ventricular septum. Figure 4.52 compares the results of the previous segmentation method—where the septum was divided into four or six uniform and equidistant parts—with those of the new approach. In the updated segmentation, segments 2 and 3 (depicted in green and blue, respectively) now span the entire length of the septum. By contrast, in the earlier method, segment 3 is noticeably too short, and segment 4 improperly includes regions of the septum that should instead be confined to the areas maintaining contact with the diaphragm. Similarly, this refined segmentation was applied to the apical region. Here, segment 14 is now designated to encompass the entire septum, addressing the limitations of the prior segmentation. This adjustment is illustrated in Figure 4.53. A comparison between T2* mean values previously obtained in standard segmentation and T2* mean values with this proposed segmentation are illustrated in Figure 4.54 (pixel-wise approach) and Figure 4.55 (ROI-based approach).

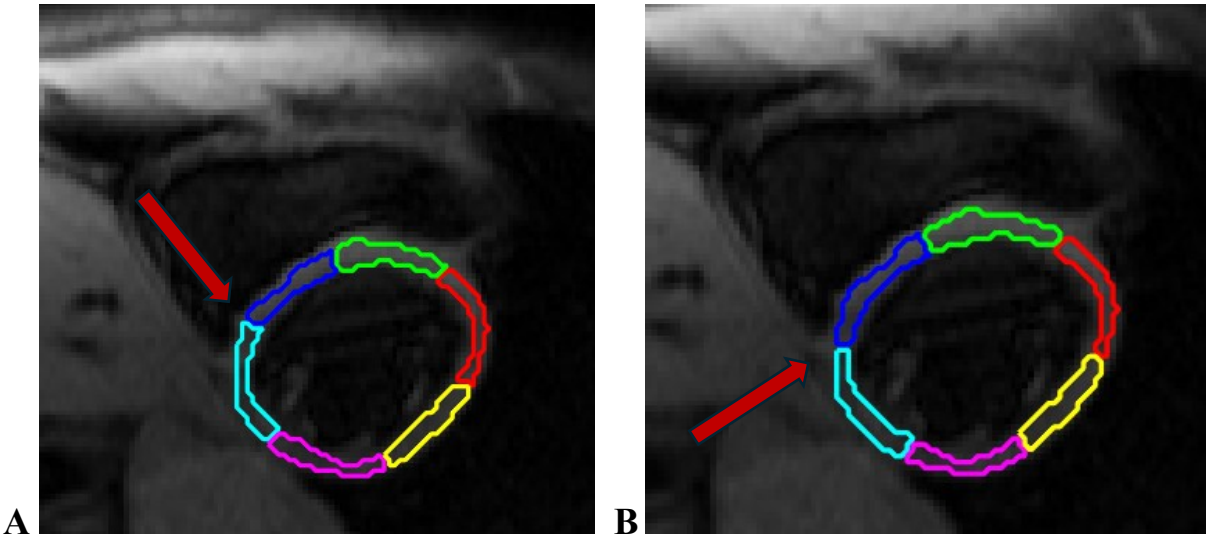

Figure 4.52. Left ventricular in basal slice. Segmentation of the myocardium in equal parts (A). Segmentation of the myocardium adapted to the inter-ventricular septum (B).

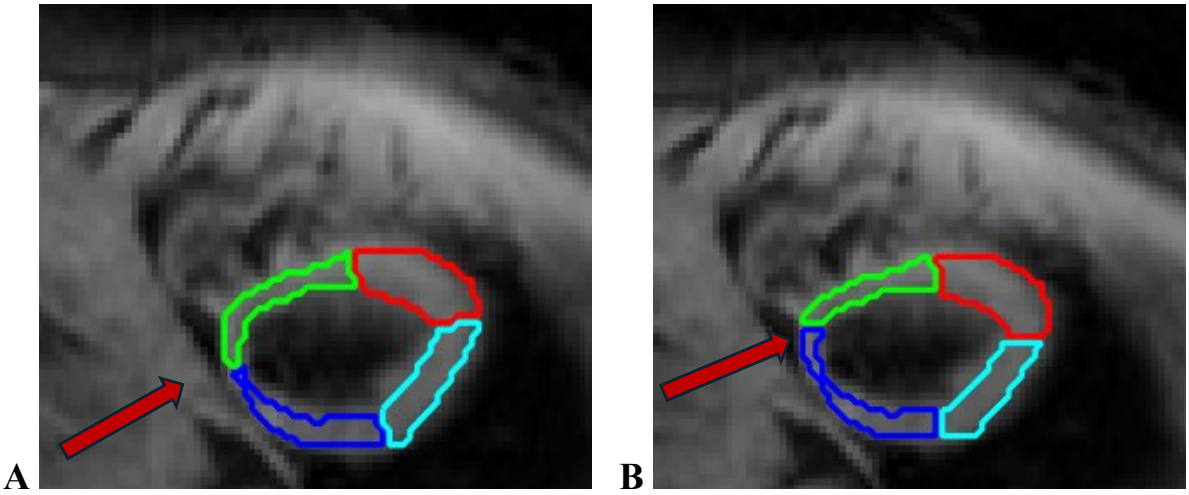

Figure 4.53. Left ventricular in apical slice. Segmentation of the myocardium in equal parts (A). Segmentation of the myocardium adapted to the inter-ventricular septum (B).

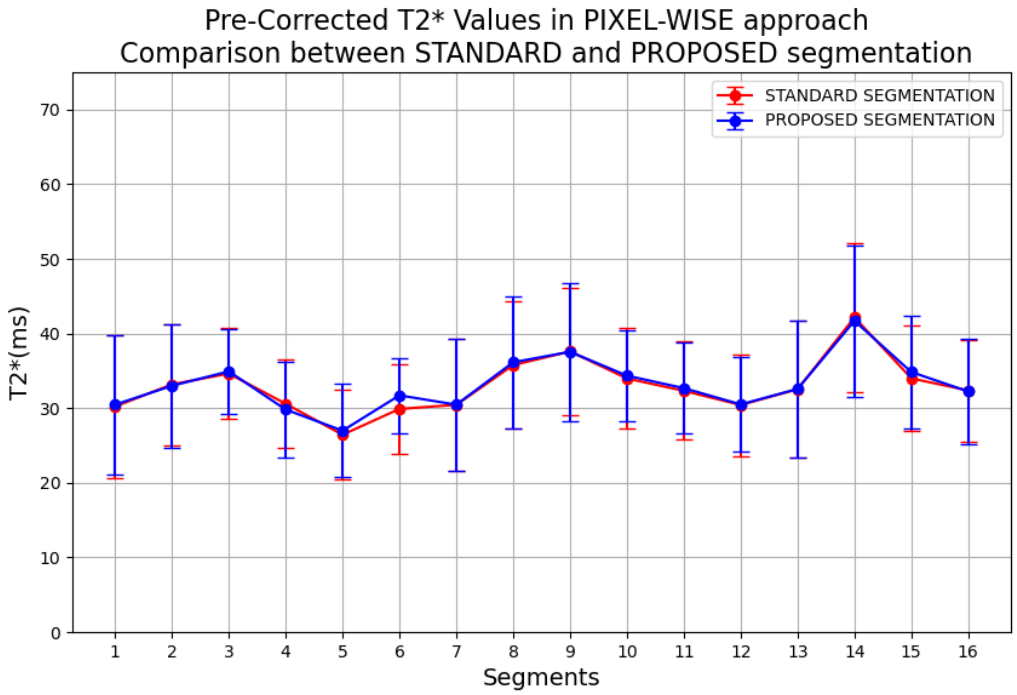

Figure 4.54. Comparison between T2* values obtained in patients with STANDARD segmentation and with the PROPOSED segmentation in pixel-wise approach

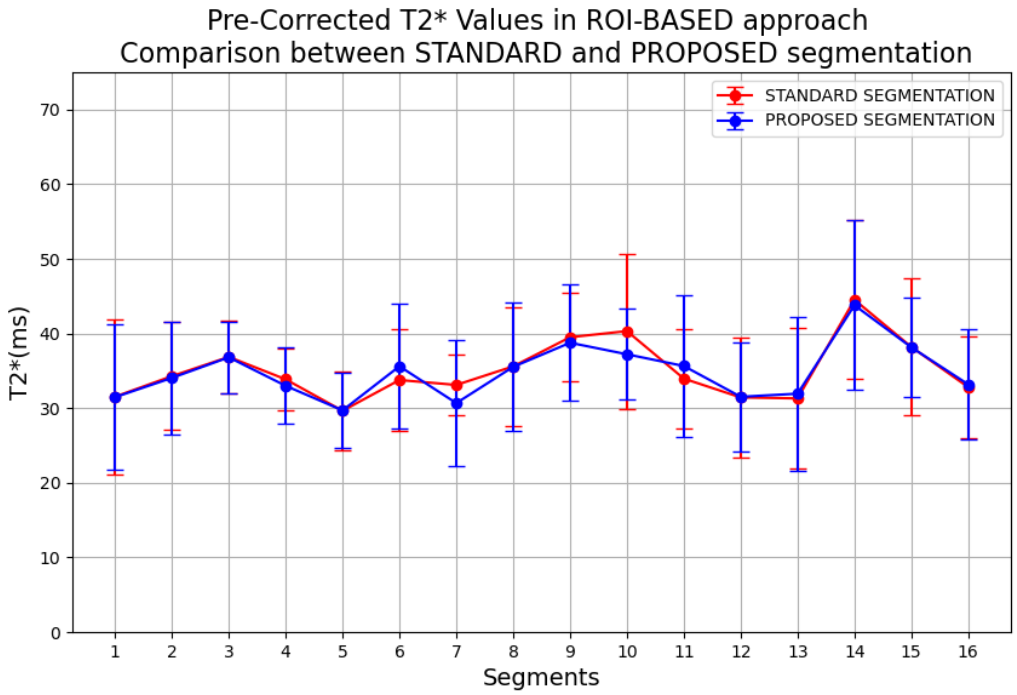

Figure 4.55. Comparison between T2* values obtained in patients with STANDARD segmentation and with the PROPOSED segmentation in ROI-based approach

4.10.2 Correction Factors with anatomical corrected segmentation

The relevant thing is to investigate how the proposed segmentation that respect anatomical landmarks impacts the correction factors previous calculated. Both pixel-wise technique and ROI-based technique were applied to the new proposed segmentation, and new R2* correction map were calculated and compared to the previous results (Table 4.9). The same Dataset of Healthy subjects were used to calculate all these factors. Then we applied both R2* correction maps to T2* mean values obtained in patients through S-EXP model, to see the effect of the correction (explained in paragraph 3.9.2). The correlation outcomes are then shown in the Figures 4.56 and 4.58. In Table 4.9, the largest differences between column 1 and column 2, as well as between column 3 and column 4, are observed in segments 4 and 5. To highlight these segments in the correlation plots, a distinct colour has been used, allowing for easy identification and tracking of their behaviour across the comparisons. Moreover, Figure 4.57 and Figure 4.59 show the comparison between T2* corrected values obtained in standard segmentation and in the proposed segmentation.

SEG	PIXEL-WISE		ROI-BASED	
	CF (standard segmentation)	CF (new segmentation	CF(standard segmentation	CF (new segmentation
1	1,908179	1,787496	0,943966	0,889041
2	0,10679	0,252709	-0,56995	-0,26103
3	0,208711	0,801517	-0,47067	-0,00338
4	6,933942	13,34576	3,488332	7,649924
5	15,48488	12,10384	14,06024	11,43992
6	2,835165	2,406567	2,344565	2,060075
7	0,884143	1,125548	1,307123	1,628278
8	-0,18081	-0,13422	0,168179	0,111123
9	0,180807	0,13422	-0,16818	-0,11112
10	5,75329	6,038604	2,448872	3,030252
11	7,057396	7,029636	6,730466	6,446456
12	1,804048	1,506919	2,104523	1,869373
13	1,952612	1,760725	2,784862	3,021231
14	-3,72808	-4,09449	-3,86611	-4,11813
15	5,416756	6,84749	4,579532	4,885949
16	6,449772	6,695516	6,983734	7,210148

Table 4.9. R2* (Hz) Correction Map in standard Segmentation and new Segmentation

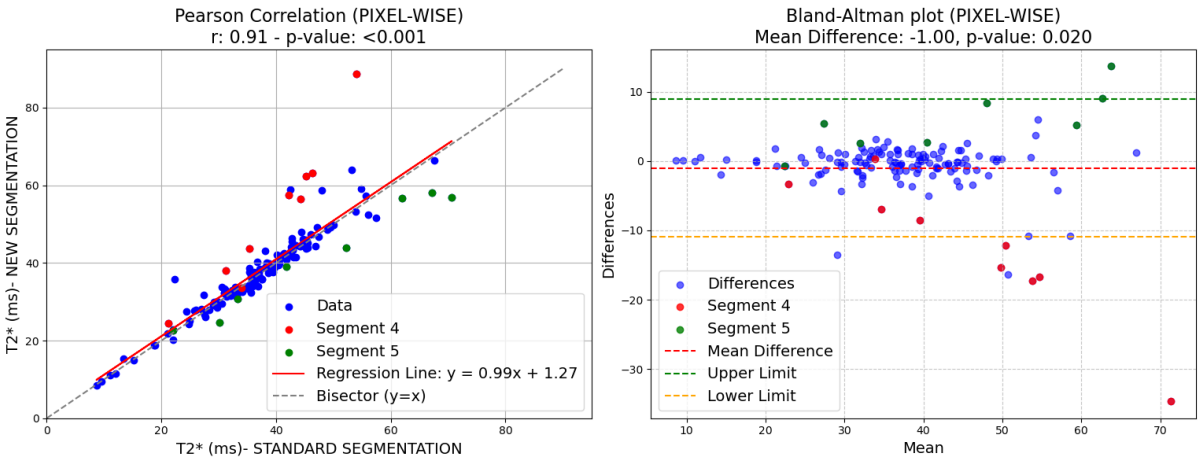

Figure 4.56. Pearson Correlation and Bland-Altman Plot between T2* corrected values in standard segmentation and T2* corrected values in new segmentation, both with pixel-wise approach

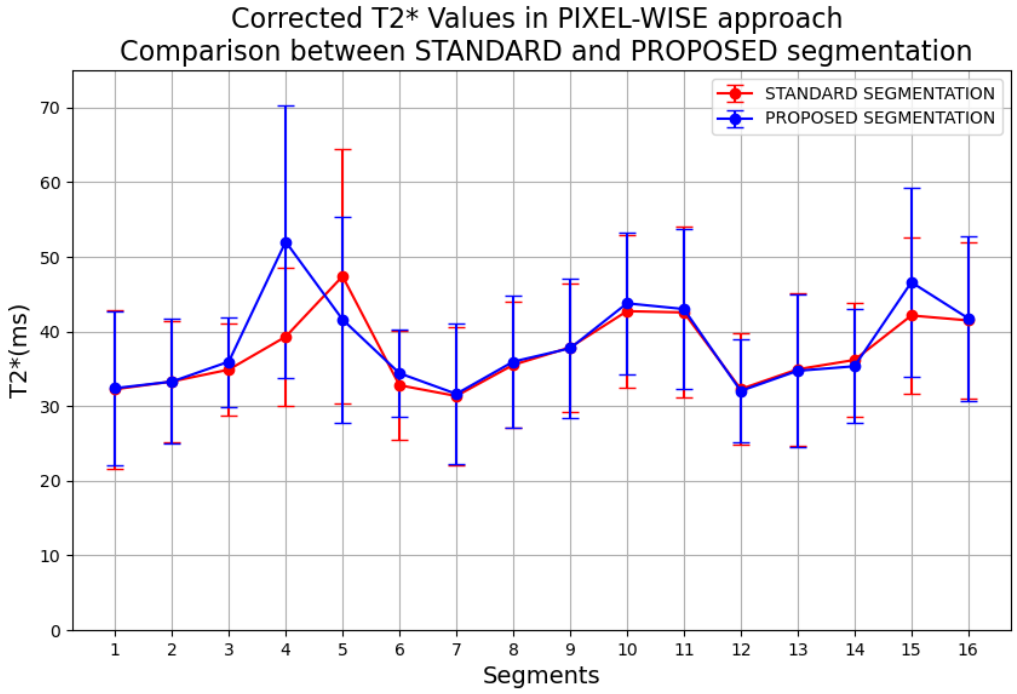

Figure 4.57. Comparison between T2* CORRECTED values obtained in patients with STANDARD segmentation and with the PROPOSED segmentation in ROI-based approach

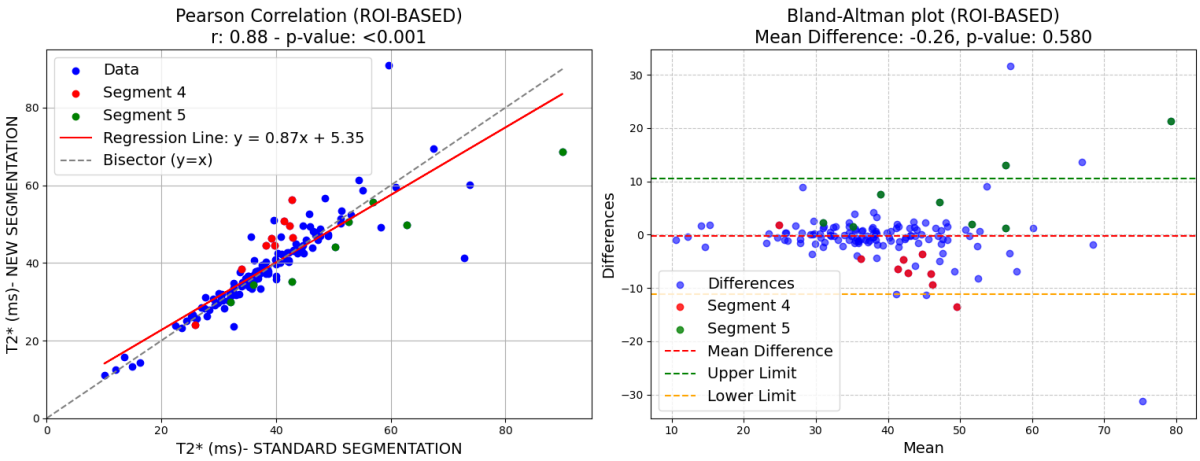

Figure 4.58. Pearson Correlation and Bland-Altman Plot between T2* corrected values in standard segmentation and T2* corrected values in new segmentation, both with ROI-based approach

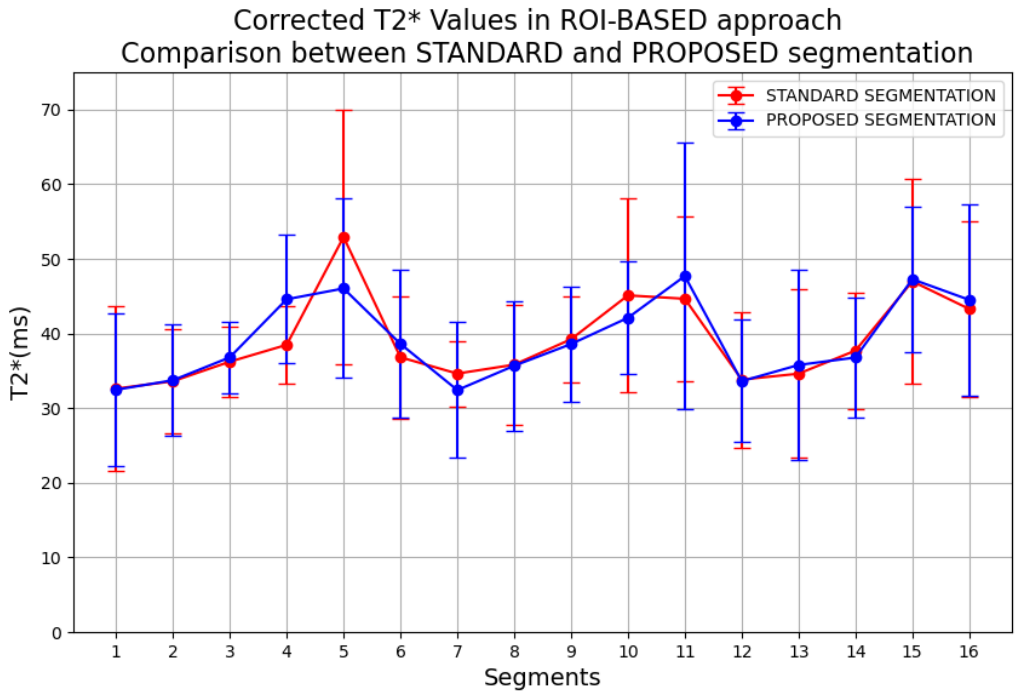

Figure 4.59. Comparison between T2* CORRECTED values obtained in patients with STANDARD segmentation and with the PROPOSED segmentation in ROI-based approach

In addition, Figures from 4.60 to 4.63 show the global trend across pre-corrected T2* and post-corrected T2* segments in patients, to underline how the correction modifies the estimates. This

comparison was carried out in both kinds of segmentations and in both approaches (pixel-wise and ROI-based), for a total of 4 plots.

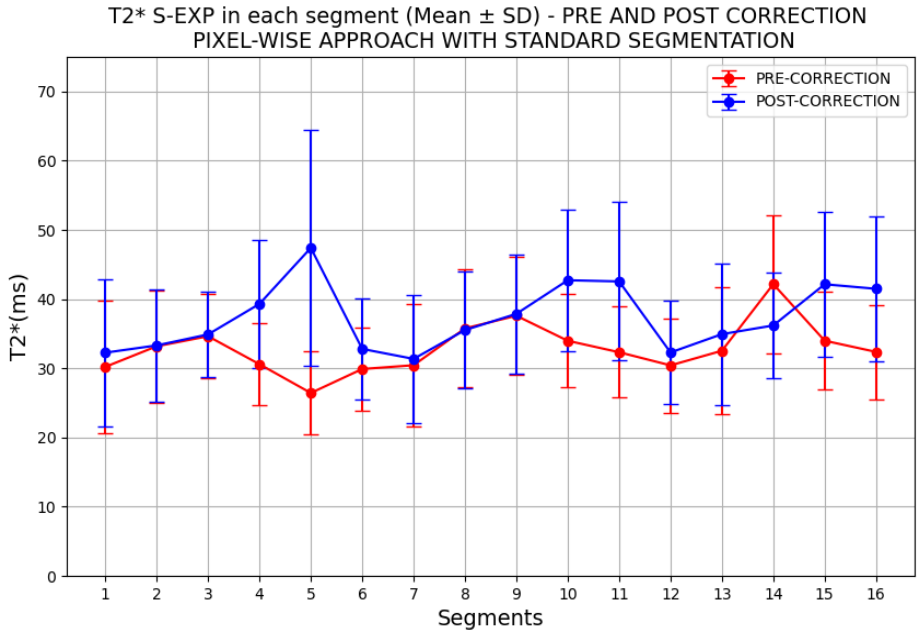

Figure 4.60. Effect of the correction on T2* segments in patients with STANDARD segmentation and using pixel-wise approach

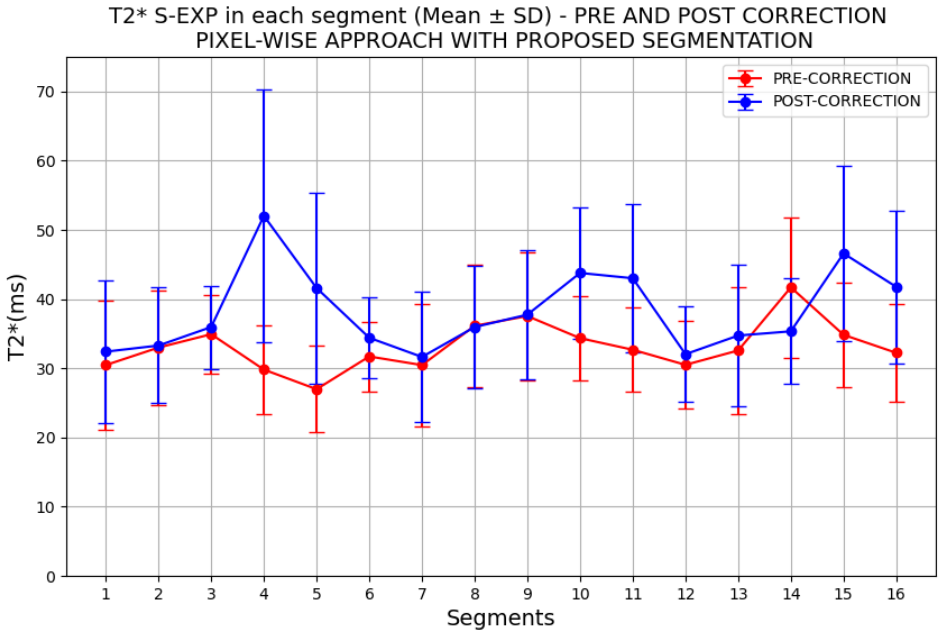

Figure 4.61. Effect of the correction on T2* segments in patients with NEW segmentation and using pixel-wise approach

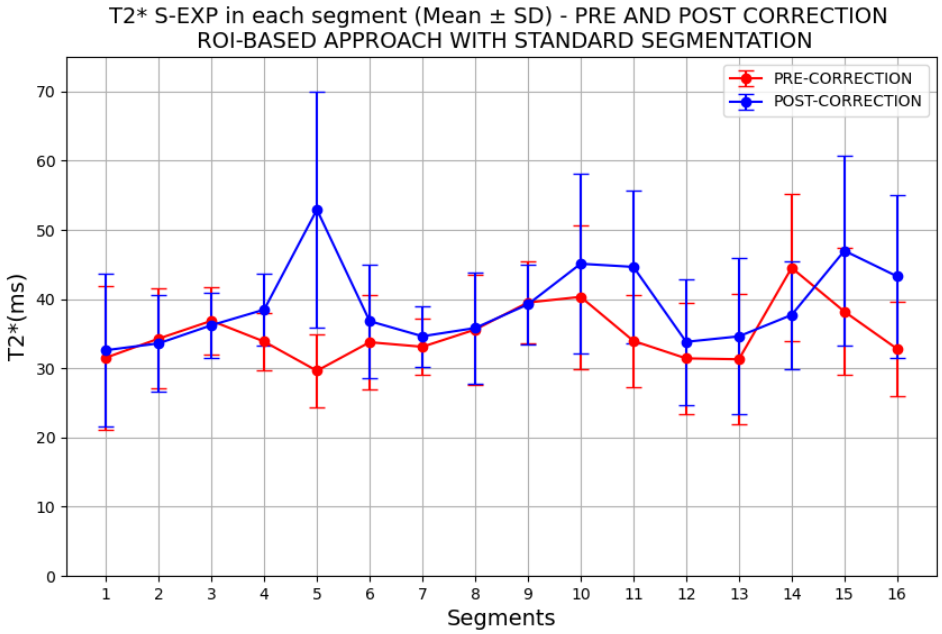

Figure 4.62. Effect of the correction on T2* segments in patients with STANDARD segmentation and using ROI-based approach

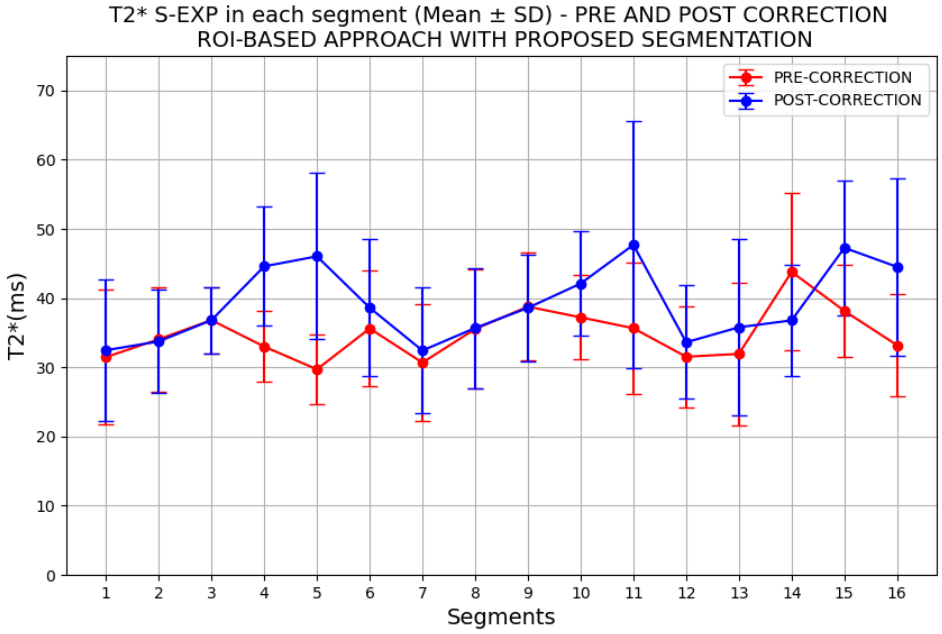

Figure 4.63. Effect of the correction on T2* segments in patients with our PROPOSED segmentation and using ROI-based approach

CHAPTER 5 – DISCUSSION

5.1 Comparison between models

This first section concerns the analysis of model results to compare T2* estimations obtained by S-EXP, LIN, C-EXP models in pixel-wise approach or in ROI-based approach, evaluating also their smoothing effect. The first consideration regards T2* maps obtained using pixel-wise approach. With this technique, we can exploit parametric mapping to estimate a T2* value in each voxel of the image. All the reported maps (Figure 4.2 and 4.6) appear similar and delineate the myocardial structure, but we see some differences in images where smoothing operation was applied. In these last ones, the anatomical structures are less defined and there is a loss of details. This happens because smoothing combines signals from multiple tissue types within a voxel's neighbourhood, leading to an amplification of the partial volume effect. In addition, at the boundaries between tissues or regions with different T2* values, smoothing blends pixel intensities, so that the contour of endocardium and epicardium is less defined and the contrast between adjacent regions is lower. Despite lower resolution, smoothing effect can lead to a noise reduction, increasing signal-to-noise ratio (SNR) [58] . It is therefore necessary to find a trade-off between all these considerations. By a visual inspection of all the plots (Figure 4.3 and Figure 4.7) presented in the previous chapter, we can observe that smoothing operation does not impact T2* estimation, since the mean values obtained averaging T2* of all subjects in each myocardial segment are comparable and their minimal differences do not compromise a diagnosis. Furthermore, this consideration is valid for all the models and for both Datasets. However, the Student T-test reveals a significant difference in 14 over 16 segments (S-EXP, C-EXP, and LIN) in healthy subjects. In contrast, a smaller quantity of segments (3 over 16) shows significant differences in patients. This is likely attributed to the larger sample size of healthy subjects (n=49) compared to patients (n=9), which increases the statistical power in the former group. Since in performing smoothing we englobe also pixels outside the myocardium region, for examples ventricular cavities and blood (whose T2* value is higher than myocardial T2*), it is not worth to implement this technique. Considering these results, we conclude that smoothing effect does not improve T2* estimation, and so in the following analysis only models which do not perform smoothing will be considered.

From a visual inspection of T2* maps, we can see that LIN and S-EXP models lead to very similar results. This is confirmed by Figure 4.4 (Healthy subjects) and Figure 4.8 (patients), where (mean ± SD) T2* values in each segment considering all subjects are represented. We can see that the overall trend is the same: the infero-lateral segment (number 5) of the basal

slice shows the lowest T2* value, while the highest T2* value is in the septal segment (number 14) of the apical region. The reason why the results of the S-EXP model and the LIN model show comparable results is due to the structure of the linearized model. The mathematical equation describing the exponential decay in these two models is the same, the only difference is the application of the logarithm in the linear model. However, a significant difference is introduced using the C-EXP model. As can be seen, the presence of the additive constant leads to an underestimation of T2* values, although enables a good fitting of the decay curve. This result is also confirmed by several studies available in the literature [40] [42].The additive constant of the model accounts for residual noise and artifacts and avoids attributing it to signal decay [42], [43] . In other terms, it ensures that long-time data points, where signal approaches the noise floor, are not misinterpreted as part of the decay curve. As described in paragraph 2.1, the truncation model offers an alternative to offset correction. However, given the constraints outlined, this method was not implemented in this work. Another alternative to the offset model is the bi-exponential model, in which the second exponential term replaces the constant. The a priori identifiability of a two exponential model can be done only if the two term ($T2_1$* and $T2_2$*) are unequal and if the noise in the data is sufficient to permit the numerical estimation of both components. In our case, it is possible to observe that, in each myocardial voxel, the estimation of the first T2* component (which describes the faster decay) and of the second T2* component (which describes the slower decay) provide the same outcomes. Therefore, we conclude that in the myocardial tissue the signal decay cannot be distinguished in more than a single exponential. Therefore, since the bi-exponential model is more complex, has a greater number of degrees of freedom and does not provide additional information, it is discarded from the subsequent analysis. Although this model is not useful for assessing myocardial iron, it has shown very good results for estimating T2* in the liver exploiting phase data in the fit using a weighted least square approach [59] .

To evaluate which of the tested models performs better, the Bayesian Information Criterion was applied in all Datasets. Histograms in Figures (from 4.10 to 4.12 in healthy subjects, and from 4.15 to 4.17 in patients) reveal that mono-exponential model is the most suitable to estimate T2* in myocardial tissue, confirming the results available in literature [40] [42]. Taigang et al. have conducted an in vivo study and an ex-vivo study to investigate which is the optimal method to quantify myocardial iron overload. In both these studies, the outcome is the same: MR signals can be well fitted by a mono-exponential model, and this is the approach that estimates T2* most accurately. Their results also suggest that the T2* decay curve in a heavily iron-overload heart is mono-exponential in essence. However, patients with severe iron overload were not

analysed in our work, and it is therefore not possible to demonstrate this outcome in this clinical context. Despite the high prevalence rates of the S-EXP model, there is a small percentage of voxels in which C-EXP model turns out to be better. Since the Bayesian Information Criterion aims to make a trade-off between model complexity (in terms of number of parameters) and fitting performance, when the residuals obtained are equal (so both models fit the data in the same way), the BIC index selects the S-EXP model as the best, since it presents only two parameters. In other situations, it is important to evaluate the original signal trend investigating the physiological context and the presence of noise or artifacts. In voxels with low SNR, the final points of the decay curve may be dominated by noise, and this can induce an improved fit by C-EXP model, thanks to the presence of the additive constant. Besides, cardiac and respiratory motion could distort signal intensities in some specific voxels. So, we know from literature that C-EXP model performs better than S-EXP model for low T2* values (< 25 ms) [39]. In this case, we are not in presence of a fast decay signal, which occurs when T2* relaxation times are very short, as frequently seen in liver tissue. This usually leads to a rapid drop in signal intensity within the initial few data points of the acquisition.

Another interesting point is the absence of the linear model in BIC results, which never gives the best fit. However, this does not imply that the model performs poorly. Since the number of parameters is the same, the calculated BIC index only depends on the result of the residuals sum of squares. In fact, the residuals appear to be slightly higher, and this leads to a higher BIC. Nevertheless, many researchers still employ the linear model because it is simpler and easily accessible. However, since the relationship between measured signal intensities and echo times is never truly linear, a nonlinear approach is suitable. In addition, the logarithmic form risks to modify the error distribution, invalidating the initial assumptions supporting the use of linear regression [42] . This enforces the choice of using mono-exponential model.

To examine the behaviour of voxels where the C-EXP model shows better performance, the colour maps in Figure 4.13 (healthy subjects) and Figure 4.18 (patients) highlight whether these voxels are associated with specific subjects or are evenly distributed across the population. In general, voxels favouring the C-EXP model are evenly distributed across subjects, although there are some exceptions. We see that there is a higher prevalence in two subjects from Dataset 1 and in one subject from Dataset 2. A common feature of the identified segments (specifically segment 7 of subject 23 and segment 16 of subject 38 in healthy subjects, and segment 6 of subject 6 in patients) is a significant discrepancy in T2* estimation between the C-EXP and LIN/S-EXP models: the T2* values derived from the C-EXP model are significantly reduced

in these cases. Although these observations require further investigation, additional analyses were performed to better understand the performance of the C-EXP model. Specifically, the threshold set for the coefficient of variation (CV) associated with T2* estimation was reduced from 1000% to 10% for both the pixel-wise approach and the ROI-based approach. This step is critical to exclude voxels or segments where T2* estimation is unreliable. The results showed that with the C-EXP model, almost 100% of voxels (in pixel-wise approach) or segments (in ROI-based) are discarded in both datasets. This result highlights that T2* estimates derived using the C-EXP model are not sufficiently accurate. Consequently, this model was excluded from all subsequent analyses. In conclusion, we found that the mono-exponential model provided the most reliable T2* estimates and therefore only this model was considered in the remaining analysis.

After identifying the most appropriate model and establishing the threshold for the coefficients of variation to determine which T2* values should be considered, it becomes insightful to compare the two different methodologies employed: the pixel-wise approach and the ROI-based approach. In the pixel-wise technique, a T2* value is estimated for each voxel individually. These voxel-wise T2* values are then averaged to compute a mean T2* value for each segment, as usually represented in the Bull's eye. On the other side, in the ROI-based method, the signal from all voxels within a single segment is first averaged, and a single T2* value is estimated for the entire segment. Both approaches aim to calculate T2* values for each of the sixteen segments. We applied and compared these techniques in both datasets to investigate potential differences in T2* estimation. As shown in Figures 4.30 (healthy subjects) and 4.32 (patients), the mean T2* values across all segments and subjects obtained using both methods assume the same trend. This is confirmed also by Pearson correlation ($r= 0.91$ in healthy subjects and $r= 0.84$ in patients). Since both approaches yield reliable results, they were deemed suitable for subsequent analyses. This conclusion aligns with findings from previous studies, which confirm that ROI-based analyses are as accurate as pixel-wise mapping methods [60]. Nevertheless, each method shows some pros and cons. The pixel-wise method provides a more detailed spatial representation, potentially capturing localized variations in T2* values. However, it is computationally intensive and more susceptible to noise. On the other hand, the ROI-based approach is faster and simpler, although it may lose some spatial resolution. Another important consideration concerns the application of the coefficient of variation (CV) threshold. We saw that, in both approaches, a CV value is determined for each estimation. Voxels with high CV values, indicative of unreliable estimates, can be selectively excluded while retaining the remaining data. In contrast, the ROI-based approach provides a single CV value for the

entire segment. If this CV exceeds the threshold, the entire segment is excluded from the analysis. This difference has practical implications. While both methods aim to ensure the reliability of the estimates, the ROI-based approach may result in excessive data loss. By discarding entire segments, critical diagnostic information can be missed. For instance, in regions with significant iron overload, the exclusion of an entire segment could prevent the detection of clinically relevant findings. Thus, while the ROI-based method simplifies the process, its limitations in preserving diagnostically valuable data must be carefully considered, particularly in scenarios where localized variations are critical for interpretation. Therefore, although the ROI-based S-EXP model gives results comparable to the pixel-wise approach, the pixel-wise approach might be suggested. Pixel-wise approach allows to selectively exclude unreliable or no-signal voxels, ensuring more accurate analysis. This result is confirmed from the outcome obtained by the test-retest applied in patients. We can see that T2* estimates obtained from the first acquisition and from the second acquisition show a stronger correlation using pixel-wise approach (r=0.91 in pixel-wise approach and r=0.89 in ROI-based approach).

5.2 Correlation between T2* values

In this study, two Datasets were provided to compare T2* estimates in both healthy subjects and Patients affected by Haemochromatosis or Thalassemia Major. First, it is interesting to investigate whether a correlation caused by anatomical analogy exists between the three slices by analysing each dataset separately. In healthy subjects, a similar pattern of mean T2* values is observed in both the basal and mid-ventricular slices. A slight gradual increase in T2* is observable across the first three segments (anterior, antero-septal, and infero-septal segments). Following this, the T2* values show a decreasing trend, reaching a negative peak in the infero-lateral segment, especially in segment 5 of the basal slice. This pronounced decrease in T2* in segment 5 is due to the presence of the posterior cardiac vein, which affects signal behaviour in this region [39] .In contrast, the apical region demonstrates a distinct pattern due to differences in segmental division. Specifically, a positive peak in T2* is observed in segment 14 (the septal segment), highlighting the main characteristic of the apical slice compared to the basal and mid-ventricular regions. In patients, the basal and mid-ventricular slices also share common features, but the pattern differs from that observed in healthy subjects. A positive peak appears in the infero-septal segments (segments 3 and 9). The negative peak persists in the infero-lateral segment of the basal slice (segment 5) and a positive peak is again observed in the septal segment (number 14), mirroring the behaviour observed in healthy subjects. We also

compared the overall trend across the sixteen cardiac segments, to verify if a common pattern is present between healthy subjects and patients. Figures 4.27 and 4.28 illustrate these trends for both groups using the pixel-wise and ROI-based approaches. Interestingly, the overall patterns are consistent between healthy subjects and patients, but some segments show higher T2* values in patients compared to healthy individuals. This observation contrasts with the expected outcome, where patients would generally have lower T2* values due to iron overload. However, this discrepancy can be attributed to the fact that the patients included in the study have been undergoing iron chelation therapy. Such treatment effectively reduces iron deposition, leading to T2* values that remain above the clinical threshold of 20 ms, conventionally used to identify iron overload. Within this context, chelation therapy, particularly when combined with complementary treatments, has demonstrated significant success in reducing iron levels and mitigating its toxic effects. Beyond iron removal, chelating agents may also provide protection against iron toxicity by inhibiting the catalytic formation of reactive oxygen species, such as free radicals[61] . Further considerations concern the conventional choose of T2* threshold, which plays a critical role in the early detection of iron overload. Below a myocardial T2* of 20 ms, there is a progressive and significant decline in left ventricular ejection fraction and an increase in the left ventricular end-systolic volume index and left ventricular mass index, proving that iron overload conduces to sever myocardial disfunctions [62]. In thalassemia, there is unequivocal evidence showing that iron causes the left ventricular disfunction, because severe siderosis is present in patients with heart failure, but this condition is reversible with an effective chelation therapy [63]. In any case, iron exits in two forms: non-transferrin bound iron (NTBI) and bound iron (BI). The toxicity of NTBI is much higher than BI. Therefore, since iron accumulates in the normal storage form in the heart, T2* falls but there is little effect on cardiac function until a threshold is reached where the iron storage capacity is exhausted. Once NTBI appears, cardiac function rapidly deteriorates. This explains why the relation between T2* and cardiac function is shallow until a critical level is reached, after this level severe damage occurs. So, the identification of abnormal LV function is a late sign of iron toxicity [23]. So, further investigations are necessary to refine the current T2* cutoff and enhance its sensitivity for detecting early iron deposition.

After these considerations, we can evaluate the correlations obtained from the T2* estimates between the single-exponential model and the HIPPO software. In pixel-wise technique not only mean T2* values were considered, but also median value in each segment, since median is less sensitive to outliers. Although the standard convention is to use the mean value, other studies have also considered the T2* value per segment obtained from the median [64]. In both

healthy subjects and patients, the Pearson correlation coefficient indicates a positive correlation between the results obtained by the S-EXP model and HIPPO, especially when using the ROI-based approach, as this is the method used by the HIPPO software. From Table 4.1, we see that there are no significant differences in the correlation between HIPPO-derived T2* values and those obtained using the pixel-wise approach with median or mean values (r = 0.78 in healthy subjects for both, and r = 0.80 with mean or 0.78 with median in patients). However, the correlation increases significantly with the ROI-based approach (r = 0.89 in healthy subjects and r = 0.90 in patients).

The Bland-Altman plot analysis provides further insight. Specifically, when assessing the agreement between T2* values obtained from HIPPO and those derived from our S-EXP model using the ROI-based approach, a mean difference of -2.5 is observed in patients, indicating a systematic bias. This bias reflects the fact that HIPPO systematically estimates T2* values that are, on average, approximately 2.5 units lower than our algorithm. In healthy subjects, this value is reduced and equal to -1.5. In contrast, no such systematic bias is observed with the pixel-wise method: in all cases and across both datasets, the mean difference is close to zero. This suggests no consistent trend of one method systematically producing higher or lower values than the other.

Besides, as explained above, a test-retest was carried out in patients to check if the same results are obtained across repeated acquisitions. Pearson Correlation and Bland-Altman Plot evaluated the correlation and the agreement between the first and the second acquisition in pixel-wise, ROI-Based and HIPPO Software. All Plots show a strong positive linear relationship and mean differences values approximately equal to zero in Bland-Altman Plot (from 0.34 to 0.83), proving a good agreement. These outcomes indicate strong reliability, validating the protocol.

5.3 Correction Factors

As introduced in the previous paragraphs, the creation of an R2* correction map is due to the need to compensate for variations in T2* values because of the presence of geometric and susceptibility artefacts. The R2* correction map implemented in HIPPO software is the one illustrated in section 2.4, calculated on a dataset of healthy subjects acquired in Pisa. Obviously, the Pisa centre has a scanner with acquisition parameters that differ from Padova, as illustrated in the Table 2.3. For this reason, one of the objectives of this work is to calculate a segmental R2* correction map based on subjects acquired in Padova. In this way, these correction factors

would be applied to all segmental T2* estimation results obtained. This ensures accurate, reliable, and reproducible T2* measurements tailored to the specific conditions of Padova centre, which is essential in clinical context. First, again, it was decided to normalize the correction map with respect to the mid-ventricular septum (segments 8 and 9), a region where artefacts are minimal[39] .This assumption has the advantage that measurements in the mid-ventricular septum are not affected by the application of the correction map. Several studies have shown that the clinical cardiac T2* measurements, used to evaluate if there is myocardial iron-overload, should be restricted to the mid-ventricular septum [60]. We have demonstrated that this statement holds true, as the introduction of the CV threshold results in a reduced percentage of discarded voxels in the mid-ventricular septum compared to other segments. For instance, segment 5, which showed a high percentage of discarded voxels due to its artefactual nature, contrasts with segments 8 and 9. This suggests that the signal quality in the mid-ventricular septum is reliable. Further evidence supporting this observation will be provided in subsequent analyses.

In this study, several approaches were used to calculate correction factors for T2*. Specifically, correction factors derived from mean T2* values per segment, median T2*values and T2* obtained from ROI-based approach were initially compared. The results show a strong correlation between these methods, with r = 1.00 between the mean and median values, and r = 0.96 between the pixel-wise approach (using mean values) and the ROI-based method.

A second comparison was made to assess the correlation and agreement between the correction factors derived in this study and those calculated using the cvi42 software [65] in a previous study, based on the same dataset of healthy subjects. In this case, the correlation was weaker (r = 0.72) and analysis using the Bland-Altman plot revealed the presence of a proportional bias, indicating systematic differences between the two approaches. However, this finding is considered to be of limited relevance for the current analysis, as cvi42 uses a different segmentation strategy, which is likely to have contributed to the observed discrepancies. For subsequent analysis and implementation, it was decided to refer to the correction factors calculated from T2* mean values obtained in each segment through pixel-wise technique, applying the selected threshold on the coefficients of variation, since we decided that this is the most reliable estimation method.

Additional analyses were performed to assess the robustness of the calculated correction factors. Specifically, to investigate the influence of the initial dataset of 50 healthy subjects used to generate the normalization map, the correction factors were recalculated five more

times, each time using a subset of 10 subjects. By assuming a T2* value of 20 ms in each segment and applying the new subgroup-derived correction factors, the correlation between the T2* values corrected with the original factors (calculated from the whole data set) and those corrected with the subgroup-derived factors was assessed. The Pearson correlation coefficients ranged from 0.91 to 0.98, indicating variability in the results depending on the subset of subjects used. This means that the composition and size of the initial dataset has an impact on the calculation of the correction map. In addition, we observed significant variability in the correction factors obtained for segments 5 (ranging from 11.72 Hz to 18.73 Hz), segment 10 (ranging from 4.05 Hz to 11.07 Hz), and segment 15 (ranging from 0.57 Hz to 8.57 Hz). This variability is clearly illustrated in Figure 4.46 and in Figure 4.48. We can also observe that the correction factors obtained for segments 8 and 9 are close to zero and show similar values across all subgroups. This consistency further validates the hypothesis that the mid-ventricular segment is a reliable reference. However, further investigation is required to address this sensitivity and improve the reliability of the correction factors. For example, recalculating the correction factors using data from additional healthy subjects could provide valuable insights into their robustness and generalisability. Such efforts would help to validate the consistency of the correction map and ensure its applicability.

Another critical aspect evaluated to validate the robustness of the correction factors was the potential influence of manual errors made by the radiologist in identifying the starting point of the mid-ventricular septum. This step is performed manually and may be subject to variability due to challenges in recognising the septum in some images, such as blurring effects or less distinct anatomical features of the myocardium. Therefore, a fix rotation was applied to all segmentation masks to simulate a systematic error. This simulation considers scenarios where a radiologist may consistently shift the starting point either to the right or left of the junction with the right ventricle due to their individual interpretation. We see that a rotation of ± 2°, either clockwise or counterclockwise, has no effect on the correction factors (r = 1.00). As expected, this indicates that small and realistic deviations in manual segmentation do not affect the calculations. In presence of large errors, the correlation decreases (r=0.82). As a ± 20° error is unlikely in typical clinical practice, the range of variability was refined to ±10° in subsequent analyses, which is a more realistic margin for potential manual error. This new analysis explores the impact of random segmentation errors across multiple simulations. A total of 50 independent simulations were performed, with the error in identifying the starting point of the mid-ventricular septum introduced randomly for each slice from each subject. For each simulation, correction factors were recalculated. To assess the impact of these recalculated

factors, they were applied to a T2* value of 20 ms for each slice. The results, summarised in terms of mean and standard deviation for each slice (see table 4.8), show that across the 50 simulations, the mean error in corrected T2* values remained consistently below 1 ms, regardless of slice or subject. A low standard deviation means that despite the introduction of random errors in the segmentation process, the corrected T2* values remain highly consistent across different simulations. So, the correction factors are not highly sensitive to variability in manual segmentation, ensuring that the results are stable. This is illustrated in Figure 4.50. From all these considerations, it is possible to conclude that the correction method implemented is accurate and reliable.

We underline that the decision to test the correction factors on segments with a T2* value of 20 ms derives from the importance of this threshold in determining the presence of myocardial iron accumulation. This value serves as a critical cut-off: segments corrected above 20 ms do not indicate iron accumulation, whereas segments below 20 ms indicate the presence of iron overload. The identification of such cases may lead to the administration of chelation therapy, with the dosage determined by the global and segmental T2* values obtained. It is therefore important to assess whether the correction applied alters the segmental T2* values in a way that affects the clinical interpretation and subsequent treatment decisions. Besides, since myocardial iron cannot be predicted from serum ferritin or liver iron (these parameters show no correlation with T2* myocardial values [23], therefore magnetic resonance imaging is used as a gold standard for the early detection of cardiac iron deposition. To further investigate the effect of our selected correction factors (obtained from R2* mean values in each segment in pixel-wise approach) on extremely low T2* values (<10 ms), we applied the correction factors to hypothetical T2* segments of 4 ms. As shown in Table 4.3, the results show that the correction map has no significant effect in the presence of severe myocardial iron overload. It is evident that in segments where the correction factors have a high magnitude, there is a consistent increase or decrease in T2* values when the starting value is 20 ms. However, when the starting value is 4 ms, the effect is negligible. This finding confirms the results reported by Positano et al. [39] . So, the higher is the T2* starting value, the higher is also the effect of the correction. This phenomenon has a mathematical basis: the application of correction factors is performed in terms of R2* (the inverse of T2*), followed by the inversion back to T2*. For higher T2* starting values, their reciprocal (R2*) is small, resulting in a greater relative impact from the correction factors. Conversely, for lower T2* starting values, the reciprocal (R2*) is larger, diminishing the influence of the correction. Obviously, the magnitude of the correction factor also influences the results: the smaller the factor, the smaller its effect on the correction. In

addition, the sign of the factor determines the direction of the effect. If the factor has a positive value, the corrected T2* segment value will be higher than the original value, whereas if the factor has a negative value, the corrected T2* segment value will be lower. This relationship highlights how both the magnitude and sign of the correction factor contribute to the adjustments made to the T2* values.

The final consideration concerns the calculation of correction factors derived from the proposed segmentation (Figure 4.52 and Figure 4.53), which is more accurate than the previous one because it allows a clearer definition of the mid-ventricular septum. The correlation between the corrected T2* values in patients (dataset 2) obtained using the standard segmentation and the new segmentation shows that the overall results remain almost unchanged ($r = 0.91$ with the pixel-wise approach and $r = 0.88$ with the ROI-based approach). In particular, the largest differences between the correction factors using the standard and the proposed segmentation approaches occur in segments 4 and 5. Considering the calculations performed with the pixel-wise approach, in the infero segment (number 4) we see that the correction factor increases from 6.93 Hz with the standard segmentation to 13.34 Hz with the proposed segmentation, while in the infero-lateral segment (number 5) the correction factor decreases from 15.48 Hz with the standard segmentation to 12.10 Hz with the proposed segmentation. These changes can be explained by the structural adjustments introduced by the new kind of segmentation. In this approach, segment 3 is extended to include the entire septum, therefore, segment 4 shifts further to the right and includes a region that previously belonged to segment 5, which had a relatively high correction factor, leading to a higher value of segment 4. Similarly, segment 5 now includes part of segment 6 (antero-lateral segment), which has a lower correction factor (2.835 Hz), and so the new correction factor in segment 5 is reduced. In Figures 4.56 and 4.58 segments 4 and 5 are highlighted in red and green, respectively, to emphasize their deviation from the bisector line in the correlation graphs. This indicates a greater difference between T2* values corrected using standard segmentation and those corrected with the new segmentation. Similarly, in the Bland-Altman plots, the highlighted points show a tendency to move further from the zero line, reflecting these discrepancies. We proved that this new segmentation method offers improved anatomical precision, and the high correlation between the standard and new segmentation results confirms that the overall corrected T2* results remain consistent, validating this new method.

LIMITATIONS

The study presents some limitations, some of which have already been mentioned in the previous chapter. Firstly, the patients analysed were undergoing chelation therapy. As a result, no myocardial tissue with iron accumulation was found, except in one person out of ten (Figure 4.19). It is worth precising that in Italy, diseases such as thalassaemia and haemochromatosis are usually diagnosed and treated at an early stage. As a result, myocardial iron accumulation is rare in treated patients, and life expectancy has increased significantly[66]. Secondly, the use of manual segmentation, particularly in delineating the epicardium and endocardium to isolate myocardial tissue, introduces variability that could potentially affect the results. To address this, it would be useful to validate the results by having the segmentations repeated by the same radiologist and then by a second radiologist. This would allow the inter- and intra-observer variability and its impact on the results to be assessed. Regarding the selection of the mid-ventricular septum, previous analyses of correction factors have shown that errors in this process do not significantly affect the results. However, these evaluations were performed using the standard segmentation approach, which divides the left ventricle into equidistant segments. To further validate the robustness of the method, it would be useful to perform similar analyses using the newly implemented segmentation technique, which adjusts the division of segments based on the identification of the mid-ventricular septum. Testing the robustness of the correction factors with this improved segmentation would ensure the reliability and consistency of the results. It may also be useful to repeat the calculation of the correction map with a new Dataset of healthy subjects, to test whether the factors maintain the same magnitude and sign, and to evaluate the degree of correlation with the current factors. Another limitation is the lack of a preliminary study to investigate the presence of image noise. In the analysis of magnetic resonance images, estimating the level of noise in an image could be an important step that allows to assess the quality of the analysis and the consistency of the image processing technique [67].

FUTURE DEVELOPMENTS

This work offers promising opportunities for further development to improve and consolidate these findings. One of the main limitations identified is the variability introduced by manual segmentation. Therefore, the development of a deep learning algorithm that automatically provides a segmentation of the entire myocardium or of the mid-ventricular septum would be a significant advance, reducing user-dependent variability and improving reproducibility [68]. In addition, it would be worth exploring the hypothesis of focusing T2* estimation only to the mid-ventricular septum to assess whether this region alone is sufficient to determine the presence of iron overload. Another avenue for future investigation is to compare T2* mapping with T1 mapping analysis. Some studies have shown that the presence of myocardial iron is associated with a decrease in T1 values. Performing analyses on the same dataset, as well as on a new cohort of patients, to compare the results of T2* and T1 mapping would provide further validations. Although T2* mapping is currently considered the gold standard for detecting iron overload, since it has been widely validated, recent research suggests that combining native T1 and T2* mapping may improve sensitivity for iron detection. This combined approach could provide a more robust framework for quantifying myocardial iron overload, improving both diagnosis and treatment planning [69]. The final enhancement, that is already in progress, focuses on lowering the bandwidth value used during acquisitions, since this parameter can lead to a higher signal to noise ratio [70]. This is possible because bandwidth can be manually adjusted by the operator. Specifically, patients will undergo sequential acquisitions: first at the current bandwidth setting of 814 Hz/Px, followed by acquisitions at a reduced bandwidth of 592 Hz/Px. As the correction map was originally calculated using data from subjects acquired at the higher bandwidth, it is critical to evaluate how this could affect T2* estimates. This will involve assessing the correlation between the T2* values obtained with the original and reduced bandwidth settings. This step is necessary to determine the consistency and reliability of the correction map under different acquisition conditions, ensuring that these new improvements do not introduce discrepancies or compromise the accuracy of T2* estimation.

CONCLUSION

In this study, different models for estimating the transverse T2* relaxation time in cardiac MRI were implemented and compared to assess the presence of iron overload in the left ventricle. The models considered included the bi-exponential, mono-exponential, mono-exponential with an added constant (offset model) and linear models. The results show that the bi-exponential model is unsuitable for estimating T2* in myocardial tissue as its behaviour effectively reduces to that of a mono-exponential model. Bayesian Information Criterion (BIC) analysis confirms that the mono-exponential model is the most appropriate, while the offset model tends to underestimate T2*. In addition, application of a stringent threshold to the coefficients of variation associated with T2* estimates showed that the offset model produced unreliable results. The S-EXP, C-EXP and LIN models were evaluated using both pixel-wise and ROI-based approaches. For the pixel-wise approach, the smoothing effect of all models was evaluated, but we decided to discard this approach since this operation runs the risk of including voxels with no MRI signal, potentially affecting the reliability of the estimates. The T2* results obtained by implementing the mono-exponential model in both ROI-based and pixel-based approaches were compared with those generated by the HIPPO software, which is currently used to analyse T2* in patients with haemochromatosis in Padova Hospital, and the estimates obtained are comparable. The results of this study aim to provide the basis for the development of a new graphical interface designed for research purposes and, after necessary validation, for potential clinical use to replace or complement this existing software. In addition, an R2* correction map was calculated from a dataset of healthy subjects acquired at the Padua centre. This map is essential to correct for geometric distortions and susceptibility artefacts that affect the images and can lead to wrong diagnoses. Correction factors were calculated using different methods, with the most reliable results obtained from the average T2* values in each segment, calculated by the mono-exponential model using a pixel-wise approach. Although the ROI-based approach has proven to be a reliable method for estimating T2* in any cardiac segment, the pixel-wise approach is preferable due to its greater sensitivity to individual voxels with absent or unreliable signals. The robustness of the calculated correction factors was tested by simulating potential radiologist error in selecting the starting point of the interventricular septum, which is used as a reference for dividing the myocardium into uniform, equidistant segments. These simulations further validated the reliability of the correction factors to account for inter- and intra- subjects variability. In addition, recognising the limitations of standard segmentation, such as cases where segments 8 and 9 (antero- and infero-septal) do not fully encompass the mid-ventricular septum, an updated segmentation method was developed. In this

approach, the start and end points of the septum are manually selected and the division into segments is adjusted to align with these boundaries. This improved segmentation method also allows the creation of an additional R2* correction map tailored to this updated framework. The results obtained are consistent with the findings reported in the literature and allow to refine and extend them using data specifically collected in Padova. These ad hoc analyses were carried out with the aim of replacing and improving the tools currently available, providing a more accurate and robust solution for clinical and research applications.

APPENDIX

The following Tables refer to correction factors obtained from the random rotations of segmentation masks and the corrected T2* values obtained with those factors (see paragraph 4.9.5).

sim=1	sim=2	sim=3	sim=4	sim=5	sim=6	sim=7	sim=8	sim=9	sim=10
1,651	1,567	2,142	2,190	1,973	1,782	1,525	1,428	1,510	1,756
0,327	0,252	0,102	0,093	-0,088	0,274	0,436	0,067	0,277	0,033
0,250	0,721	1,151	0,295	0,686	0,246	0,004	0,250	0,502	0,434
7,627	7,637	7,527	7,321	7,804	7,125	8,879	8,534	8,982	8,325
15,557	14,109	13,623	15,500	14,812	14,197	14,784	14,597	15,067	14,898
3,046	2,963	2,999	3,068	2,995	3,565	3,020	2,821	2,579	3,126
0,830	0,849	0,682	0,890	0,982	0,692	1,297	1,074	1,317	0,496
-0,258	-0,150	-0,308	-0,131	-0,112	-0,260	-0,232	-0,125	-0,190	-0,277
0,258	0,150	0,308	0,131	0,112	0,260	0,232	0,125	0,190	0,277
5,957	5,466	5,236	5,461	4,527	5,368	5,004	4,918	5,159	4,710
6,600	7,082	6,973	7,124	6,559	7,358	7,496	7,486	7,065	6,494
1,942	1,682	1,413	1,186	1,908	2,187	1,634	1,568	1,716	1,271
1,940	2,521	1,587	1,576	1,884	1,654	1,858	2,179	1,611	2,334
-3,604	-3,319	-3,473	-3,823	-3,667	-3,596	-3,490	-3,826	-3,534	-3,848
5,475	5,072	5,435	5,759	5,405	6,196	5,714	5,544	5,637	5,754
6,440	6,551	6,687	6,260	6,306	6,707	6,492	6,507	6,606	6,232

sim=11	sim=12	sim=13	sim=14	sim=15	sim=16	sim=17	sim=18	sim=19	sim=20
1,758	2,665	1,731	1,531	1,632	1,839	2,056	2,434	1,431	2,296
-0,069	0,082	0,386	0,338	-0,025	0,203	0,313	0,015	-0,306	0,147
0,544	0,169	0,379	0,007	0,690	0,020	-0,092	0,172	0,411	0,491
6,467	7,437	8,459	8,487	7,150	8,138	8,277	7,714	7,591	5,771
14,153	14,902	14,107	15,131	14,155	14,942	15,471	14,970	13,936	13,626
2,790	3,137	2,381	2,811	2,793	2,751	3,208	3,189	2,546	2,801
0,888	1,394	1,165	1,154	1,068	0,975	1,079	1,173	0,710	0,783
-0,173	-0,111	-0,057	-0,131	-0,163	-0,197	-0,055	-0,123	-0,194	-0,222
0,173	0,111	0,057	0,131	0,163	0,197	0,055	0,123	0,194	0,222
5,539	4,674	5,484	4,198	4,523	5,325	4,620	4,243	5,223	5,684
6,993	7,369	7,121	7,053	7,229	7,109	7,453	7,810	6,748	6,956
1,513	1,818	1,876	2,417	2,116	1,689	1,970	1,696	1,264	1,812
1,706	1,854	2,165	1,825	1,757	1,799	1,794	2,006	1,509	1,426
-3,531	-3,468	-3,621	-3,621	-3,679	-3,401	-3,707	-3,649	-3,905	-3,303
5,266	5,267	5,789	5,073	5,080	5,764	5,891	5,755	5,757	5,636
6,513	6,305	6,454	6,579	6,463	6,563	6,440	6,394	5,989	6,659

sim=21	sim=22	sim=23	sim=24	sim=25	sim=26	sim=27	sim=28	sim=29	sim=30
1,985	1,247	1,859	1,945	1,377	1,793	1,713	1,900	2,086	1,588
0,048	0,052	0,269	0,026	0,155	-0,019	-0,086	0,287	-0,092	0,156
0,281	0,107	-0,122	0,483	0,769	0,018	0,312	0,320	0,238	-0,086
7,882	9,029	8,952	7,867	8,329	6,964	7,350	8,676	8,005	6,992
14,746	14,668	14,678	14,364	14,662	14,852	14,595	15,273	13,667	14,741
2,655	2,478	3,323	2,949	2,828	2,988	2,528	2,865	2,561	2,445
0,895	0,997	1,046	1,144	0,988	0,926	0,575	1,301	0,729	0,854
-0,098	-0,144	-0,243	-0,063	-0,044	-0,319	-0,320	-0,051	-0,165	-0,273
0,098	0,144	0,243	0,063	0,044	0,319	0,320	0,051	0,165	0,273
5,245	5,543	4,509	5,496	4,909	5,886	5,269	5,521	5,514	5,453
7,126	7,346	7,296	7,192	7,247	6,806	7,232	7,062	6,848	7,100
1,862	1,435	2,186	1,645	1,530	2,417	1,611	1,770	1,858	1,397
1,309	1,668	1,727	2,076	1,785	1,886	1,951	1,725	2,165	1,835
-3,786	-3,773	-3,523	-3,647	-3,774	-3,664	-3,960	-3,594	-3,621	-3,953
5,500	5,266	5,458	5,994	5,959	5,248	5,828	6,161	5,370	5,425
6,856	6,390	6,675	6,523	6,505	6,892	5,930	6,531	6,362	6,305

sim=31	sim=32	sim=33	sim=34	sim=35	sim=36	sim=37	sim=38	sim=39	sim=40
2,031	2,213	1,446	1,514	1,819	1,505	2,237	1,672	1,966	1,267
-0,100	0,041	0,084	0,148	0,324	0,348	0,156	0,066	0,200	0,136
0,399	0,152	0,658	0,591	0,387	-0,011	0,631	0,323	0,372	0,642
7,819	7,330	7,148	8,277	8,382	7,744	6,685	8,369	7,095	8,043
14,613	13,970	13,788	14,434	15,274	13,852	15,003	14,399	14,890	14,404
2,916	2,831	3,218	2,545	2,356	3,283	3,116	2,617	3,013	2,672
0,947	0,982	1,019	0,901	0,928	0,817	0,643	0,945	1,126	0,851
-0,210	-0,134	-0,286	-0,185	-0,174	-0,275	-0,210	-0,190	-0,039	-0,207
0,210	0,134	0,286	0,185	0,174	0,275	0,210	0,190	0,039	0,207
5,287	4,916	5,507	4,789	5,339	5,170	5,085	3,901	4,562	5,620
6,676	7,829	7,465	7,394	6,914	6,892	7,269	7,331	7,057	7,137
1,948	1,550	1,642	1,698	2,160	1,928	1,992	1,931	1,783	1,966
1,696	1,883	1,775	2,164	1,790	1,966	2,165	2,350	1,858	1,580
-3,644	-3,454	-3,460	-3,666	-3,535	-3,557	-3,582	-3,613	-3,830	-3,804
5,357	4,852	5,417	5,325	5,758	5,698	5,237	5,026	5,876	4,833
6,503	6,522	6,447	6,663	6,578	6,348	6,536	6,774	6,569	6,274

sim=41	sim=42	sim=43	sim=44	sim=45	sim=46	sim=47	sim=48	sim=49	sim=50
2,093	1,441	2,015	1,891	2,205	1,904	1,497	1,483	1,871	1,560
-0,123	0,342	0,155	0,224	0,019	-0,218	-0,029	0,104	0,168	0,103
0,415	0,713	0,113	0,770	0,610	0,693	-0,012	0,688	0,161	0,728
7,222	7,721	7,551	7,376	7,367	7,982	8,539	7,364	8,232	7,539
14,860	15,104	15,290	14,311	14,753	13,904	15,076	14,201	14,705	14,256
3,562	2,995	3,072	2,885	2,948	2,569	2,562	2,669	2,757	2,691
1,012	0,731	1,011	0,711	0,961	0,834	1,044	1,085	0,936	0,888
-0,162	-0,164	-0,006	-0,163	-0,111	-0,332	-0,264	-0,053	-0,162	-0,291
0,162	0,164	0,006	0,163	0,111	0,332	0,264	0,053	0,162	0,291
4,436	4,499	5,353	5,698	5,988	5,377	4,038	4,984	4,681	4,876
7,291	7,114	6,828	7,081	7,084	6,412	7,030	7,185	6,954	7,297
1,633	1,924	1,687	1,667	1,486	1,740	1,562	1,611	2,037	1,546
1,714	1,746	1,904	1,369	1,541	1,321	2,274	1,691	2,418	1,789
-3,566	-3,786	-3,500	-3,654	-3,719	-3,814	-3,499	-3,810	-3,633	-3,996
5,474	6,104	5,396	5,721	5,800	5,639	5,024	5,268	5,473	5,903
6,363	6,565	6,671	6,501	6,313	6,424	6,267	6,255	6,541	6,562

Table. R2* (Hz) Correction Factors obtained after random mask rotation

sim=1	sim=2	sim=3	sim=4	sim=5	sim=6	sim=7	sim=8	sim=9	sim=10
20,683	20,647	20,895	20,916	20,821	20,739	20,629	20,588	20,623	20,728
20,132	20,101	20,041	20,037	19,965	20,110	20,176	20,027	20,112	20,013
20,101	20,293	20,471	20,119	20,278	20,099	20,001	20,100	20,203	20,175
23,600	23,606	23,544	23,431	23,699	23,323	24,318	24,116	24,380	23,995
29,033	27,862	27,490	28,985	28,419	27,930	28,396	28,246	28,626	28,488
21,298	21,260	21,276	21,307	21,275	21,535	21,286	21,196	21,087	21,334
20,338	20,345	20,276	20,363	20,401	20,281	20,533	20,439	20,541	20,200
19,897	19,940	19,877	19,948	19,955	19,896	19,908	19,950	19,924	19,890
20,104	20,060	20,124	20,053	20,045	20,105	20,093	20,050	20,076	20,111
22,705	22,455	22,340	22,452	21,991	22,406	22,224	22,182	22,301	22,080
23,041	23,300	23,241	23,323	23,020	23,451	23,527	23,521	23,291	22,985
20,808	20,696	20,582	20,486	20,794	20,915	20,676	20,647	20,711	20,522
20,807	21,062	20,656	20,651	20,783	20,684	20,772	20,911	20,666	20,979
18,655	18,755	18,701	18,579	18,633	18,658	18,695	18,578	18,680	18,571
22,459	22,258	22,439	22,603	22,424	22,829	22,581	22,494	22,542	22,601
22,957	23,015	23,088	22,862	22,887	23,098	22,984	22,992	23,045	22,848

sim=11	sim=12	sim=13	sim=14	sim=15	sim=16	sim=17	sim=18	sim=19	sim=20
20,729	21,126	20,717	20,632	20,675	20,764	20,858	21,023	20,589	20,963
19,972	20,033	20,156	20,136	19,990	20,082	20,126	20,006	19,878	20,059
20,220	20,068	20,153	20,003	20,280	20,008	19,963	20,069	20,166	20,198
22,971	23,495	24,073	24,089	23,337	23,888	23,967	23,648	23,580	22,610
27,896	28,492	27,861	28,679	27,898	28,524	28,961	28,547	27,728	27,492
21,182	21,339	21,000	21,191	21,183	21,164	21,371	21,362	21,073	21,187
20,361	20,573	20,477	20,473	20,437	20,398	20,441	20,480	20,288	20,318
19,931	19,956	19,977	19,948	19,935	19,921	19,978	19,951	19,923	19,911
20,069	20,045	20,023	20,053	20,065	20,079	20,022	20,049	20,078	20,089
22,492	22,062	22,464	21,833	21,989	22,384	22,036	21,854	22,333	22,565
23,252	23,457	23,321	23,285	23,381	23,315	23,504	23,702	23,120	23,232
20,624	20,755	20,779	21,016	20,884	20,699	20,820	20,702	20,519	20,752
20,706	20,770	20,905	20,758	20,729	20,747	20,744	20,836	20,623	20,587
18,681	18,703	18,650	18,650	18,629	18,726	18,620	18,640	18,551	18,761
22,354	22,355	22,619	22,258	22,262	22,606	22,671	22,601	22,602	22,541
22,995	22,886	22,964	23,030	22,969	23,022	22,957	22,933	22,722	23,073

sim=21	sim=22	sim=23	sim=24	sim=25	sim=26	sim=27	sim=28	sim=29	sim=30
20,827	20,512	20,772	20,810	20,566	20,744	20,710	20,790	20,871	20,656
20,019	20,021	20,108	20,010	20,062	19,992	19,966	20,116	19,963	20,063
20,113	20,043	19,952	20,195	20,312	20,007	20,125	20,129	20,096	19,966
23,743	24,408	24,362	23,734	23,998	23,236	23,447	24,199	23,813	23,251
28,365	28,303	28,311	28,061	28,298	28,451	28,244	28,796	27,523	28,361
21,121	21,043	21,424	21,253	21,199	21,271	21,065	21,216	21,080	21,028
20,365	20,407	20,427	20,468	20,403	20,378	20,233	20,534	20,296	20,347
19,961	19,943	19,903	19,975	19,982	19,873	19,873	19,980	19,934	19,891
20,039	20,058	20,098	20,025	20,018	20,128	20,129	20,020	20,066	20,110
22,344	22,494	21,982	22,470	22,177	22,668	22,356	22,483	22,479	22,448
23,324	23,445	23,417	23,360	23,390	23,151	23,382	23,290	23,174	23,310
20,774	20,591	20,914	20,680	20,631	21,016	20,666	20,734	20,772	20,575
20,538	20,690	20,716	20,866	20,740	20,784	20,812	20,715	20,905	20,762
18,592	18,597	18,683	18,640	18,596	18,634	18,532	18,659	18,650	18,534
22,472	22,354	22,451	22,724	22,706	22,345	22,639	22,811	22,407	22,434
23,178	22,930	23,082	23,001	22,991	23,197	22,691	23,005	22,916	22,886

sim=31	sim=32	sim=33	sim=34	sim=35	sim=36	sim=37	sim=38	sim=39	sim=40
20,847	20,926	20,596	20,625	20,755	20,621	20,937	20,692	20,818	20,520
19,960	20,016	20,034	20,059	20,131	20,140	20,063	20,026	20,081	20,055
20,161	20,061	20,267	20,239	20,156	19,996	20,256	20,130	20,150	20,260
23,707	23,436	23,336	23,968	24,028	23,665	23,087	24,021	23,307	23,834
28,259	27,755	27,615	28,117	28,797	27,664	28,574	28,089	28,482	28,093
21,239	21,200	21,376	21,073	20,989	21,406	21,329	21,105	21,282	21,129
20,386	20,401	20,416	20,367	20,378	20,332	20,260	20,385	20,461	20,346
19,916	19,946	19,886	19,926	19,931	19,891	19,916	19,924	19,985	19,918
20,084	20,054	20,115	20,074	20,070	20,110	20,084	20,076	20,015	20,083
22,365	22,181	22,476	22,119	22,391	22,306	22,264	21,692	22,008	22,533
23,082	23,713	23,510	23,471	23,209	23,197	23,402	23,436	23,286	23,330
20,811	20,640	20,679	20,703	20,903	20,802	20,830	20,804	20,739	20,819
20,702	20,783	20,736	20,905	20,743	20,819	20,905	20,986	20,772	20,653
18,641	18,708	18,706	18,634	18,680	18,672	18,663	18,652	18,577	18,586
22,400	22,149	22,430	22,384	22,603	22,572	22,340	22,235	22,663	22,140
22,990	23,000	22,960	23,075	23,030	22,909	23,008	23,134	23,025	22,870

sim=41	sim=42	sim=43	sim=44	sim=45	sim=46	sim=47	sim=48	sim=49	sim=50
20,874	20,593	20,840	20,786	20,923	20,792	20,617	20,611	20,778	20,644
19,951	20,138	20,062	20,090	20,008	19,913	19,988	20,042	20,067	20,041
20,167	20,289	20,045	20,313	20,247	20,281	19,995	20,279	20,064	20,296
23,377	23,653	23,557	23,461	23,456	23,800	24,119	23,454	23,942	23,551
28,458	28,657	28,810	28,020	28,371	27,704	28,633	27,934	28,332	27,976
21,534	21,274	21,309	21,225	21,253	21,083	21,080	21,128	21,167	21,138
20,413	20,297	20,413	20,288	20,392	20,339	20,427	20,444	20,382	20,362
19,935	19,935	19,997	19,935	19,956	19,868	19,895	19,979	19,936	19,884
20,065	20,066	20,003	20,066	20,045	20,134	20,106	20,021	20,065	20,117
21,947	21,977	22,398	22,572	22,721	22,410	21,757	22,214	22,066	22,161
23,414	23,318	23,163	23,300	23,301	22,942	23,272	23,356	23,231	23,418
20,675	20,800	20,698	20,690	20,612	20,721	20,645	20,666	20,849	20,638
20,710	20,724	20,792	20,563	20,636	20,543	20,953	20,700	21,016	20,742
18,668	18,592	18,691	18,638	18,615	18,583	18,692	18,584	18,645	18,520
22,459	22,781	22,420	22,584	22,624	22,542	22,234	22,356	22,458	22,677
22,916	23,023	23,079	22,989	22,890	22,948	22,866	22,860	23,010	23,021

Table. T2* (ms) Post-correction segments (starting from an initial value of 20 ms in each segment)

Bibliography

[1] G. D. Clarke, J. Li, A. H. Kuo, A. J. Moody, and P. W. Nathanielsz, "Cardiac magnetic resonance imaging: Insights into developmental programming and its consequences for aging," Apr. 01, 2021, *Cambridge University Press*. doi: 10.1017/S2040174420001233.

[2] D. Stäb, J. Roessler, K. O'Brien, C. Hamilton-Craig, and M. Barth, "ECG Triggering in Ultra-High Field Cardiovascular MRI," *Tomography*, vol. 2, no. 3, pp. 167–174, Sep. 2016, doi: 10.18383/j.tom.2016.00193.

[3] N. Ferris, "Gadolinium Contrast Medium (MRI Contrast Agents). ," *Inside Radiology, General Radiology.*, 2017.

[4] C. JV. Shellock FG, "MR procedures: biologic effects, safety, and patient care," *Radiology*, pp. 635–52, 2004.

[5] B. JA. Murphy KJ, "Adult claustrophobia, anxiety and sedation in MRI ," *Magn Reson Imaging*, vol. 15(1), pp. 51–4, 1997.

[6] R. Guo *et al.*, "Emerging Techniques in Cardiac Magnetic Resonance Imaging," Apr. 01, 2022, *John Wiley and Sons Inc*. doi: 10.1002/jmri.27848.

[7] S. Mori, J. T. Tretter, D. E. Spicer, D. L. Bolender, and R. H. Anderson, "What is the real cardiac anatomy?," Apr. 01, 2019, *John Wiley and Sons Inc.* doi: 10.1002/ca.23340.

[8] D. Silverthorn, *Human Physiology: an integrated approach* , 7th ed. PearsonEducation, 2016.

[9] "'Heart'. Encyclopedia Britannica ://www.britannica.com/science/heart. Accessed 6 November 2024."

[10] L. Gartner and J. Hiatt, *Concise Histology, cap 11 – Circulatory system*. 2011.

[11] Suren Abreu · Mandira P., "https://socratic.org/questions/how-many-walls-does-the-human-heart-have."

[12] P. Storey, "Magnetic Resonance Imaging: Methods and Biologic Applications Edited by."

[13] M. H. Levitt, *Spin Dynamics: Basics of Nuclear Magnetic Resonance* , 2nd ed. Wiley, 2008.

[14] A. C. Ogier, A. Bustin, H. Cochet, J. Schwitter, and R. B. van Heeswijk, "The Road Toward Reproducibility of Parametric Mapping of the Heart: A Technical Review," May 06, 2022, *Frontiers Media S.A.* doi: 10.3389/fcvm.2022.876475.

[15] A. O. Leung, I. Paterson, and R. B. Thompson, "Free-breathing cine MRI," *Magn Reson Med*, vol. 60, no. 3, pp. 709–717, 2008, doi: 10.1002/mrm.21711.

[16] "https://radiologykey.com/cardiac-mri/."

[17] A. Piperno, “www.emocromatosi.it/articoli/metabolismo.”

[18] P. Cucchi, C. Vullo, and Barrai I, “Population genetics in the province of ferrara. II. Survival of children with Cooley’s anemia,” *Am J Hum Genet.*, pp. 178–183, 1977.

[19] P. A. Wahidiyat, F. Liauw, D. Sekarsari, S. A. Putriasih, V. Berdoukas, and D. J. Pennell, “Evaluation of cardiac and hepatic iron overload in thalassemia major patients with T2* magnetic resonance imaging,” *Hematology*, vol. 22, no. 8, pp. 501–507, Sep. 2017, doi: 10.1080/10245332.2017.1292614.

[20] N. Olivieri and G. Brittenham, “Iron-chelating therapy and the treatment of thalassemia,” *Blood*, pp. 739–761, 1997.

[21] D. J. Pennell, “T2* magnetic resonance and myocardial iron in thalassemia,” in *Annals of the New York Academy of Sciences*, New York Academy of Sciences, 2005, pp. 373–378. doi: 10.1196/annals.1345.045.

[22] C. Borgna-Pignatti, M. Cappellini, and P. De Stefano, “Cardiac morbidity and mortality in deferoxamine- or deferiprone-treated patients with thalassemia major,” *Blood*, vol. 107, pp. 3733–3737, 2006.

[23] L. J. Anderson *et al.*, “Cardiovascular T2-star (T2*) magnetic resonance for the early diagnosis of myocardial iron overload,” *Eur Heart J*, vol. 22, no. 23, pp. 2171–2179, 2001, doi: 10.1053/euhj.2001.2822.

[24] J. C. Wood, “Use of magnetic resonance imaging to monitor iron overload,” 2014, *W.B. Saunders*. doi: 10.1016/j.hoc.2014.04.002.

[25] J. L. Fernandes, “MRI for Iron Overload in Thalassemia,” Apr. 01, 2018, *W.B. Saunders*. doi: 10.1016/j.hoc.2017.11.012.

[26] N. Olivieri and D. Nathan, “Survival in medically treated patients with homozygous beta-thalassemia ,” *N Engl J Med*, vol. 331(9), pp. 574–8, 1994.

[27] A. Piga, F. Longo, and L. Duca, “High nontransferrin bound iron levels and heart disease in thalassemia major,” *Am J Hematol*, vol. 84, pp. 29–33, 2009.

[28] M. Emond and M. Bronner et al, “Quantitative study of the variability of hepatic iron concentrations,” *Clin Chem*, vol. 45, pp. 340–6, 1999.

[29] O. Leone, J. Veinot, and A. Angelini, “Consensus statement on endomyocardial biopsy from the Association for European Cardiovascular Pathology and the Society for Cardiovascular Pathology,” *Cardiovasc Pathol*, vol. 21, pp. 245–274, 2012.

[30] Fu Luo Xian and Xue Qian Xie et al, “Dual-energy CT for patients suspected of having liver iron overload: can virtual iron content imaging accurately quantify liver iron content?,” *Radiology*, vol. 277(1), pp. 95–103, 2015.

[31] P. S. Rajiah, C. J. François, and T. Leiner, “Cardiac MRI: State of the Art,” *Radiology*, vol. 307, no. 3, May 2023, doi: 10.1148/RADIOL.223008.

[32] K. Menacho, A. Abdel-Gadir, J. C. Moon, and J. L. Fernandes, “T2* Mapping Techniques: Iron Overload Assessment and Other Potential Clinical Applications,” Aug. 01, 2019, *W.B. Saunders*. doi: 10.1016/j.mric.2019.04.008.

[33] M. Westwood and L. Anderson et al, “A single breath-hold multiecho T2* cardiovascular magnetic resonance technique for diagnosis of myocardial iron overload ,” *J Magn Reson Imaging*, vol. 18(1), pp. 33–9, 2003.

[34] P. DJ. Baksi AJ, “T2* imaging of the heart: methods, applications, and outcomes ,” *Top Magn Reson Imaging*, vol. 23(1), pp. 13–20, 2014.

[35] M. Tanner, H. Taigang, and M. Westwood, “Multi-center validation of the transferability of the magnetic resonance T2* technique for the quantification of tissue iron ,” *Haematologica*, vol. 91(10), pp. 1338–91, 2006.

[36] J. Carpenter et al, “On T2* magnetic resonance and cardiac iron ,” *Circulation*, vol. 123(14), pp. 1519–28, 2011.

[37] P. Kirk and M. Roughton, “Cardiac T2* magnetic resonance for prediction of cardiac complications in thalassemia major,” *Circulation*, vol. 120(20), pp. 1961–8, 2009.

[38] DJ Pennell and JE Udelson et al, “Cardiovascular function and treatment in beta-thalassemia major: a consensus statement from the American Heart Association,” *Circulation*, vol. 128(3), pp. 281–308, 2013.

[39] V. Positano *et al.*, “Standardized T2* map of normal human heart in vivo to correct T2* segmental artefacts,” *NMR Biomed*, vol. 20, no. 6, pp. 578–590, Oct. 2007, doi: 10.1002/nbm.1121.

[40] T. He, P. D. Gatehouse, G. C. Smith, R. H. Mohiaddin, D. J. Pennell, and D. N. Firmin, “Myocardial T2* measurements in iron-overloaded thalassemia: An in vivo study to investigate optimal methods of quantification,” *Magn Reson Med*, vol. 60, no. 5, pp. 1082–1089, 2008, doi: 10.1002/mrm.21744.

[41] V. Positano *et al.*, “Multislice multiecho T2* cardiac magnetic resonance for the detection of heterogeneous myocardial iron distribution in thalassaemia patients,” *NMR Biomed*, vol. 22, no. 7, pp. 707–715, 2009, doi: 10.1002/nbm.1382.

[42] T. He, P. D. Gatehouse, P. Kirk, R. H. Mohiaddin, D. J. Pennell, and D. N. Firmin, “Myocardial T2* measurement in iron-overloaded Thalassemia: An ex vivo study to investigate optimal methods of quantification,” *Magn Reson Med*, vol. 60, no. 2, pp. 350–356, 2008, doi: 10.1002/mrm.21625.

[43] T. He *et al.*, “Automated truncation method for myocardial T2* measurement in thalassemia,” *Journal of Magnetic Resonance Imaging*, vol. 37, no. 2, pp. 479–483, Feb. 2013, doi: 10.1002/jmri.23780.

[44] J. M. Bonny, M. Zanca, J. Y. Boire, and A. Veyre, “T2 maximum likelihood estimation from multiple spin-echo magnitude images,” *Magn Reson Med*, vol. 36, no. 2, pp. 287–293, 1996, doi: 10.1002/mrm.1910360216.

[45] G. Brix, L. Schad, and W. Lorenz, “Evaluation of proton density by magnetic resonance imaging: phantom experiments and analysis of multiple component proton transverse relaxation.,” *Phys. Med. Biol.*, vol. 35, pp. 53–66, 1990.

[46] T. G. St Pierre, P. R. Clark, and W. Chua-anusorn, “Single spin-echo proton transverse relaxometry of iron-loaded liver,” Nov. 2004. doi: 10.1002/nbm.905.

[47] M. Cerqueira *et al*., “Standardized myocardial segmentation and nomenclature for tomographic imaging of the heart: a statement for healthcare professionals from the Cardiac Imaging Committee of the Council on Clinical Cardiology of the American Heart Association,” *Circulation*, vol. 105, pp. 539–542, 2002.

[48] A. Ramazzotti *et al.*, “Multicenter validation of the magnetic resonance T2* technique for segmental and global quantification of myocardial iron,” *Journal of Magnetic Resonance Imaging*, vol. 30, no. 1, pp. 62–68, Jul. 2009, doi: 10.1002/jmri.21781.

[49] S. B. Reeder, A. Z. Faranesh, J. L. Boxerman, and E. R. Mcveigh, “In Vivo Measurement of T2* and Field Inhomogeneity Maps in the Human Heart at 1.5 T.”

[50] M. K. Atalay, B. P. Poncelet, H. L. Kantor, T. J. Brady, and R. M. Weisskoff, “Cardiac susceptibility artifacts arising from the heart-lung interface,” *Magn Reson Med*, vol. 45, no. 2, pp. 341–345, 2001, doi: 10.1002/1522-2594(200102)45:2<341::AID-MRM1043>3.0.CO;2-Q.

[51] C. M. Wacker *et al.*, “Changes in myocardial oxygenation and perfusion under pharmacological stress with dipyridamole: Assessment using T*2 and T1 measurements,” *Magn Reson Med*, vol. 41, no. 4, pp. 686–695, 1999, doi: 10.1002/(SICI)1522-2594(199904)41:4<686::AID-MRM6>3.0.CO;2-9.

[52] A. Pepe *et al.*, “Evaluation of the efficacy of oral deferiprone in β-thalassemia major by multislice multiecho T2,” *Eur J Haematol*, vol. 76, no. 3, pp. 183–192, Mar. 2006, doi: 10.1111/j.1600-0609.2005.00587.x.

[53] D. R. Messroghli *et al.*, “Clinical recommendations for cardiovascular magnetic resonance mapping of T1, T2, T2 and extracellular volume: A consensus statement by the Society for Cardiovascular Magnetic Resonance (SCMR) endorsed by the European Association for Cardiovascular Imaging (EACVI),” Oct. 09, 2017, *BioMed Central Ltd.* doi: 10.1186/s12968-017-0389-8.

[54] N. Kawel-Boehm *et al.*, “Reference ranges (‘normal values’) for cardiovascular magnetic resonance (CMR) in adults and children: 2020 update,” Dec. 01, 2020, *BioMed Central Ltd*. doi: 10.1186/s12968-020-00683-3.

[55] A. A. Neath and J. E. Cavanaugh, “The Bayesian information criterion: Background, derivation, and applications,” *Wiley Interdiscip Rev Comput Stat*, vol. 4, no. 2, pp. 199–203, Mar. 2012, doi: 10.1002/wics.199.

[56] N. Martini *et al.*, “Fully Automated Regional Analysis of Myocardial T2* Values for Iron Quantification Using Deep Learning,” *Electronics (Switzerland)*, vol. 11, no. 17, Sep. 2022, doi: 10.3390/electronics11172749.

[57] S. Gambato, “T2 e T2* mapping miocardico con approccio segmentario quantitativo: valori di normalità, effetti dell’invecchiamento e differenze di genere,” 2022.

[58] A. Weibull, H. Gustavsson, S. Mattsson, and J. Svensson, “Investigation of spatial resolution, partial volume effects and smoothing in functional MRI using artificial 3D time series,” *Neuroimage*, vol. 41, no. 2, pp. 346–353, Jun. 2008, doi: 10.1016/j.neuroimage.2008.02.015.

[59] E. S. H. Ibrahim, A. M. Khalifa, and A. K. Eldaly, “Influence of the analysis technique on estimating hepatic iron content using MRI,” *Journal of Magnetic Resonance Imaging*, vol. 44, no. 6, pp. 1448–1455, Dec. 2016, doi: 10.1002/jmri.25317.

[60] N. R. Ghugre, C. M. Enriquez, T. D. Coates, M. D. Nelson, and J. C. Wood, “Improved R2* measurement in myocardial iron overload,” *Journal of Magnetic Resonance Imaging*, vol. 23, no. 1, pp. 9–16, Jan. 2006, doi: 10.1002/jmri.20467.

[61] G. J. Kontoghiorghes, K. Pattichi, M. Hadjigavriel, and A. Kolnagou, “Transfusional iron overload and chelation therapy with deferoxamine and deferiprone (L1).” [Online]. Available: www.elsevier.com/locate/transci

[62] H. S. D. B. et al Anderson LJ, “Cardiovascular T2-star (T2*) magnetic resonance for the early diagnosis of myocardial iron overload,” vol. 22(23), pp. 2171–9, 2001.

[63] J.-P. Carpenter, A. E. Grasso, J. B. Porter, F. Shah, J. Dooley, and D. J. Pennell, “On myocardial siderosis and left ventricular dysfunction in hemochromatosis,” 2013. [Online]. Available: http://www.jcmr-online.com/content/15/1/24

[64] A. Meloni, H. Y. Rienhoff, A. Jones, A. Pepe, M. Lombardi, and J. C. Wood, “Cardiac R2* values are independent of the image analysis approach employed,” *Magn Reson Med*, vol. 72, no. 2, pp. 485–491, 2014, doi: 10.1002/mrm.24942.

[65] “Complete cvi42 Overview- INNOVATION TO STREAMLINE CARDIOVASCULAR IMAGING.”

[66] C. Borgna-Pignatti *et al.*, “Survival and complications in thalassemia,” in *Annals of the New York Academy of Sciences*, New York Academy of Sciences, 2005, pp. 40–47. doi: 10.1196/annals.1345.006.

[67] P. Coupé, J. V. Manjón, E. Gedamu, D. Arnold, M. Robles, and D. L. Collins, “Robust Rician noise estimation for MR images,” *Med Image Anal*, vol. 14, no. 4, pp. 483–493, Aug. 2010, doi: 10.1016/j.media.2010.03.001.

[68] Z. Lian, Q. Lu, B. Lin, L. Chen, P. Peng, and Y. Feng, “MRI Deep Learning-Based Automatic Segmentation of Interventricular Septum for Black-Blood Myocardial T2* Measurement in Thalassemia,” *Journal of Magnetic Resonance Imaging*, vol. 60, no. 2, pp. 651–661, Aug. 2024, doi: 10.1002/jmri.29113.

[69] A. Meloni *et al.*, “Myocardial iron overload by cardiovascular magnetic resonance native segmental T1 mapping: a sensitive approach that correlates with cardiac complications,” *Journal of Cardiovascular Magnetic Resonance*, vol. 23, no. 1, Dec. 2021, doi: 10.1186/s12968-021-00765-w.

[70] Joachim Graessner, “Bandwidth in MRI,” *MAGNETOM Flash, Siemens Healthcare*, 2013.

Ringraziamenti

Non posso concludere questo lavoro senza ringraziare tutte le persone che mi sono state accanto durante questi anni. Di certo queste poche righe non sono sufficienti per esprimere l'immensa gratitudine che provo per voi, ma se oggi termino con soddisfazione e gioia questo percorso voglio che sappiate che è anche merito vostro. Comincio ringraziando i miei genitori e i miei fratelli. Grazie mamma e grazie papà per avermi sostenuta in ogni singolo momento, per aver condiviso i momenti più belli ma anche quelli più difficili, senza mai farmi dimenticare quanto sia unica e speciale la nostra famiglia. Inoltre, grazie nonni e grazie zii, perché siete da sempre un supporto fondamentale nella mia vita.

Un ringraziamento speciale lo dedico a te Mattia, perché mi sei sempre stato vicino, e non avrei vissuto allo stesso modo nessuno di questi anni senza il tuo appoggio costante. Grazie perché riesci a farmi sorridere anche nei momenti più duri. Non posso poi non ringraziare tutti i miei amici e le mie amiche, da coloro che hanno condiviso con me gli anni universitari, a quelli che mi conoscono da quando ero bambina. Sono circondata da persone meravigliose e so di essere fortunata ad avervi con me.

Vorrei spendere le ultime parole per ringraziare il mio relatore, il Professor Marco Castellaro, per avermi dato la possibilità di prendere parte a questo progetto e per l'immensa disponibilità che ha sempre dimostrato. Ti ringrazio Marco per la passione e l'entusiasmo che mi hai trasmesso. Esprimo un sincero ringraziamento anche alla Dott.ssa Amalia Lupi e alla Prof.ssa Alessia Pepe. È stato un onore aver lavorato con voi in questi mesi.

Grazie di cuore a tutti per la fiducia e per aver creduto in me anche in quei momenti in cui io non sono stata in grado di farlo. Conserverò ogni ricordo di questi anni stupendi, che mi hanno resa così fiera di me stessa. Con questa pagina si conclude il mio percorso universitario, ma queste righe non sono solo le ultime di questo capitolo, ma quelle che daranno inizio ad una nuova fase della mia vita.